NUREG/CR-4171
SAND85-0442
R4
Printed December 1985

TRAC-PF1/MOD1 Independent Assessment: LOBI Large Break Transient A1-04R

L. N. Kmetyk

Prepared by
Sandia National Laboratories
Albuquerque, New Mexico 87185 and Livermore, California 94550
for the United States Department of Energy
under Contract DE-AC04-76DP00789

Prepared for
U. S. NUCLEAR REGULATORY COMMISSION

SF2900Q(8-81)

Available from

Superintendent of Documents
U.S. Government Printing Office
Post Office Box 37082
Washington, D.C. 20013-7982

and

National Technical Information Service
Springfield, VA 22161

NUREG/CR-4171
SAND85-0442
R4

TRAC-PF1/MOD1 INDEPENDENT ASSESSMENT: LOBI LARGE BREAK TRANSIENT A1-04R

L. N. Kmetyk

Date Published: December 1985

Sandia National Laboratories
Albuquerque, NM 87185
Operated by
Sandia Corporation
for the
U. S. Department of Energy

Prepared for
Reactor Systems Research Branch
Division of Accident Evaluation
Office of Nuclear Regulatory Research
U. S. Nuclear Regulatory Commission
Washington, DC 20555
Under Memorandum of Understanding DOE 40-550-75
NRC FIN No. A-1374

ABSTRACT

The TRAC-PF1/MOD1 independent assessment project at Sandia National Laboratories is part of an overall effort funded by the NRC to determine the ability of various system codes to predict the detailed thermal/hydraulic response of light water reactors during accident and off-normal conditions. The TRAC code is being assessed at Sandia against test data from various integral and separate effects test facilities. As part of this assessment matrix, a large-break transient performed at the LOBI facility has been analyzed.

Our results show that TRAC-PF1/MOD1 correctly predicts the major phenomena occurring during a large break accident. Subcooled and saturated discharge coefficients both equal to 1.0 give good agreement with data for break flows and primary system depressurization. Accumulator flow is calculated to begin within 1 s of the observed time, and the predicted accumulator injection is generally within 5% of the measured value. Both the peak clad temperature (788 K) and the overall rod temperatures are in acceptable agreement with data (823 K PCT).

Sensitivity studies were done on the cold leg nodalization, the magnitude of the core bypass flow, the saturated break flow discharge coefficient and the accumulator surge line resistance. A coding error was discovered which resulted in the calculation of substantial and prolonged liquid superheat in the core; correcting this error did not, however, significantly change any of the global behavior calculated.

These TRAC-PF1/MOD1 results are generally comparable to our previous RELAP5/MOD1 results for this same LOBI test. Similar break flow and primary pressure behavior were calculated, but for different discharge coefficients; similar accumulator injection was calculated, but for different user-input surge line resistances. The PCT predicted by RELAP5 (820 K) was in much better agreement with data, but the late-time rod temperatures predicted by TRAC are in better agreement with data than those from RELAP5.

CONTENTS

ILLUSTRATIONS

TABLES

ACKNOWLEDGEMENTS

We would like to thank Dr. Banaschik of BMFT and Dr. H. J. Caspar of GRS for graciously allowing us to publish the LOBI A1-04R data in the open literature.

1.0 INTRODUCTION

The TRAC-PF1/MOD1 independent assessment project at Sandia National Laboratories in Albuquerque is part of an overall effort funded by the U. S. Nuclear Regulatory Commission (NRC) to determine the ability of various systems codes to predict the detailed thermal/hydraulic response of light water reactors during accident and off-normal conditions. This TRAC-PF1/MOD1 assessment project is a successor to the RELAP5/MOD1 independent assessment program previously performed at Sandia.

The TRAC-PF1/MOD1 code [1] is the latest in a series of systems codes developed at the Los Alamos National Laboratory (LANL) to provide advanced best-estimate predictions of postulated accidents and transients in pressurized light water reactors. TRAC-PF1 features a two-fluid nonequilibrium hydrodynamics model with a flow-regime-dependent constitutive equation treatment; additional models have been incorporated in TRAC-PF1/MOD1 to allow simulation of a broad range of accidents relevant to current licensing issues.

The specific TRAC-PF1/MOD1 code used for the final assessment analyses reported here was Version 12.0. Many of the early calculations were done using Version 11.0, received from LANL in October 1983 when our program started. Some A1-04R calculations were done with other intermediate versions such as 11.1, 11.6 and 11.9, but any such runs are considered and flagged herein as preliminary calculations.

TRAC-PF1/MOD1 is being assessed at Sandia against experimental data from various integral and separate effects test facilities. The TRAC assessment test matrix includes two loss-of-coolant accident (LOCA) transients performed at the Loop Blowdown Investigations (LOBI) test facility in Italy [2]. The two LOBI tests in our assessment matrix are A1-04R, a 200% cold leg break scenario previously analyzed as part of our RELAP5/MOD1 assessment program [3], and B-R1M, a 25% cold leg break test which is a scaled counterpart of Semiscale intermediate break test S-IB-3 (also in our TRAC assessment matrix). We chose to analyze A1-04R first, since much of the background work had already been done during our RELAP5 analyses.

This report summarizes our TRAC analyses of the LOBI A1-04R large break LOCA test. The TRAC nodalization used for the analyses is described in Section 2. Calculational results are presented in Section 3 for the final transient analysis, as well as for the steady state initialization. Differences in the results for the basecase analysis run on the CYBER-76 and CRAY-1S computers, comparison with our previous RELAP5/MOD1

analysis and run time data are discussed in Section 4. Section 5 gives the results of some studies investigating the sensitivity of the results to different modelling and input assumptions. The history of these analyses and the code errors and problems found are included in Section 6. Section 7 summarizes the overall conclusions from these analyses. The appendices provide a brief description of the test facility, and an input listing for the basecase transient.

2.0 NODALIZATION

The LOBI test facility (shown schematically in Figure 2.1) is located at Ispra, Italy, and operated by the EURATOM Joint Research Centre [2]. The facility was designed to supply experimental data on simulated reactor primary coolant system response during the initial high pressure blowdown portion of a LOCA. It is an approximately 1:712 scale model of a four-loop 1300 MWe pressurized water reactor, consisting of two primary coolant loops connected to the electrically-heated reactor pressure vessel model. While both experimental loops are active loops containing a circulation pump and a steam generator, one (the intact loop) has three times the water volume and mass flow of the other (the single or broken loop). A brief description of the test facility is given in Appendix I.

The TRAC-PF1/MOD1 nodalization we developed for the LOBI facility is shown in Figure 2.2. Both loops are modelled, with the triple-capacity intact loop shown on the left, the single broken loop on the right and the vessel in the middle.

This model contains 44 components with a total of 256 cells, of which 178 are 1-D cells and 78 cells are in the 3-D VESSEL component; the distribution of these cells is summarized in detail in Table 2.1. A complete listing of the input used for the final A1-04R transient analysis is given in Appendix II.

There are a total of 150 heat slabs (90 representing loop piping and 60 in the vessel) in this A1-04R nodalization. Most of the heat slabs in the 1-D components contain three nodes, although 11 slabs modelling the U-tubes in each steam generator have five nodes each; the majority of the 3-D vessel slabs use the lumped-parameter model and thus have only one "node", while the core rods have 13 nodes.

The 3-D vessel model has 3 radial rings (2 in the core and 1 in the downcomer), 2 unequal azimuthal sectors (2/3 and 1/3 on the intact and broken loop sides, respectively) and 13 axial levels (3 in the lower plenum, 6 in the core and 4 in the upper plenum). Of the two radial rings in the core, the inner ring corresponds to both the "central" and "intermediate" regions of the 8*8 assembly (containing 36 out of the 64 rods present); the second ring corresponds to the "peripheral" region of rods adjacent to the core barrel (containing the remaining 28 rods). A VESSEL component was used rather than a 1-D CORE component because of the significant heater rod power leakage in the upper plenum; the "leaky" heater rod extension into the upper plenum could not be modelled explicitly in the TEE or PLENUM components that would have been needed to hook the hot legs to the vessel in a purely 1-D model.

The vessel nodalization is shown in detail in Figure 2.3. The relative elevations of the level boundaries are given (for comparison with Figure AI.3). The core region axial levels were based on the axial rod geometry and power profile information given in Figure AI.4. The core cell heights were adjusted to give the correct total mass in each power region using the average inner rod diameter, to ensure the correct initial stored energy; the single rod geometry forced by TRAC's input does not allow modelling the actual "staggered" rod geometry. The core rod heat slabs were extended into the lower and upper plena, since a significant fraction of the rod heat (~15%) is lost outside the core "heated length", as shown in Figure AI.4. Besides the core rods, heat slabs have been included for much of the major vessel structure -- the pressure vessel itself, the core barrel, the upper closure plate, and the upper head and bypass line piping walls.

The external upper head and bypass line (shown in Figure AI.3 at the top of the vessel) were modelled with 4 1-D volumes, attached at one end to the intact loop cold leg and at the other end to one of the inner cells in the top level of the 3-D VESSEL. More correctly, these connections would both have been to cells in the top level of the 3-D VESSEL component, one in the downcomer and one in the second radial ring. However, this would have required a third azimuthal sector, and was not done to keep the total number of vessel cells below the perceived limit (100) allowing direct inversion of the vessel solution matrix; this limit is not specifically mentioned in the PF1/MOD1 manual but shows up in an input processing error message.

Both the single-phase and the two-phase degraded homologous head and torque curves for the two circulation pumps are taken from published LOBI pump curves [4,5]. The Semiscale two-phase head multiplier curve was used since no other data was available.

Piping elbows and area changes are carefully modelled in the loop piping, using guidelines developed at Sandia during the course of this assessment project. The resulting pressure drops calculated are in good agreement with the differential pressure measurements for steady state conditions [6]. Our results from various steady state calculations (for the PKL natural circulation tests [7,8] and the B&W OTSG separate effects tests [9] as well as for this LOBI integral test) indicate that the previous RELAP5/MOD1 input developed cannot be used directly. User-input loss coefficients representing pipe bends are unchanged but user-input loss coefficients for pipe tees are removed, because our results suggest that the TRAC TEE component calculates some of the necessary momentum effects internally (unlike RELAP5 BRANCH components). Hydraulic diameters (a cell-edged variable

in TRAC) are adjusted to produce the correct overall wall friction whenever two pipes of different areas (and hence different cell-centered diameters) are adjacent. The vena contracta area is input for orifices rather than the geometric area, and the friction factor option is usually NFF=-2 (at area changes) or NFF=+2 (in smooth pipes and at both VESSEL connections and TEE primary-to-secondary connections).

Table 2.1 Nodalization

	Hydro Cells	Heat Slabs	BREAKs/FILLs
Intact Loop			
Hot Leg	5	5	
SG Primary	13		
U-Tubes		11	
SG Secondary	32		2
Pump Suction	8	8	
Pump	2	2	
Pump Seal Leakage	2	2	1
Cold Leg	5	4	
Pressurizer			
Vessel	5	5	2
Surge Line	6	6	
Accumulator			
Vessel	5		
Valve/Surge Line	6	6	
Broken Loop			
Hot Leg	5	5	
SG Primary	13		
U-Tubes		11	
SG Secondary	32		2
Pump Suction	6	6	
Pump	2	2	
Pump Seal Leakage	2	2	1
Pump-Side Cold Leg	6	6	1
ARGUS Valve	2	2	
Vessel-Side Cold Leg	7	7	1
Vessel			
Downcomer	26	26	
Lower Plenum	12	8	
Core	24	12 (+4 rods)	
Upper Plenum	16	10	
Upper Head	4		

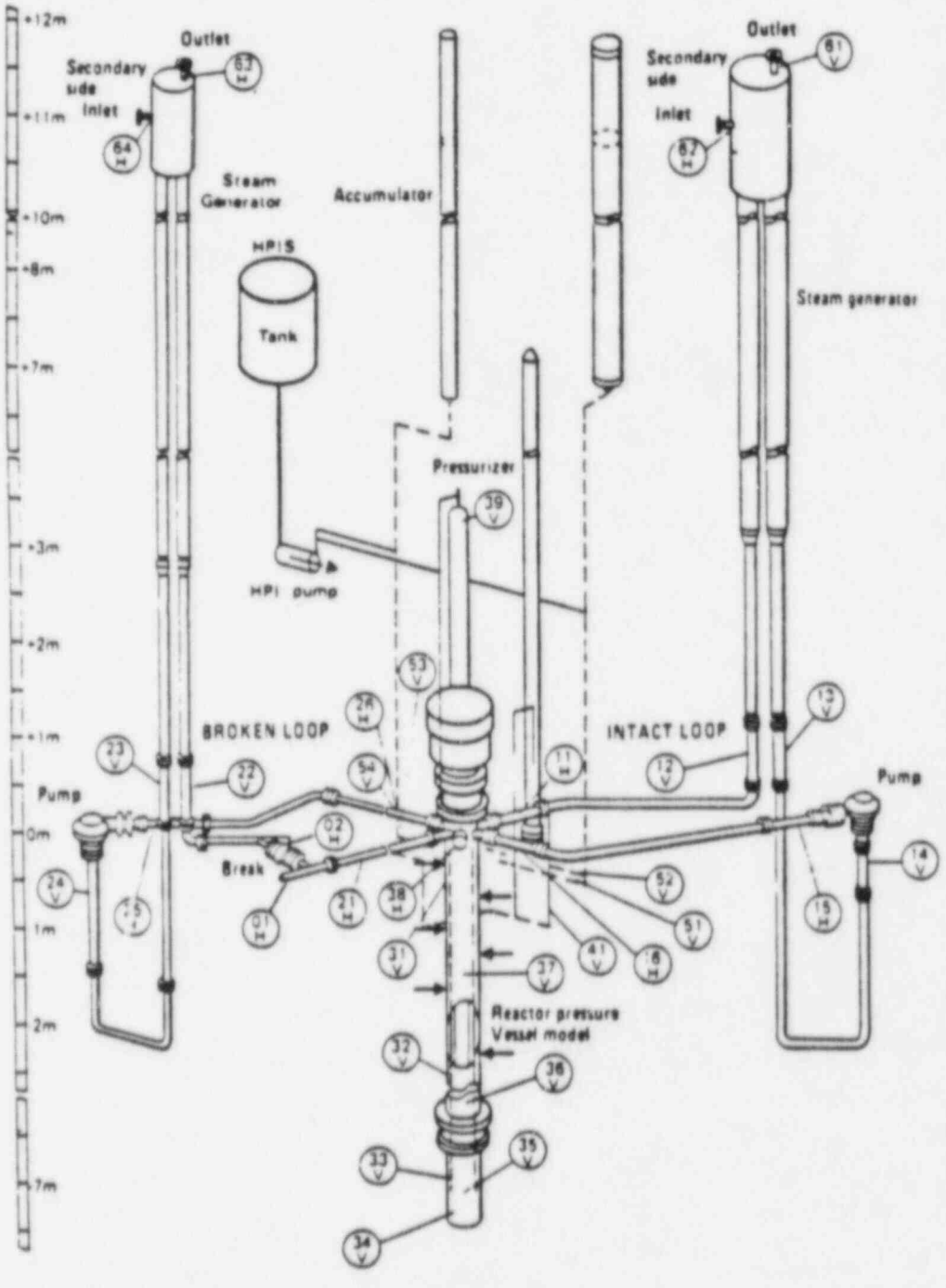

Figure 2.1 LOBI Test Facility

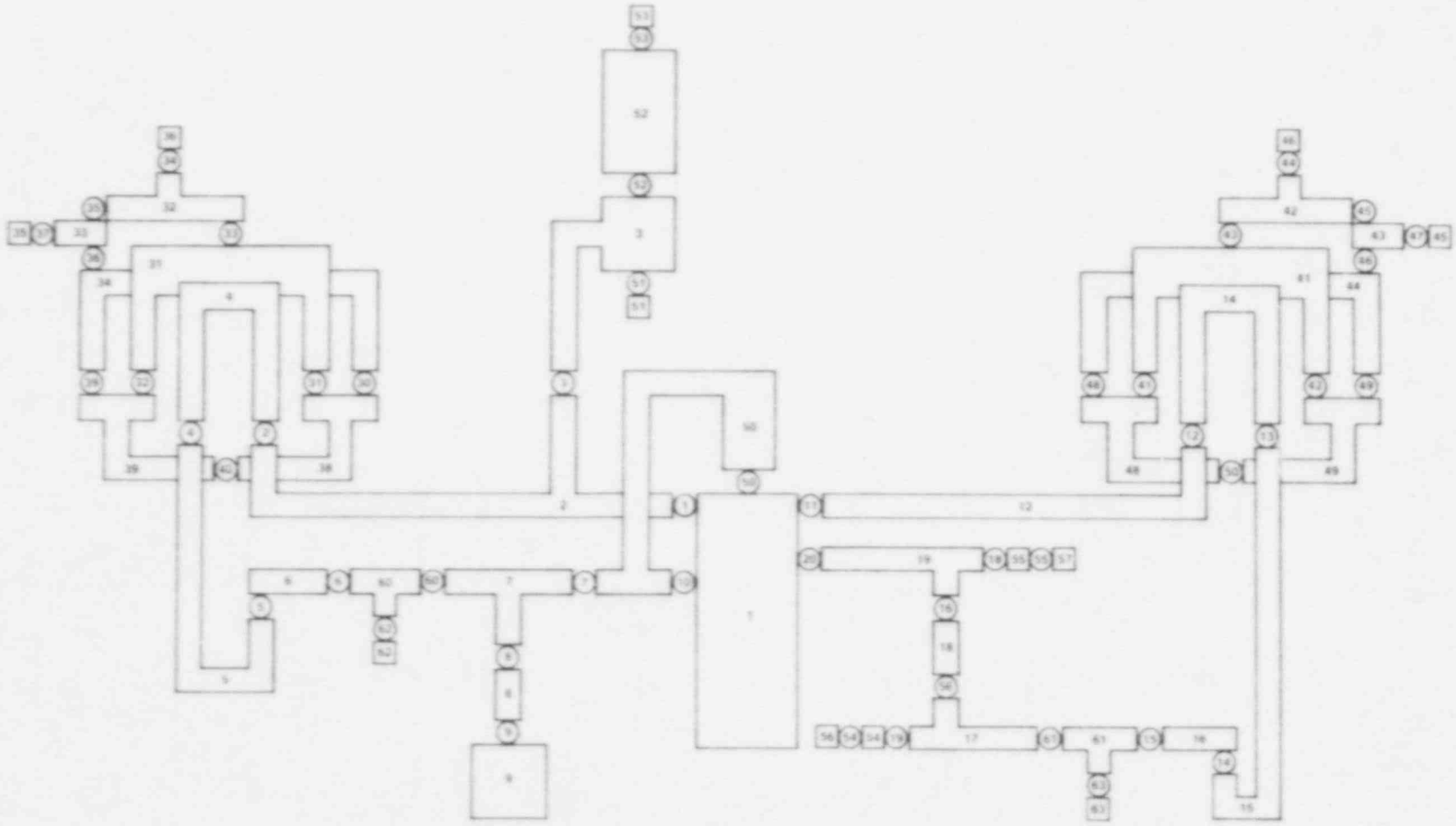

Figure 2.2 Facility Nodalization

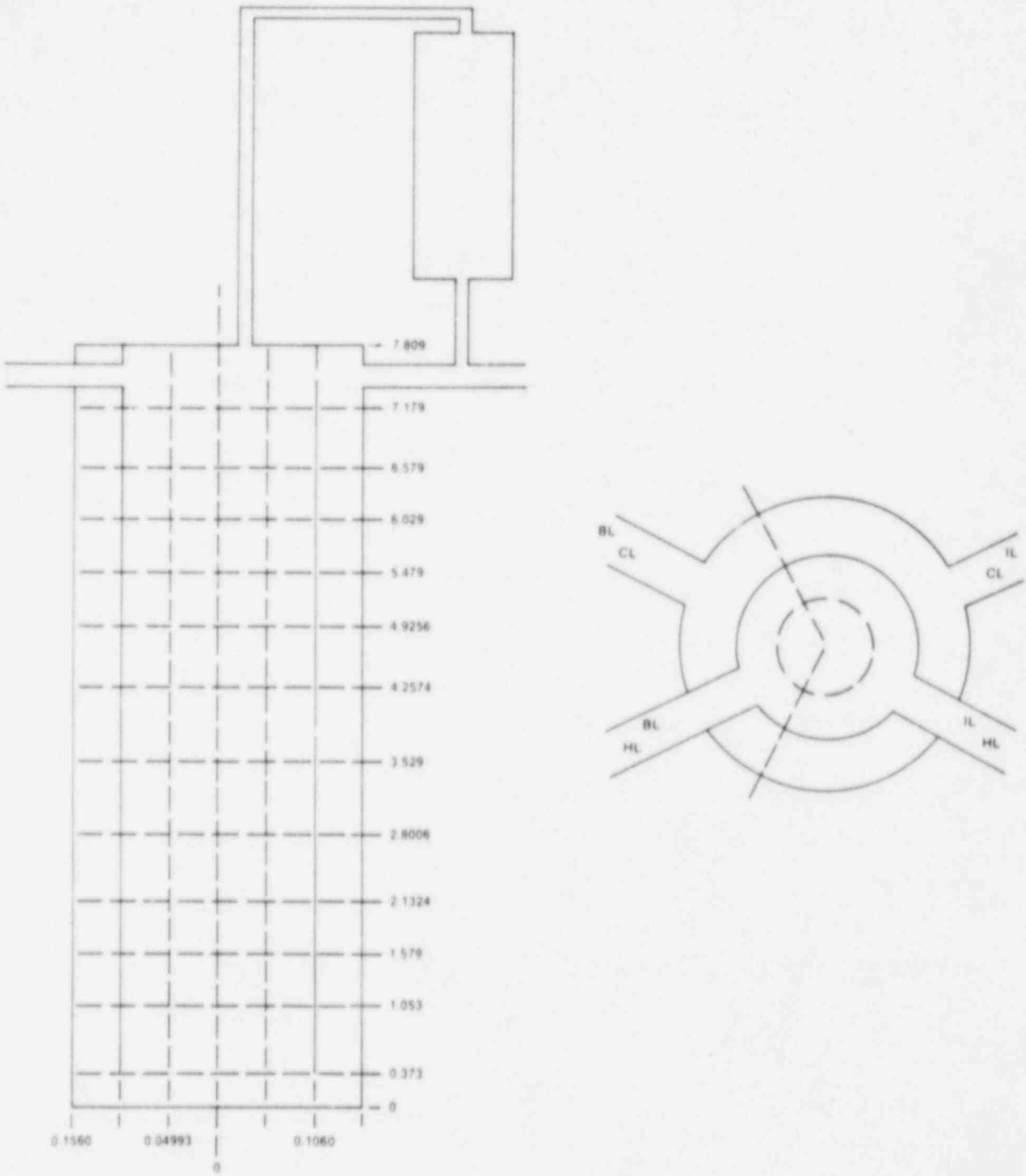

Figure 2.3 Vessel Nodalization

3.0 BASECASE ANALYSIS RESULTS

The first part of the LOBI experimental program consisted of the six large-break A1 tests. These were simulations of 200% double-ended offset-shear breaks in the cold leg pipe between the pump and the pressure vessel. The first main LOBI test, A1-04(C), was also chosen for a "blind" standard problem calculational exercise, the LOBI pre-prediction exercise (LOBI PREX). A summary of the A1 test series is given in Table 3.1. Three of these six tests (the PREX test A1-04, A1-03 and A1-04R) were analyzed during our RELAP5/MOD1 independent assessment program [3]. Of these, test A1-04R [11,12], the most similar to a design-basis 200% cold leg break, was chosen as part of our current TRAC-PF1/MOD1 independent assessment program.

3.1 Transient Initialization

Table 3.1.1 shows the measured and calculated steady state initial conditions, with good agreement achieved for all major parameters. The TRAC steady state calculation was begun by inputting the RELAP5 initial values rather than from cold no-flow conditions, saving significant computer time. As in our earlier RELAP5 calculations, we found that using the minimum tube-to-tube spacing as the heated equivalent diameter on the outside of the U-tubes (rather than the usual hydraulic diameter) was required to allow simultaneous matching of the primary side cold leg temperature and the secondary side pressure.

A remarkable fluid temperature imbalance was measured between the outlets from the pressure vessel to the broken and intact loops. (This temperature difference may be caused by an asymmetric flow behavior in the upper plenum of the test facility where, due to an extension of the heater rods, about 8% of the total power is transferred to the fluid.) This fluid temperature imbalance between intact and broken loop is not calculated, although reasonable agreement is seen between experimental weighted average fluid temperatures for the hot and cold legs of both loops and the calculated temperatures.

Table 3.1.2 gives the transient boundary conditions. The vessel-side break flap valve opens first, defining time "zero"; the other, pump-side, break flap valve has a delay of ~0.05 s before opening, and the ARGUS break isolation valve closes in about 1 s. (The break assembly is described in more detail in Appendix I, and is shown in Figure AI.9.) The core heater rod power after the transient starts is controlled by the specified power curve. Both the intact and broken loop pumps were also controlled using specified speed-vs-time curves. The bleed from

the primary system, required for pump seal water removal, was stopped at blowdown initiation, although the seal water injection in both pumps increased after the transient started. The feedwater flows to the intact and broken loop steam generators were reduced to zero in 10 and 25 s, respectively, and the steam outlets of the generators were kept open during the whole transient; the resulting secondary side pressures were specified as boundary conditions in our analyses. The LOBI containment simulator was connected to the atmosphere; the containment pressure thus did not greatly exceed atmospheric pressure during the transient and was therefore modelled as a constant one-atmosphere boundary condition.

3.2 Primary System Thermal/Hydraulics

Figure 3.2.1 shows the pressures in the intact loop cold leg and in the broken loop upstream of the pump-side break. (The experimental data digitized from the curves in the published data reports [8,9] are shown as dashed lines, and the calculational results are shown as solid lines.) The overall agreement between calculation and experiment is very good. After initiation of blowdown, the saturation pressure in the hot legs is reached in ~100 ms. At this time, flashing in the hot leg starts and the depressurization rate for the two curves decreases. Flashing in the intact loop cold leg begins at about 3 s, which causes a further decrease in the depressurization rate. After ~24 s the accumulator activation pressure is reached and the accumulator injection starts.

(This accumulator injection pressure value is calculated to occur at about the right time, because it was used to choose the value of the saturated discharge coefficient applied at the break junctions. A value of 1.0 was found to give the best agreement with the data. The sensitivity of the calculated results to the saturated discharge coefficient assumed is discussed in Section 5.3. The peak break flow values were the criteria used to select the subcooled discharge coefficient applied at the break junctions. A value of 1.0 gave the good overall agreement for both pump-side and vessel-side peak break flows.)

The pressure in the broken loop upstream of the pump-side break falls immediately to the saturation pressure and is then mainly governed by the break flow. The mass flow rates upstream of the vessel-side and pump-side breaks are shown in Figure 3.2.2. During most of the blowdown, critical flow conditions exist at the throat of the discharge nozzles, so that the break mass flows are determined only by the upstream flow conditions. At the vessel-side break, subcooled water is supplied directly from the large downcomer region, which leads to prolonged

subcooled conditions upstream of the vessel-side break. As a consequence, large vessel-side break mass flows (Figure 3.2.2a) occur during the first 2 s of the transient with values up to ~70 kg/s. Due to the relatively large flow resistance of the pump, piping and steam generator upstream of the pump-side break, the pump-side break mass flow (Figure 3.2.2b) is limited to values below ~30 kg/s. The break flows calculated are in good agreement with experimental data, with no long-term deviations visible.

(The measured break flow data given come from combining densitometer and either turbine meter (pump-side) or drag disc (vessel-side) measurements, and are subject to several errors in addition to standard measurement uncertainties. [9] The pump-side drag disc measurement was considered to be unreliable due to a transducer mounting error. The vessel-side drag disc transducer was uncalibrated for positive flows, explaining the difference in initial steady state flow shown, and the measurement channel was saturated for the first few seconds of the transient, explaining the truncated peak break flow data shown. However, the given measurement uncertainty afterwards is small compared to the data; in contrast, the velocity measurement uncertainty on the turbine meter used for the pump-side break flow is quite large compared to data, and is the likely source of the pump-side initial steady state flow discrepancy.)

The calculated and measured broken loop cold leg densities between the vessel and the vessel-side break valve are shown in Figure 3.2.3. The cold leg voids somewhat more quickly in the calculation from 5 to 10 s than was measured, and accumulator liquid slugs are not calculated in the broken loop cold leg until ~50 s, about 25 s later than first measured. Also, the mechanism generating these oscillations is apparently different in the calculation and the experiment. The measured density oscillations begin at about the same time as accumulator injection and bypass, and thus are likely condensation-induced. However, even though substantial bypass is calculated, calculated density oscillations do not appear until the lower plenum refills and liquid begins entering the core, with resulting manometric flow oscillations as steam generated in the core pushes the accumulator liquid back up the downcomer and into the broken loop cold leg. (This will be discussed in more detail in Section 3.3.)

Figure 3.2.4 gives the broken loop hot leg and pump suction leg densities. The agreement with data is generally good. The small brief increase in density at about 5 seconds corresponds to the reestablishment of positive core flow. The hot leg density comparison suggests that this increase is slightly underpredicted in the calculation. While little sign of this slug is visible in the calculated pump inlet density, it does propagate through this point because it can be seen in the pump-side break upstream mass flow in Figure 3.2.2b.

The hot leg and pump suction leg densities in the intact loop are shown in Figure 3.2.5. The calculated pump inlet density is in very good agreement with data, but several discrepancies are seen in the hot leg. The high density measured early in the transient (~5-10 s) is probably a combination of the pressurizer draining, the reestablishment of positive core flow and the draining of the steam generator U-tubes, as is the smaller density spike at ~15 seconds. The calculated behavior is both qualitatively and quantitatively different in the first 30 s of transient, with a smaller first density spike and a larger second spike and subsequent density drop all later than measured. The source of these discrepancies is not known. (The intact loop cold leg density, particularly the behavior after the onset of accumulator injection, will be discussed in Sections 3.3 and 5.1.)

Most of the primary side temperatures are in good agreement with experimental measurements, because large portions of the primary system remain saturated after the initial blowdown and because the overall agreement between calculated and measured system pressure is quite good. However, some vapor superheat was measured in the course of the transient, primarily around the steam generator inlets and outlets. Summaries of measured and calculated temperatures in the primary system are given in Figures 3.2.6 and 3.2.7. During the course of the blowdown, the primary pressure drops below that in the secondary system, after which time heat is transferred from secondary to primary in the steam generators. This is clearly visible in Figure 3.2.6 where the steam generator outlet plenum temperature at late times rises to the secondary side temperature (not shown but ~540 K). The same phenomenon is qualitatively calculated in the broken loop steam generator (Figure 3.2.7) but at a smaller magnitude than measured.

We see problems calculating the correct vapor superheat conditions in some places. As shown in Figure 3.2.6, the intact loop steam generator inlet plenum shows calculated vapor superheat appearing later (by ~5 seconds) than measured; this temperature then rises to the measured value within about another 5 s and subsequently decreases at ~50 seconds in agreement with the data. However, the superheating does not then recover to its previous value, as observed. The same behavior is seen in both the calculated and measured intact loop hot leg temperatures. This indicates that less superheated vapor is being generated in the core and transported out the hot leg at late times in the calculation as compared to the experiment.

The second place there are problems is seen in Figure 3.2.7. The broken loop steam generator inlet plenum temperature is measured to be at saturation rather than superheated through

most of the transient, while the calculation shows ~10-20 K vapor superheat after about 30 seconds, when the broken loop is mostly voided; this may represent superheated vapor being transported from the core, energy transfer from the hot piping walls in the model or simply a reflection of some relatively stable nonequilibrium behavior being calculated by TRAC. The broken loop steam generator outlet plenum temperature, however, shows less superheating throughout the entire period of reverse heat transfer than measured. The low superheating calculated may be due to too high a mass flow rate through the tubes' primary side or to too high a liquid proportion in the broken loop flow.

The vapor superheat seen in the hot legs and/or steam generator inlet and outlet plena is dissipated as the vapor continues to flow around the loops and enters the pumps. Downstream of the pump in the intact loop, a different set of phenomena dominates the temperature (and density) response due to accumulator injection, as will be discussed in Section 3.3.

3.3 Accumulator Injection

The injection of ECC water from the intact loop accumulator is initiated when the pressure in the intact loop cold leg falls below the accumulator pressure of 2.7 MPa at ~24 s. As shown by the accumulator injection flow rates in Figure 3.3.1, the maximum measured injection is 3.3 kg/s, while the maximum calculated rate is 3.4 kg/s. (Sensitivity studies on the effect of the accumulator surge line resistance on the injected flow are discussed in Section 5.4.) The accumulator injection is underpredicted by ~10% at later times in this calculation, possibly due to some miscalculation of condensation effects on the pressure drop at the injection point.

About 2 s after the injection has started, the cold leg pipe between the injection point and the pressure vessel is completely filled with subcooled water in the experiment, as indicated by the steep increase of the fluid density to its subcooled value during this time period in Figure 3.3.2; in contrast, the calculation shows a much lower density indicating a substantial quantity of steam still present. The calculated density response after the onset of accumulator injection was found to be very sensitive to the nodalization detail used, as will be discussed later in Section 5.1. Figure 3.3.3 shows the liquid temperature at the ECC injection point, which is correctly calculated despite the density behavior shown in Figure 3.3.2. (The vapor still present in these cells remains saturated.)

Most of the injected ECC water bypasses around the downcomer and is discharged through the vessel-side break during the

blowdown period. However, some accumulator liquid is delivered to and retained in the vessel almost immediately, so that there is no significant period of perfect bypass predicted. The calculated vessel liquid mass is shown in Figure 3.3.4; there is no measured data available for comparison. It begins increasing at ~28 s, only 4 seconds after accumulator flow begins and several seconds before the accumulator flow peaks at ~33 s. The 50 kg increase in the vessel liquid mass after this time represents about 25% of the total accumulator injection (assuming ~65 s of ~3 kg/s injection). The other 75% must be bypassing the vessel and going out the vessel-side break, since the loop densities (in particular, the cold legs) do not show any substantial liquid accumulation. This is verified by a careful scrutiny of the vessel-side break flow rate shown in Figure 3.2.2a, where a small increase in flow rate of ~1-2 kg/s is seen starting at about 25 s.

Figure 3.3.5 shows the downcomer liquid mass, indicating that most of the accumulator liquid retained in the vessel actually remains in the downcomer, although some of it does reach the lower plenum, as seen in Figure 3.3.6. The oscillations starting at ~45 seconds push small amounts of water up into the core, as shown in Figure 3.3.7, which gives the core liquid mass. (The magnitudes of the oscillations being calculated in the downcomer, lower plenum and core are the same, but the different ordinate scales visually exaggerate the oscillations in the lower plenum.)

These "manometer-type" oscillations occur when the liquid entering the core from the downcomer via the lower plenum contacts the hot core rods and is rapidly vaporized. The resulting increase in local core pressure pushes liquid from the core and lower plenum back up into the downcomer until continued accumulator injection and pressure decay causes the process to repeat. The frequency and amplitude of these oscillations depend strongly on the rate of core quenching and on the ECC liquid injection rate. The vessel refill rate in this transient is slow enough that a rapid core reflood does not occur. Instead, the rod heat is slowly removed via steam cooling, by the steam generated during the liquid inflows in these oscillations.

3.4 Core Thermal Response

The initial unbalance of the two break mass flows leads to a reversal of the core flow during the first few seconds of the blowdown, while the flashing process is restricted to the hot legs, upper plenum and core region. This is shown by the negative core inlet liquid flows during this time period in Figure 3.4.1. After flashing has started in the downcomer region, a

positive core mass flow is reestablished, as seen between 3 and 10 s. This positive flow sweeps remaining fluid with higher density from the lower plenum through the core, the hot leg and the steam generator, and shows up in Figure 3.2.2b as a small increase in the pump-side break flow after a minimum at ~3-4 s. (The large liquid flow oscillations in Figure 3.4.1 after 45 s reflect the manometric oscillation of accumulator liquid between the core and the downcomer and lower plenum, discussed in Section 3.3.)

Even small amounts of liquid entering the core contribute strongly to core heater rod cooling. Figure 3.4.2 shows the input core power and the total rod heat transfer rate; changes in the total rod heat transfer rate are related to the core inlet liquid flow changing the core liquid mass (shown previously in Figure 3.3.7). Generally, when the total rod heat transfer rate is greater than the core power, the rods cool down; conversely, when the total rod heat transfer rate is less than the core power, the rods heat up. This can be best seen by correlating the qualitative behavior of the maximum calculated heater rod temperature, shown in Figure 3.4.3, with the differences between core input power and total rod heat transfer given in Figure 3.4.2.

The rod heat transfer drops rapidly below the input core power soon after transient initiation as the core voids, but then recovers somewhat due to reestablished positive core flow returning some liquid to the core. As the total rod heat transfer drops early in the transient, the maximum rod temperature increases rapidly until turned around by the reestablished positive core flow forcing total rod heat transfer to be greater than the input core power. The core power is greater than the total rod heat transfer again at 13-15 s when another more gradual general core heatup is calculated, as shown by the second increase in maximum heater rod temperature during that time period. The heat transfer and the gradual drop in the maximum rod temperature from about 13 s to 45 s are due almost entirely to steam cooling, which is then enhanced after intermittent delivery of accumulator liquid to the core begins at ~45 s.

Measured and calculated heater rod temperatures for the various instrumented levels are shown in Figures 3.4.4 through 3.4.11. When only a single measured rod temperature is shown for a given level, it represents a mean or typical temperature of all thermocouples in the central and the intermediate (but not the peripheral) core regions. Calculated values in the first core ring and data from the central and intermediate rod zones are all indicated as "center", while calculated values in the second core ring and data from the peripheral rod zone are marked "edge".

The differences between measured and predicted temperatures before and shortly after time zero are a result of the steep radial temperature profile in the heater tube walls for the high surface heat fluxes present during forced convection and nucleate boiling; the thermocouples, which are located 0.4 to 0.5 mm beneath the outer rod surface, indicate temperatures up to 15 K higher than the calculated surface temperatures during this period. After departure from nucleate boiling (DNB) has occurred, these differences are much smaller due to the relatively flat radial temperature profile that develops.

In the data, DNB is seen throughout the entire core heated length at about 1 s (Figures 3.4.4 through 3.4.11). The peak clad temperature (PCT) of 823 K was measured in the high-powered middle section of the heated length at 3.2 s, just before the power input was reduced to 32.5% (Figures 3.4.7 and 3.4.9). The reduction in power combined with the improved cooling conditions as flashing began in the downcomer and positive core flow was reestablished caused an early rewetting of most of the rods at around 10 s, but a second dryout occurred almost immediately in the middle and upper levels (Figures 3.4.7 through 3.4.11). The rewet observed at ~10 s is total for heater rods in the central and intermediate rod zones, but only partial for rods in the peripheral rod zone adjacent to the core barrel (particularly visible in Figure 3.4.8), suggesting that some flow channeling occurred in the test. Rod cooldown due to accumulator-driven recovery is seen at later times in the higher core levels. The magnitude of the accumulator injection is not high enough to reflood the core on this time scale; instead, the rod temperature drops are primarily due to steam cooling, as small amounts of accumulator liquid are flashed in the core.

Just as measured, DNB was also calculated to occur throughout the entire core heated length at about 1 s. A PCT of 788 K was calculated in the middle of the high-powered middle section of the bundle at 3.2 s, just before the power input was stepped down. Many of the rod temperatures calculated exhibit an initial dryout followed by a partial or total rewet and a second dryout, as does the experimental data. The calculated rod temperatures also show a bottom-up cooling front. The qualitative behavior is generally well-predicted despite minor quantitative differences.

The rod temperatures at the core entrance (Figure 3.4.4) are in very good agreement with data. Farther up the lower core (Figures 3.4.5 and 3.4.6), the early-time partial core rewet begins a little earlier in the calculation than observed (leading to lower predicted blowdown peak temperatures) and the early-time total core rewet is calculated somewhat later than observed; the second brief dryout and heatup in the calculation is later and smaller than that measured.

The predicted PCT of 788 K at the core mid-plane (Figure 3.4.7) is in reasonably good agreement with the experimental value of 823 K. The discrepancy may be due primarily to the approximation of the actual staggered hollow-rod geometry required in the TRAC input. Using the rod average thickness and adjusting the heights of the various core levels (as already mentioned in Section 2), we matched the power input to each section and the total mass in each section, ensuring the correct initial stored energy. However, the average hollow rod thickness in the high-powered middle section of the core heated length is greater than the actual thickness in that region, which would increase the characteristic conduction time and thus slow the rod surface heatup. (There is no way to match all the staggered hollow-rod geometry within the current TRAC input limitations.)

The rod temperatures at the core mid-plane also show an earlier partial rewet in the calculation, with no total core rewet calculated; the predicted second heatup begins from higher rod temperatures and thus the calculated late-time rod temperatures are generally higher than observed. The experimental data show an early-time total core rewet only in the central and intermediate zone rods above and below the core mid-plane; the peripheral rods show only a partial rewet before the second heatup. The data also show an early rod "quench" at ~20-30 s just below the core mid-plane (Figure 3.4.8a), and a later quench at ~60 s just above the core mid-plane (Figure 3.4.8b); while one of the rods cools substantially at ~30 s in the calculation, quench at the mid-plane is not predicted until after ~60 s, with considerable asymmetry in the individual rod quench behavior.

Above the core mid-plane region (Figures 3.4.9 and 3.4.10), the early-time partial core rewet also begins slightly earlier in the calculation than was observed, leading to somewhat lower peak rod temperatures. A total core rewet is calculated in rods in the inner core ring, which represents the central and intermediate heater rod zones, but not in the second core ring, representing the peripheral rods; this indicates that some flow channeling is being calculated. Higher in the core, particularly at the core outlet (Figure 3.4.11), the calculated temperatures are substantially lower than measured, although qualitatively correct; this may be due partly to our assumption that the ~8% heater rod power leaked into the upper plenum is uniformly distributed there, while it may actually be concentrated more near the core heated length.

LOBI Tests Summary, Programme A1

Test Nr / Date	Initial Conditions: Po bar	T_o /T °C	M_o kg/s	P_o MW	Boundary Conditions: Rupture Position	Rupture Size	Core Power P = f (t)	Pump I, II	ECCS	Results / Commentary
A1-04C 12-12-79	153	330 / 291.	25.8	5.38	cold leg	2x1A	off at t_{sc} 1.8s 1.8 full power seconds	I ramp to 70% in 5s II ramp to 0 in 3s	Accu (26 bar) intact loop cold leg	- PREX test - 2x1A double-ended, cold leg break - 1.8s full power - cold leg Accu injection
A1-01B 29-01-80	152.4	323.3 | 289 327.7	26.2	5.11	cold leg	2x1A	t≤2.6s : 100% t≤15s : 20% t≤30s : 10% t>30s : 0 6.58 full power seconds	I ramp to 70% in 5s II ramp to 0 in 2s	Accu (27 bar, 30 °C). IL h. +c. leg BL h.leg	- Power ascension series - 2x1A d.e. - c.l. break - combined, hot & cold leg injection - core power 3.9 full power seconds only, due to control error - B.L. Accu injection delayed - oscillations during injection period
A1-02B 14-02-80	153	322 | 290 326.5	28	5.33	cold leg	2x1A	t≤ 3s : 100% t≤15s : 25% t≤30s : 10% t≤50s : 5% >50s : 0 8.5 f.p.s.	I ramp to 70% in 5s II ramp to 0 in 2s	Accu (27 bar, 30 °C): IL h. +c. leg BL h.leg	- Power ascension series - 2x1A d.e. - c.l. break - combined, h. & c. leg inject. - core power 8.5 full power seconds - oscillations during injection period
A1 - 03 19-03-80	153	320 | 289 325.6	28	5.22	cold leg	2x1A	t≤3.2s : 100% ≤15s : 30% ≤20s : 15% ≤30s : 10% ≤50s : 5% >50s : 0% 9.49 full power seconds	I : ramp to 70% in 5s II : ramp to 0 in 2s	Accu (27 bar, 30 °C) : IL . h. +c. leg BL : h. leg	- Power ascension series - 2x1A d.e. - c.l. break - combined, h.&c. leg inject. - 9.04 full power seconds due to temporary power shut-off - oscillations during injection period
A1-04B 17-04-80	153	328 | 288 332	28	5.12	cold leg	2x1A	t≤3.2s : 100% ≤15s : 38% ≤20s : 15% ≤30s : 10% ≤50s : 5% >50s : 0 10.2 full power seconds	I : ramp to 70% in 5s II : ramp to 0 in 2s	Accu (27 bar, 30 °C) : IL : c. leg BL :	- Power ascension series (last test) - Repeat of PREX test - 2x1A d.e. - c.l. break - only cold leg injection - 10.2 full power seconds - increased Accu injection rate due to piping modification
A1-05A 06-05-80	153	324 | 291 328	28	5.26	cold leg	2x1A	t≤3.2s : 100% ≤15s : 36% ≤20s : 15% ≤30s : 10% ≤50s : 5% >50s : 0 10.2 full power seconds	I : ramp to 70% in 5s II : ramp to 0 in 2s	Accu (27 bar, 30 °C) : IL : h. +c. leg BL : h. leg	- 8 Accu plant ref. test - 2x1A d.e. - c.l. break - combined h.&c. leg inject. - 10.2 full power seconds - Accu injection rate into I.L. not high enough for simulating 8 Accu plant

Table 3.1 LOBI A1 Experimental Test Program [10]

Table 3.1.1 Steady State Initial Conditions

Variable	Data	TRAC
Core Power (MW)	5.12	5.12
Primary Pressure (MPa)	15.3	15.26
IL Hot Leg Temperature (K)	600	600.9
IL Cold Leg Temperature (K)	571	570.0
IL Mass Flow (kg/s)	21.1	21.0
IL Pump Speed (rad/s)	498	500.
BL Hot Leg Temperature (K)	606	600.5
BL Cold Leg Temperature (K)	571	569.8
BL Mass Flow (kg/s)	7.0	7.01
BL Pump Speed (rad/s)	397	400.
IL SG Pressure (MPa)	6.4	6.4
IL SG Steam Temperature (K)	553	553.0
IL SG Feedwater Temperature (K)	493	493.0
IL SG Feedwater Flow (kg/s)	2.07	2.1
BL SG Pressure (MPa)	6.4	6.4
BL SG Steam Temperature (K)	553	553.0
BL SG Feedwater Temperature (K)	501	501.0
BL SG Feedwater Flow (kg/s)	0.8	0.8

Table 3.1.2 Experimental Boundary Conditions

Vessel Side Break Opens	0-0.005 s	
Pump Side Break Opens	0.045-0.050 s	
ARGUS Valve Closes	0-0.6 s	
Core Power	0-3.2 s	100%
	3.2-15 s	32.5%
	15-20 s	12.6%
	20-30 s	8.8%
	30-50 s	5.3%
	50-	0%
Intact Loop Pump Speed	0 s	100%
	0-8 s	ramp to 71%
	8-	71%
Broken Loop Pump Speed	0 s	100%
	0-3 s	ramp to 10%
	3-36 s	ramp to 0%
	36-	0%
IL Pump Seal Water	t<0	0.019 kg/s
	t>0	0.025 kg/s
BL Pump Seal Water	t<0	0.018 kg/s
	t>0	0.030 kg/s
Pump Seal Water Drain	t<0	0.037 kg/s
	t>0	0
IL SG Feedwater Flow	ramp to 0 in 20 s	
BL SG Feedwater Flow	ramp to 0 in 10 s	

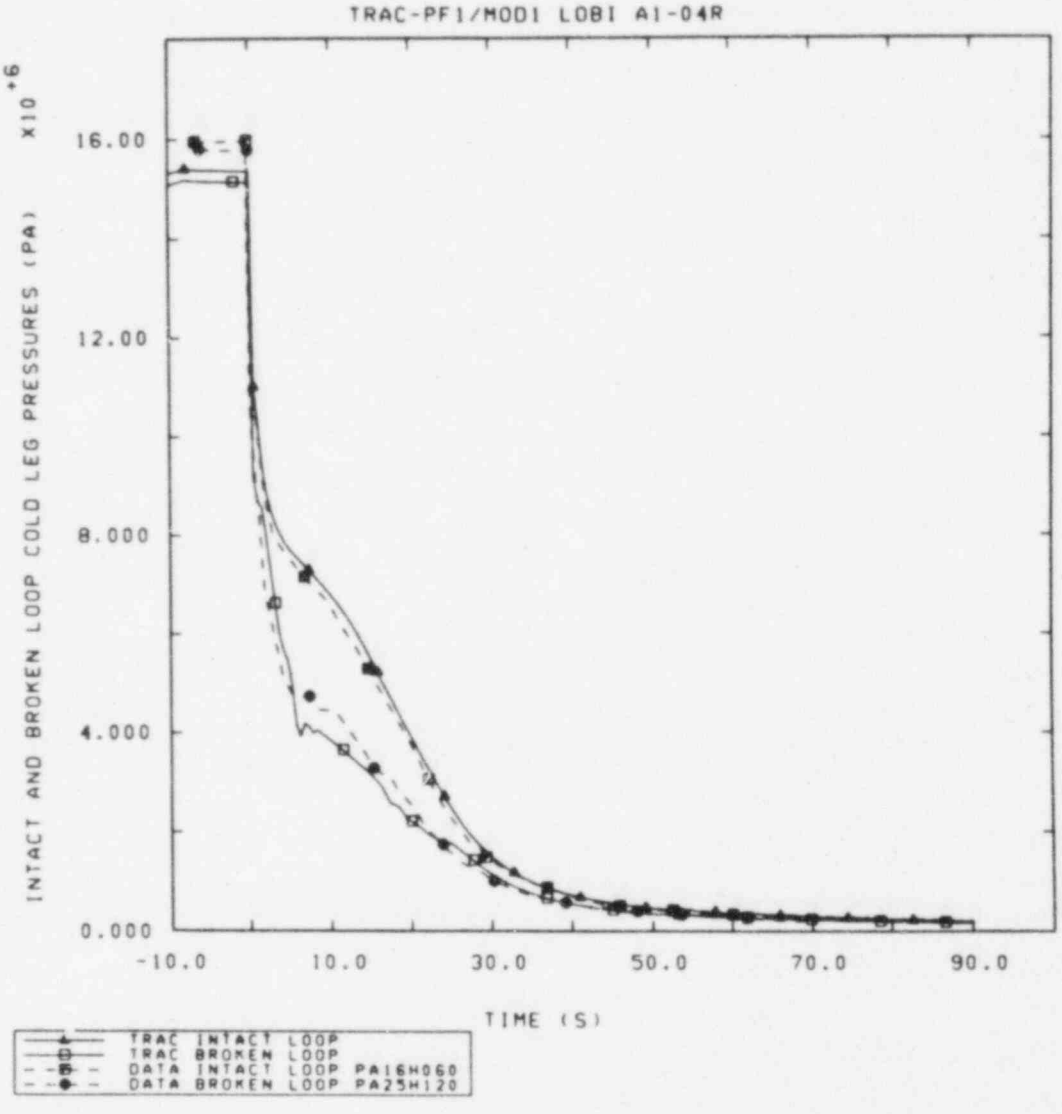

Figure 3.2.1 Intact and Broken Loop Cold Leg Pressures

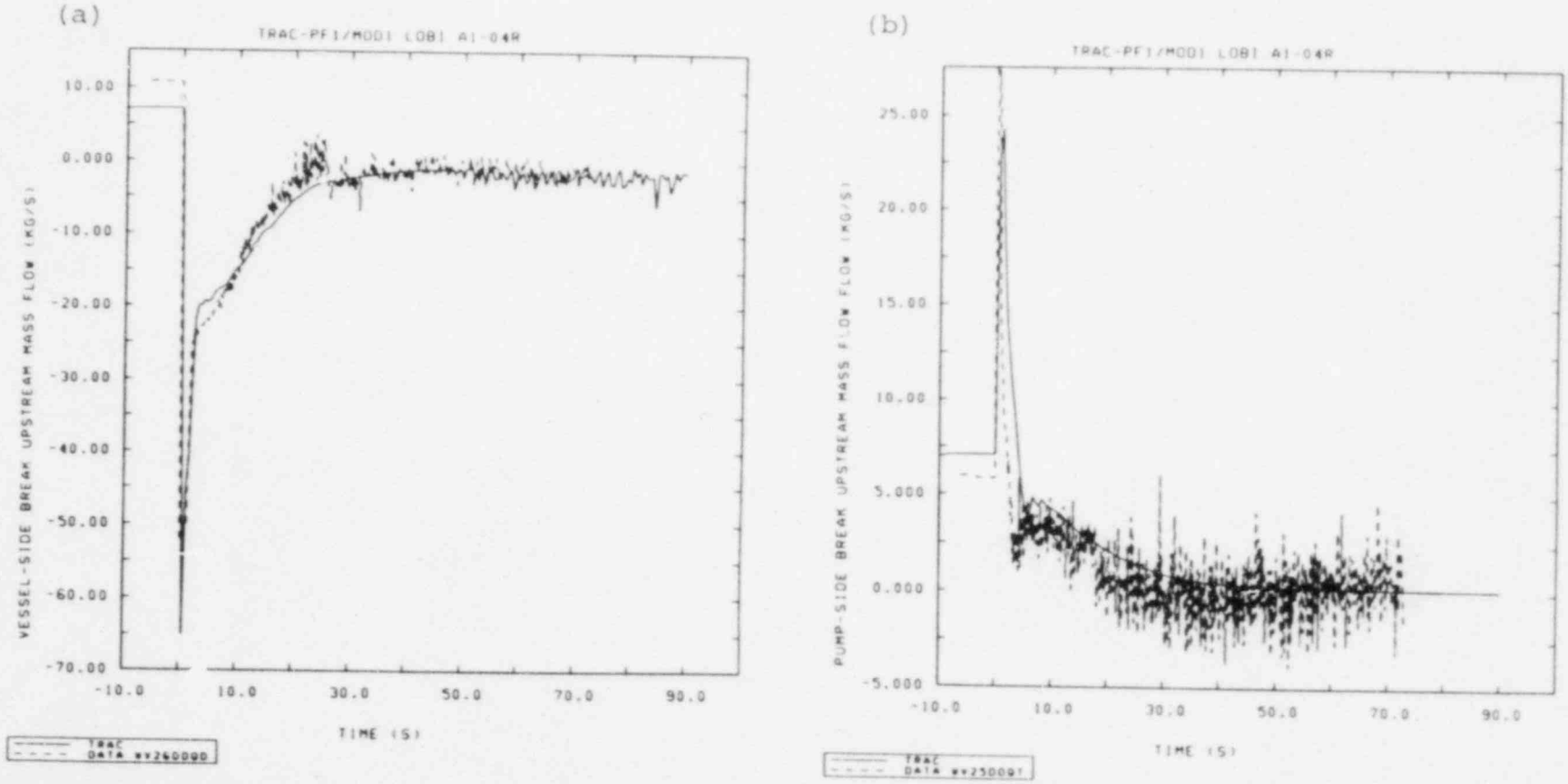

Figure 3.2.2 (a) Vessel-Side and (b) Pump-Side Break Mass Flow Rates

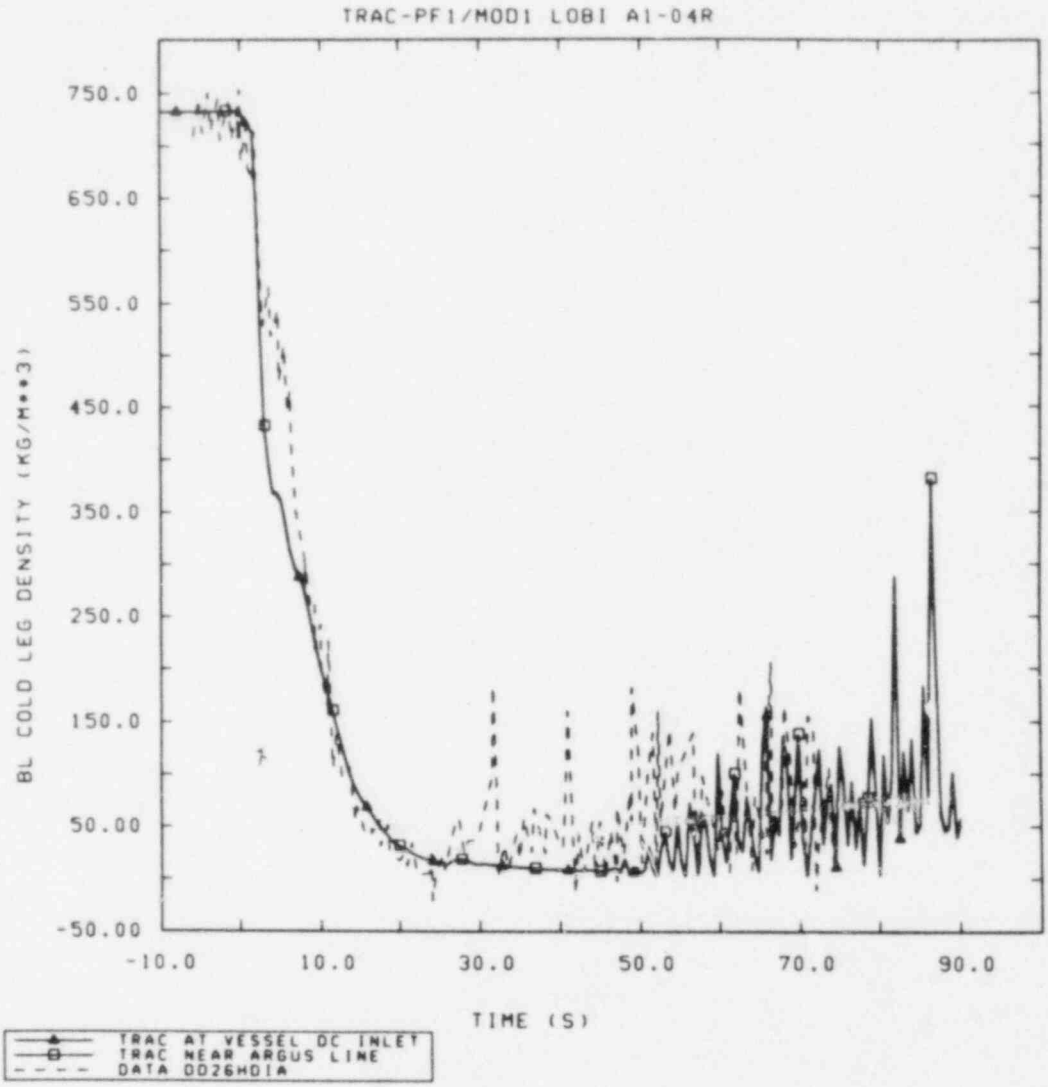

Figure 3.2.3 Broken Loop Cold Leg Densities

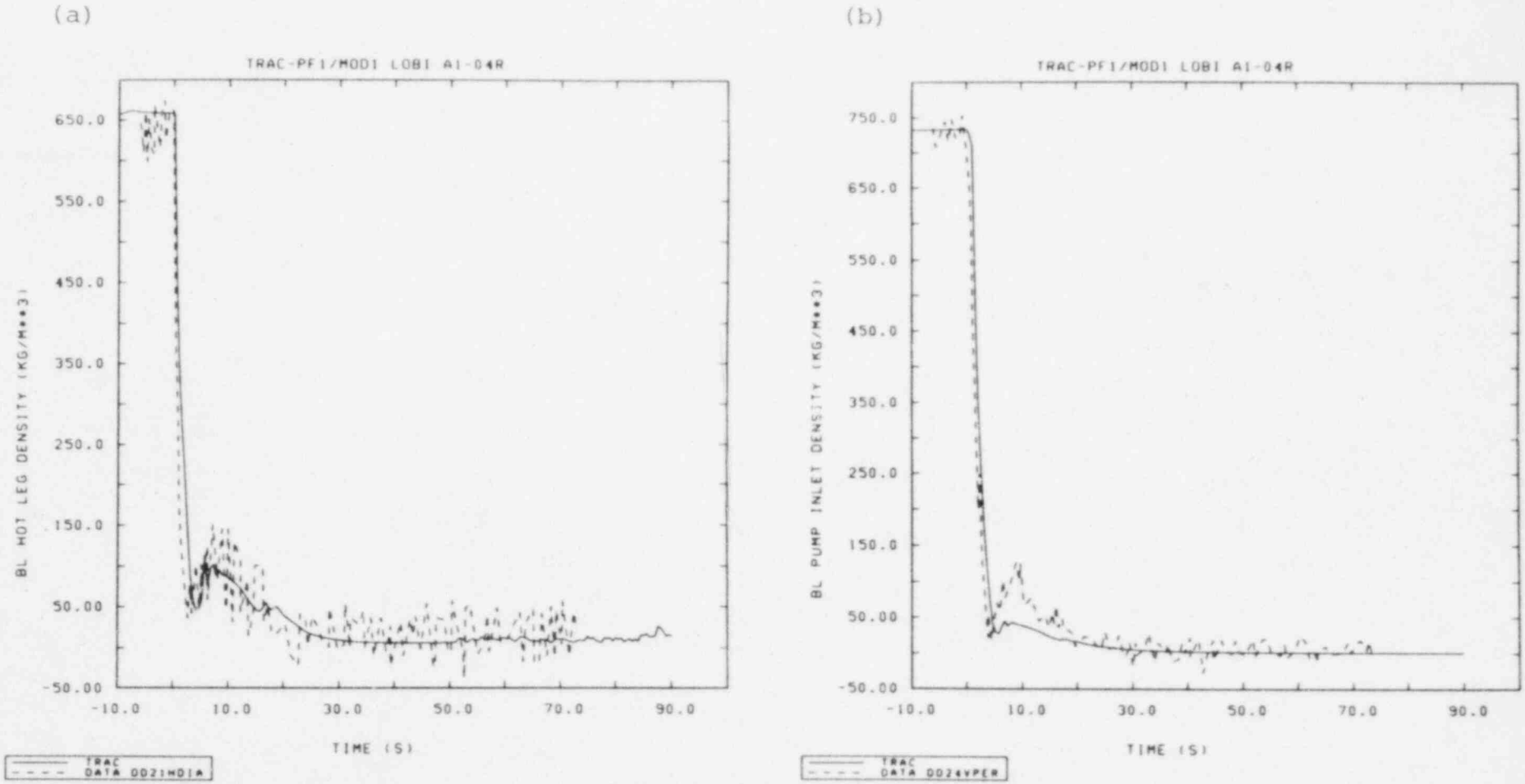

Figure 3.2.4 Broken Loop (a) Hot Leg and (b) Pump Suction Leg Densities

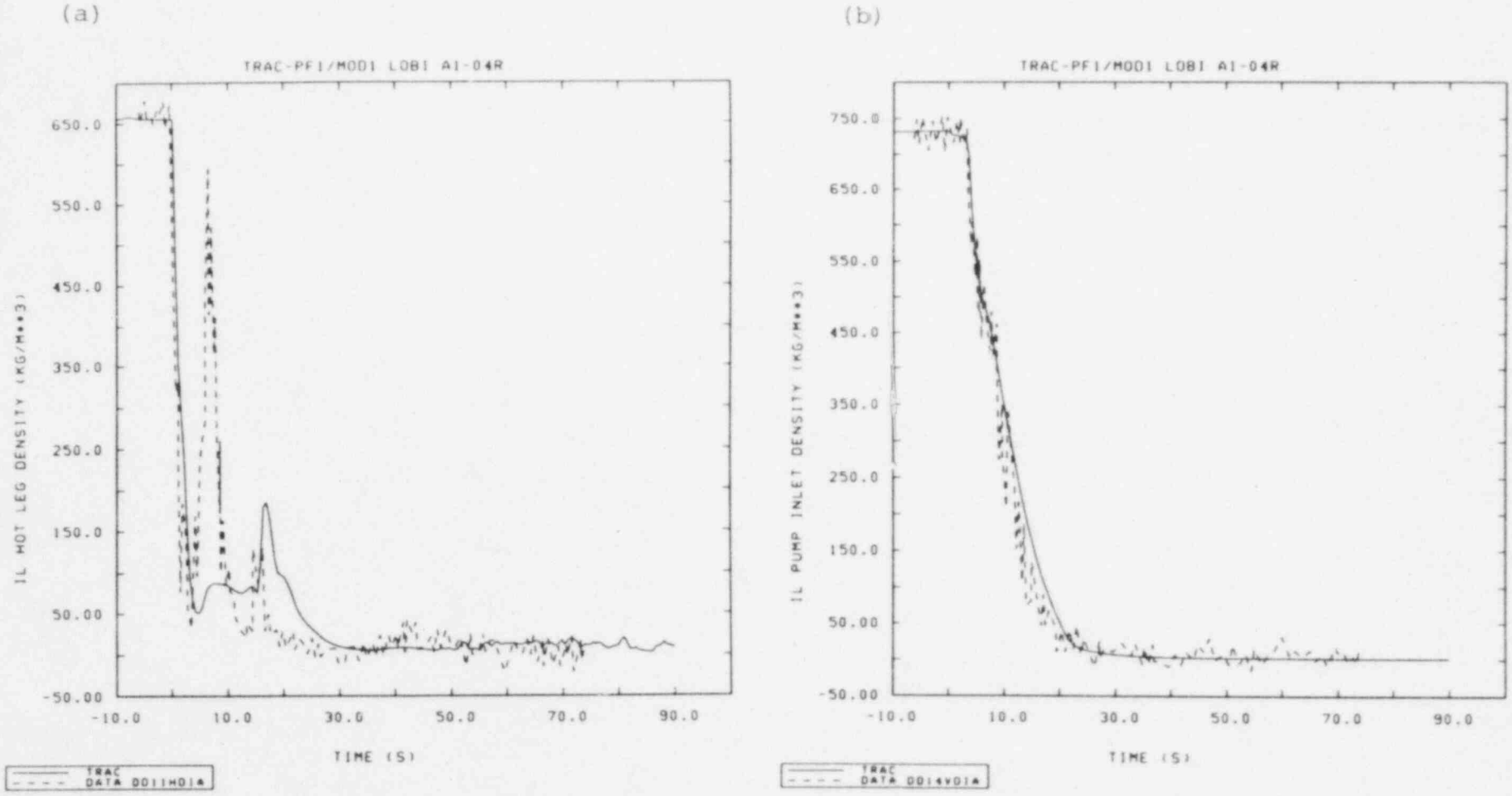

Figure 3.2.5 Intact Loop (a) Hot Leg and (b) Pump Suction Leg Densities

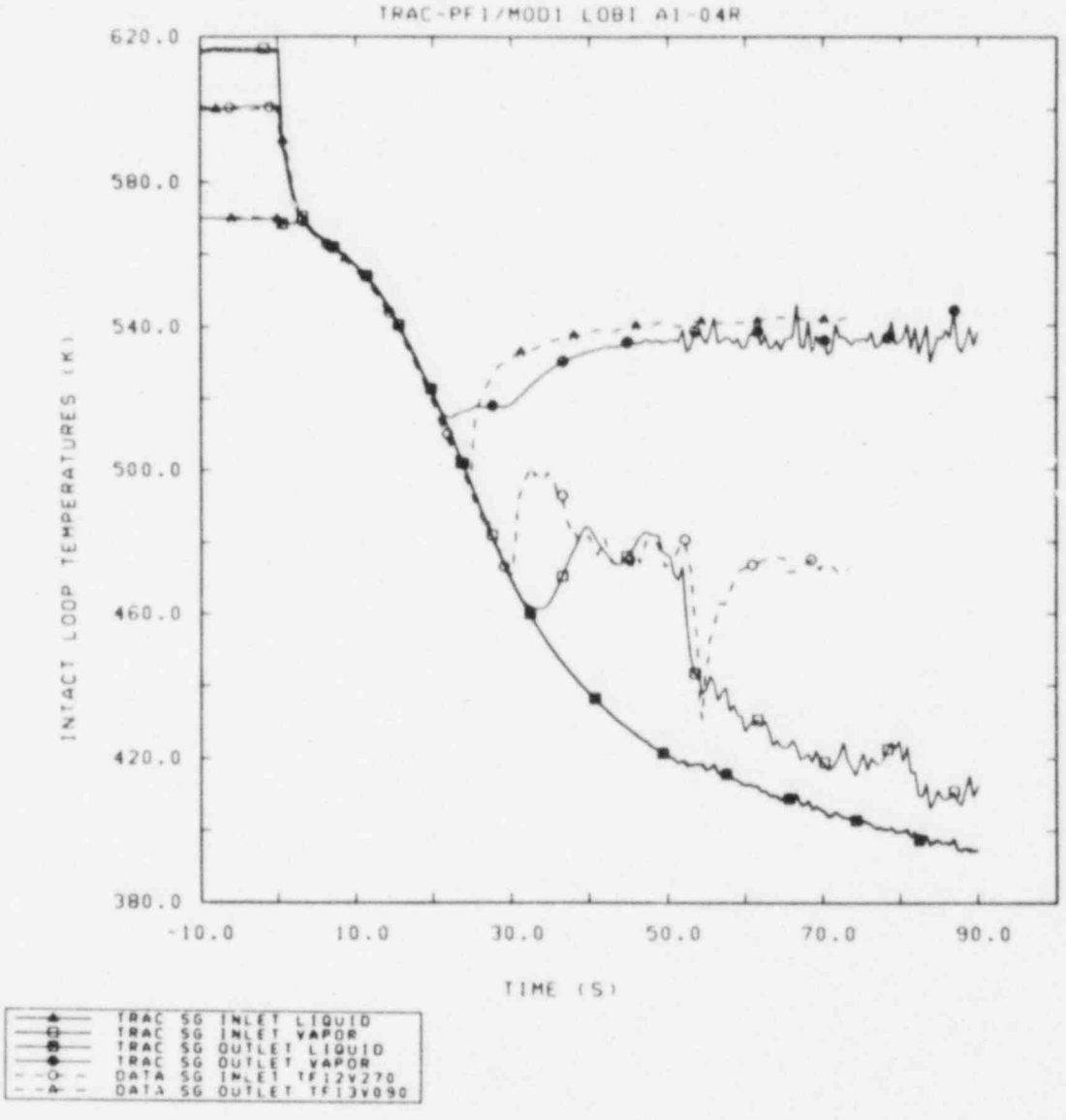

Figure 3.2.6 Intact Loop Steam Generator Temperatures

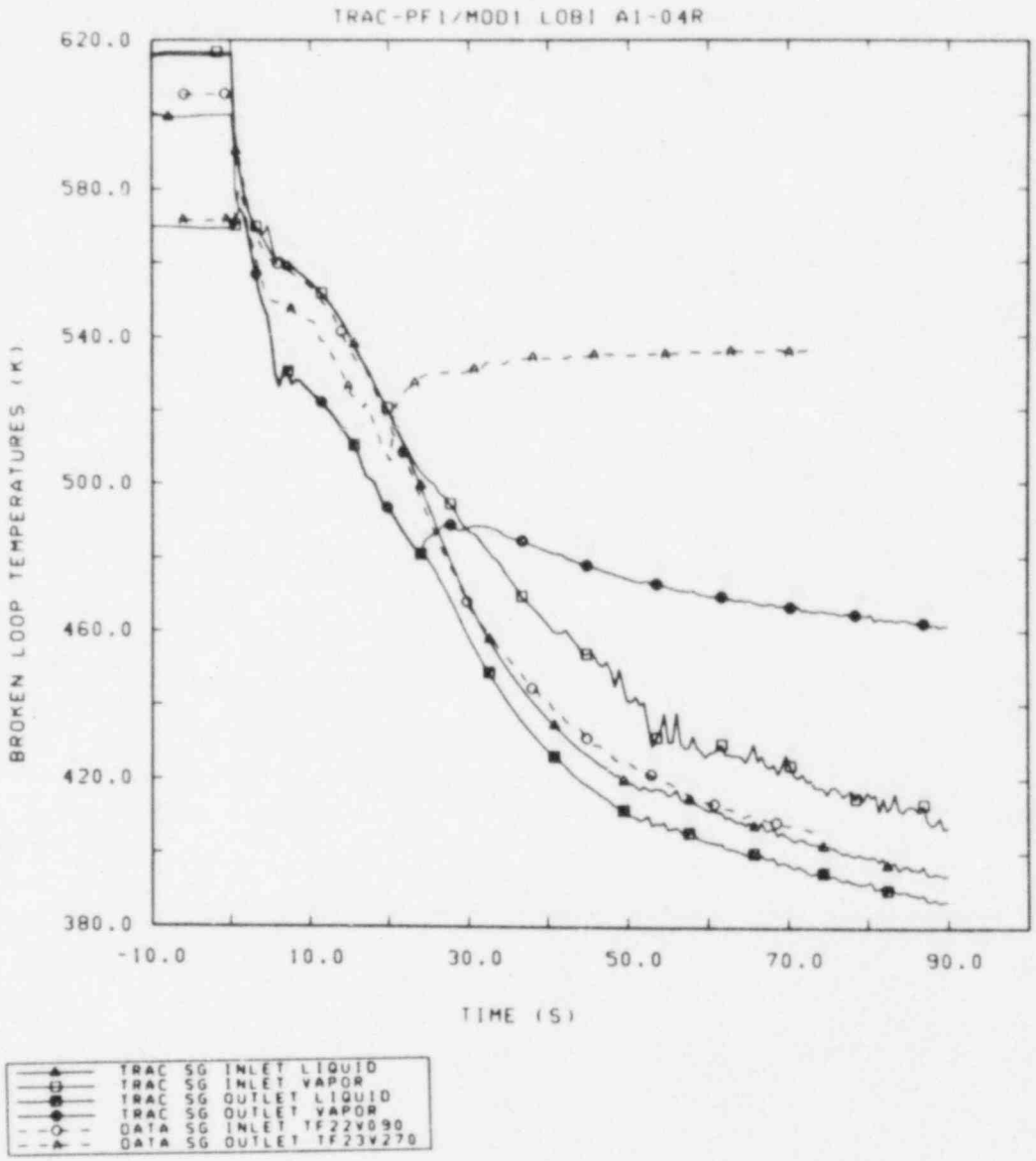

Figure 3.2.7 Broken Loop Steam Generator Temperatures

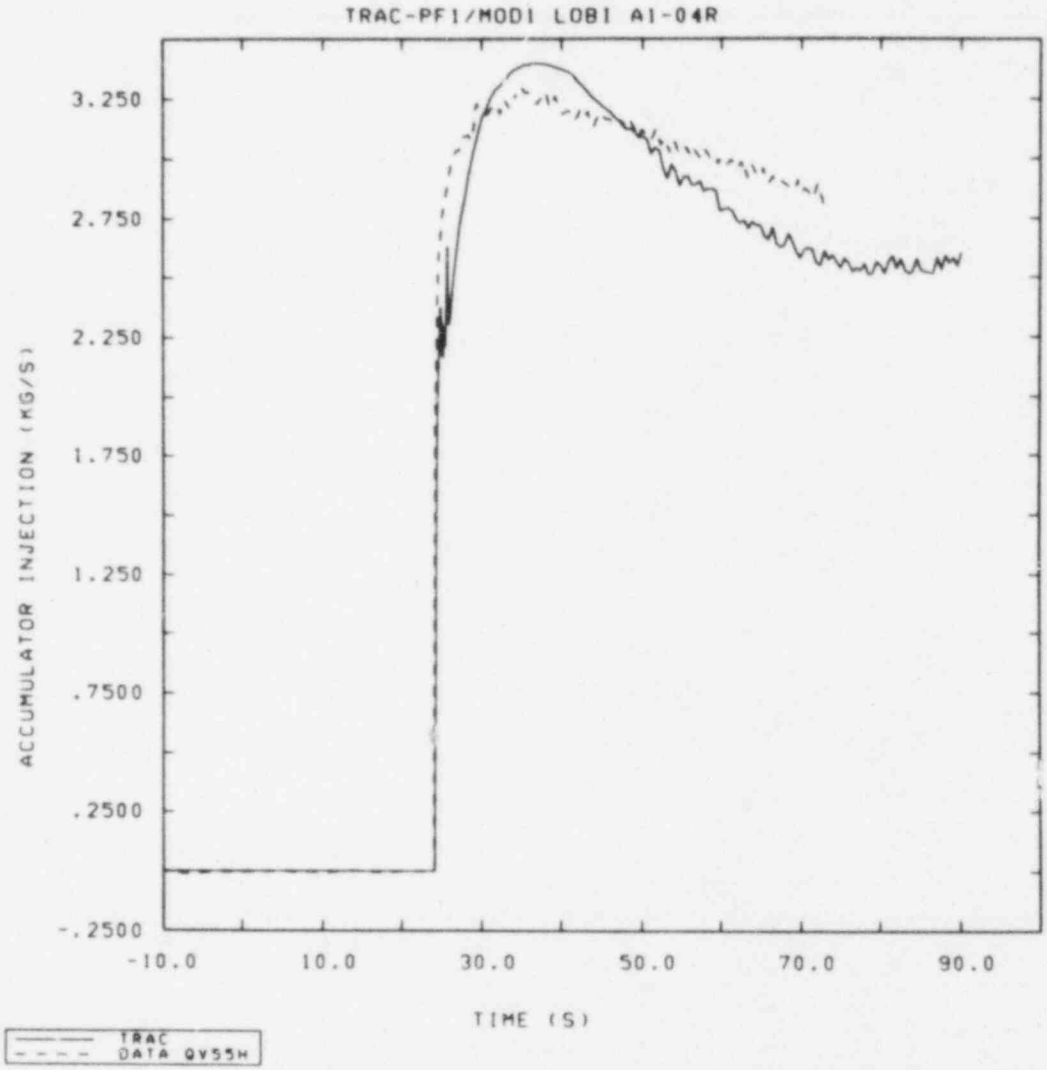

Figure 3.3.1 Accumulator Injection Flow Rate

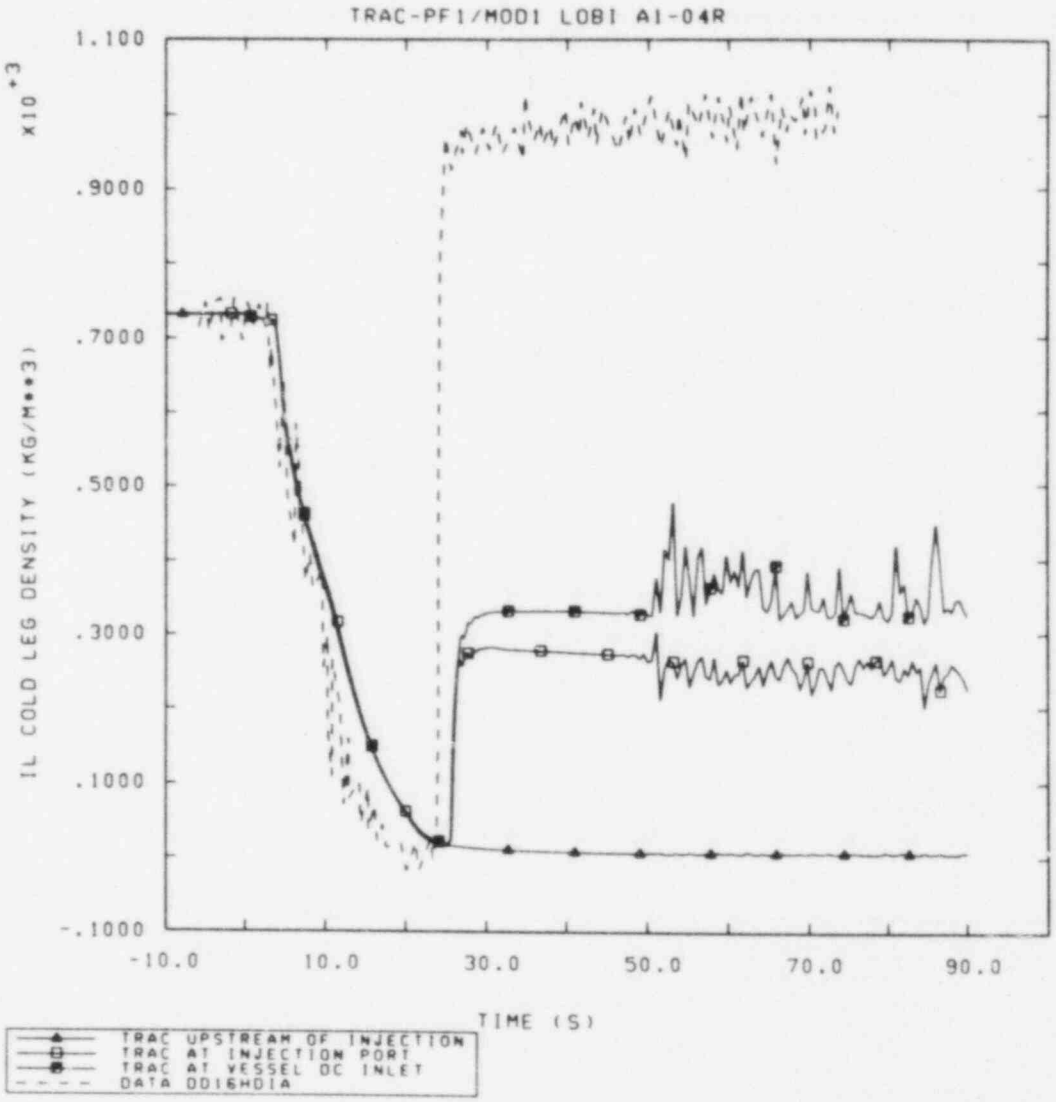

Figure 3.3.2 Intact Loop Cold Leg Densities at and Downstream of Accumulator Injection

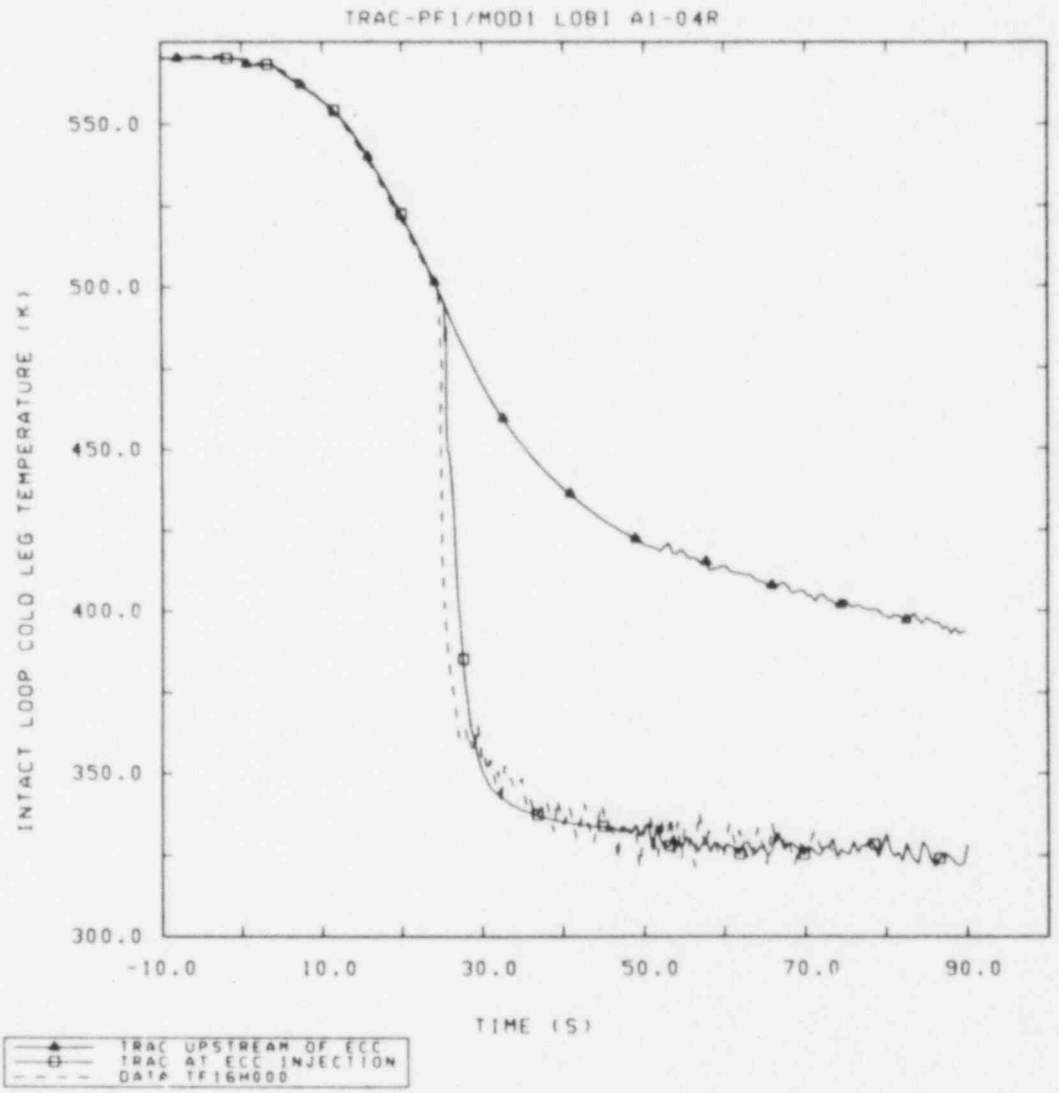

Figure 3.3.3 Intact Loop Cold Leg Liquid Temperatures at and Upstream of Accumulator Injection

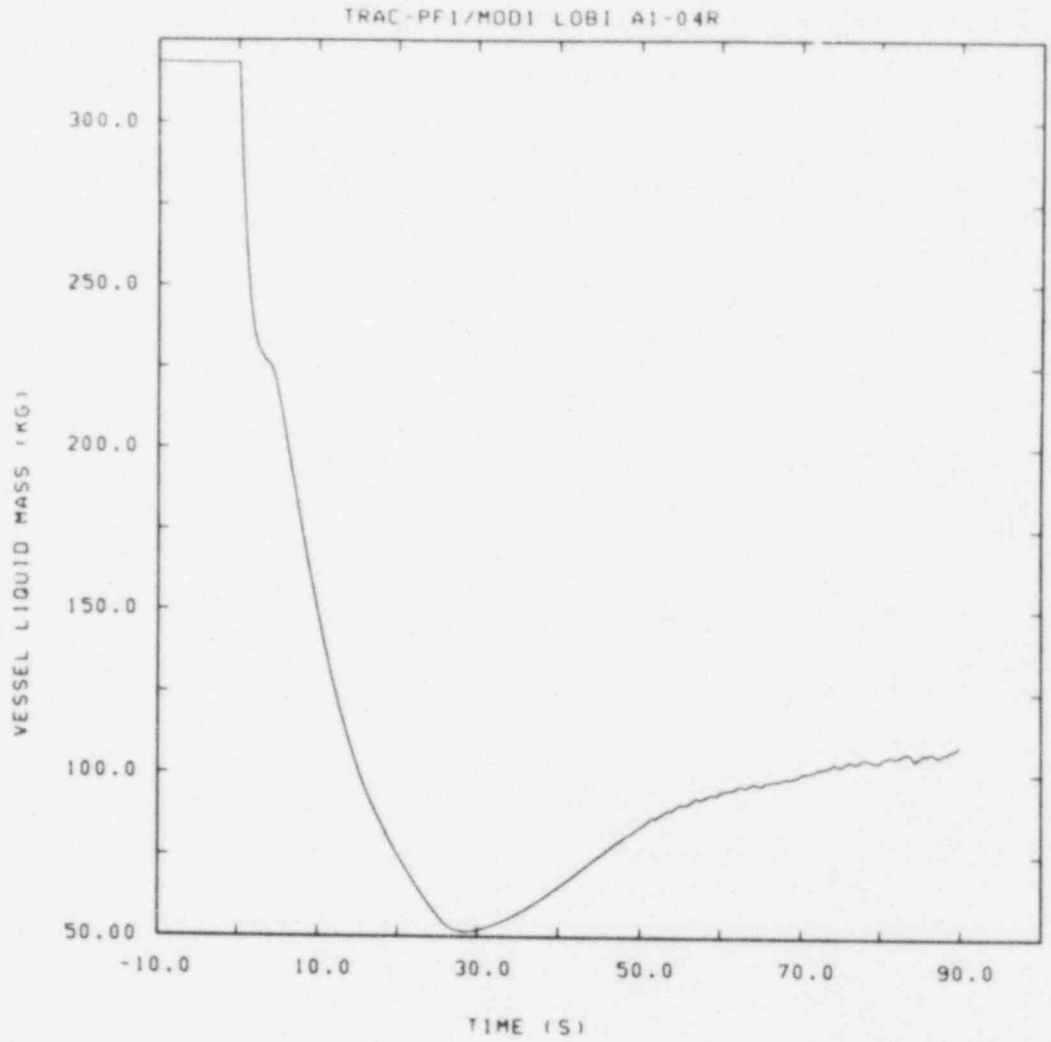

Figure 3.3.4 Vessel Liquid Mass

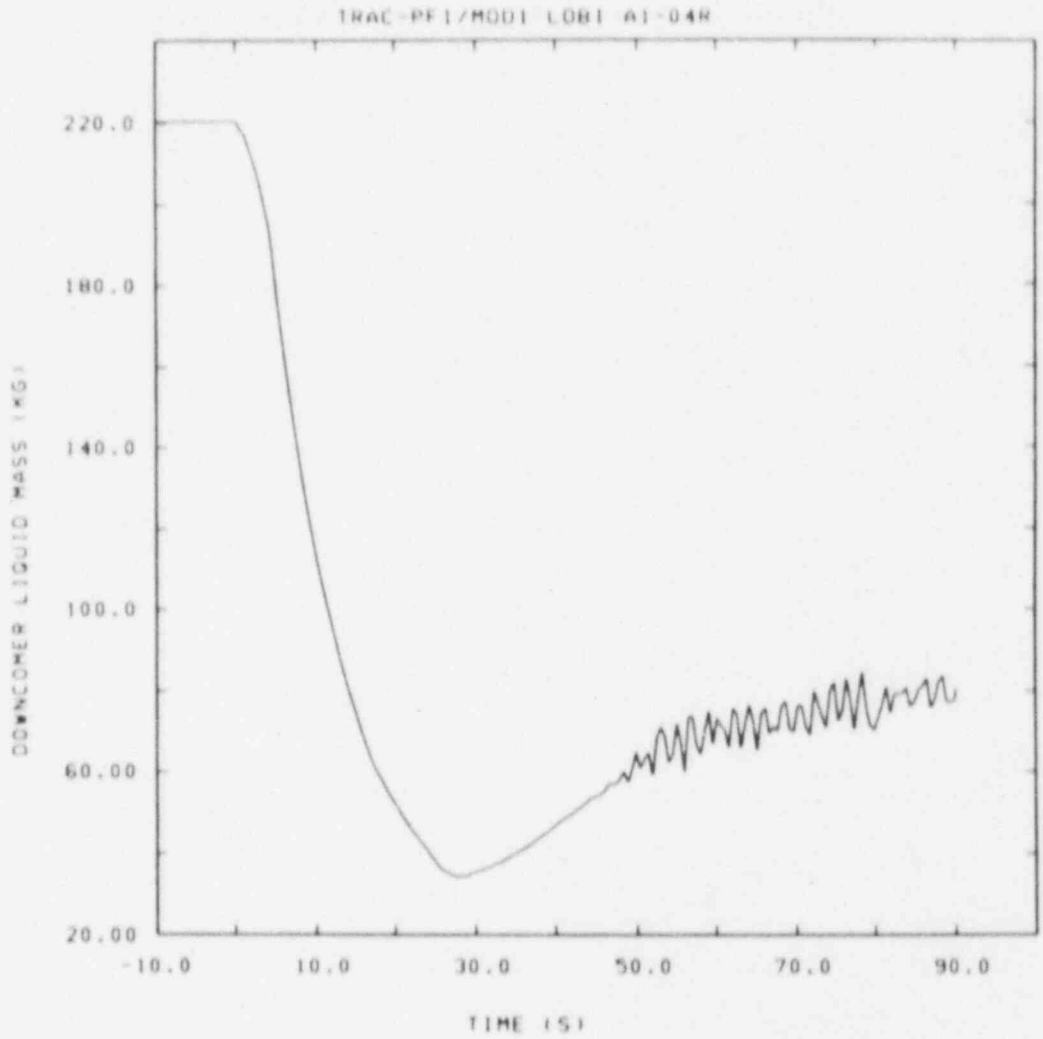

Figure 3.3.5 Downcomer Liquid Mass

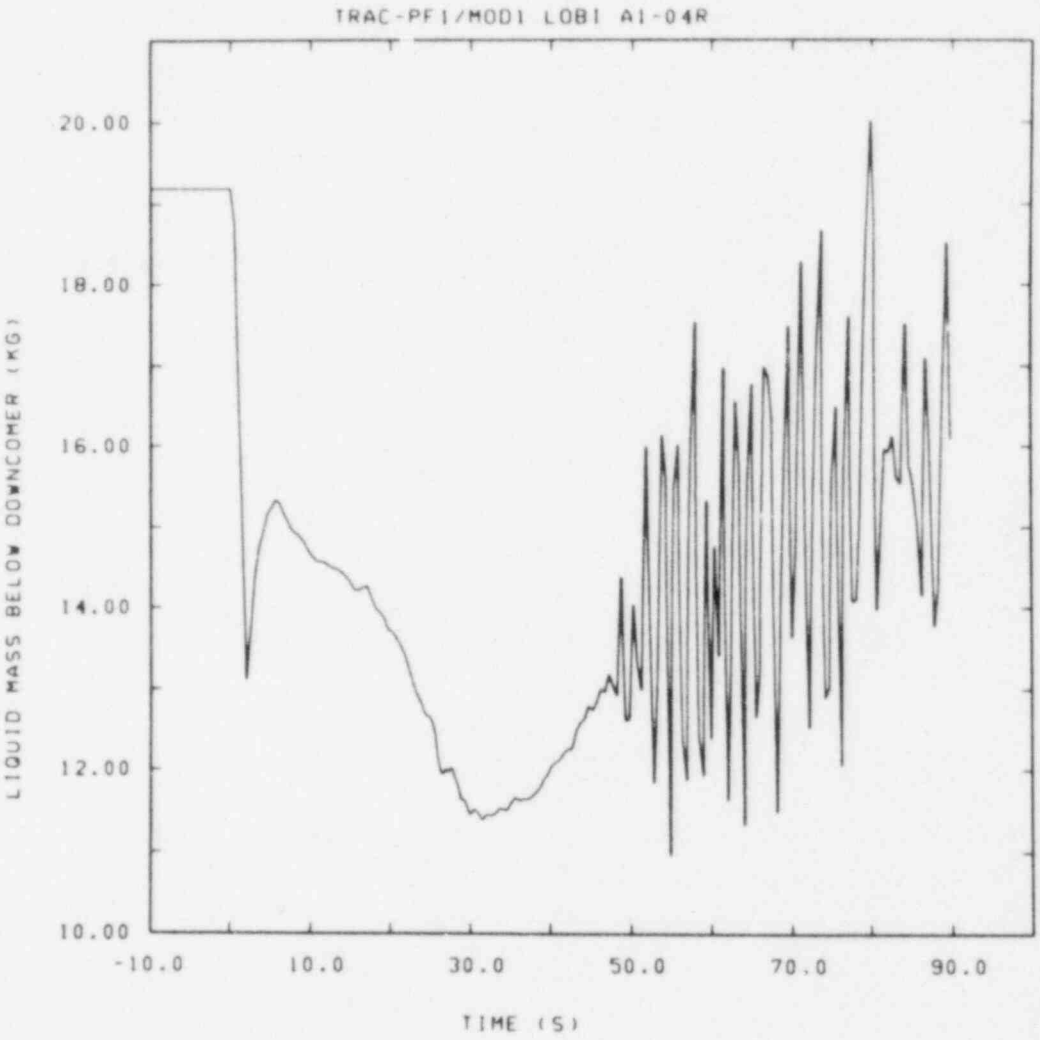

Figure 3.3.6 Lower Plenum Liquid Mass

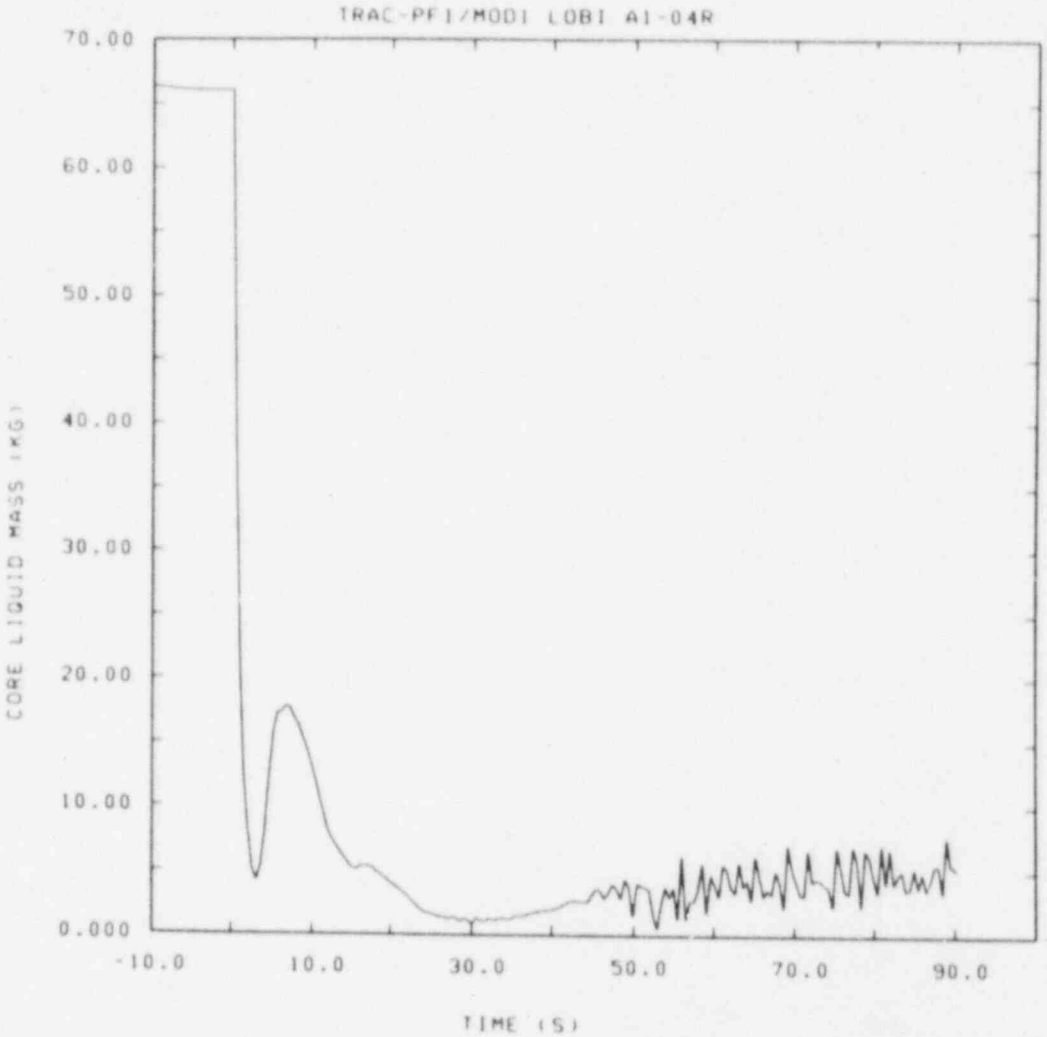

Figure 3.3.7 Core Liquid Mass

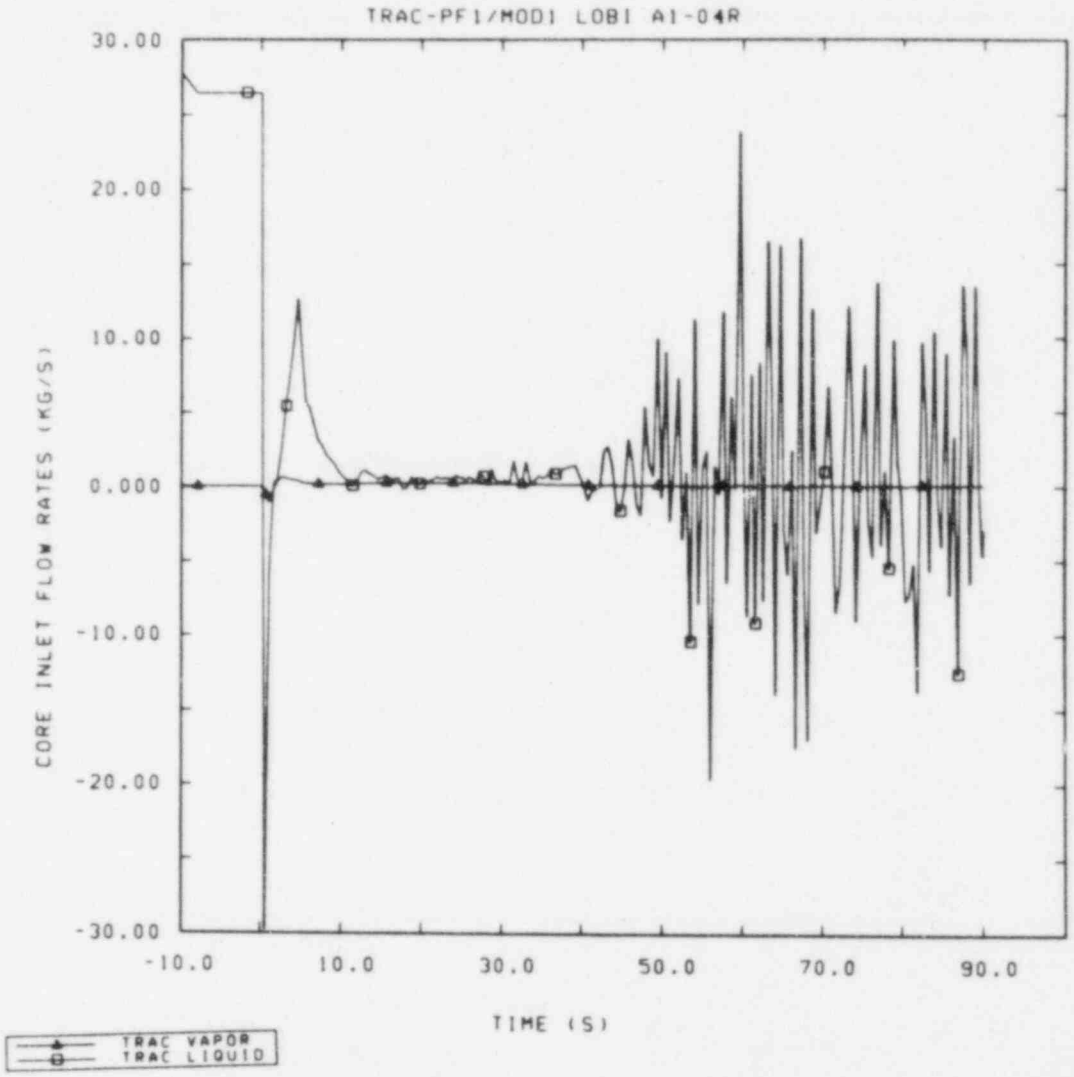

Figure 3.4.1 Core Inlet Liquid and Vapor Mass Flow Rates

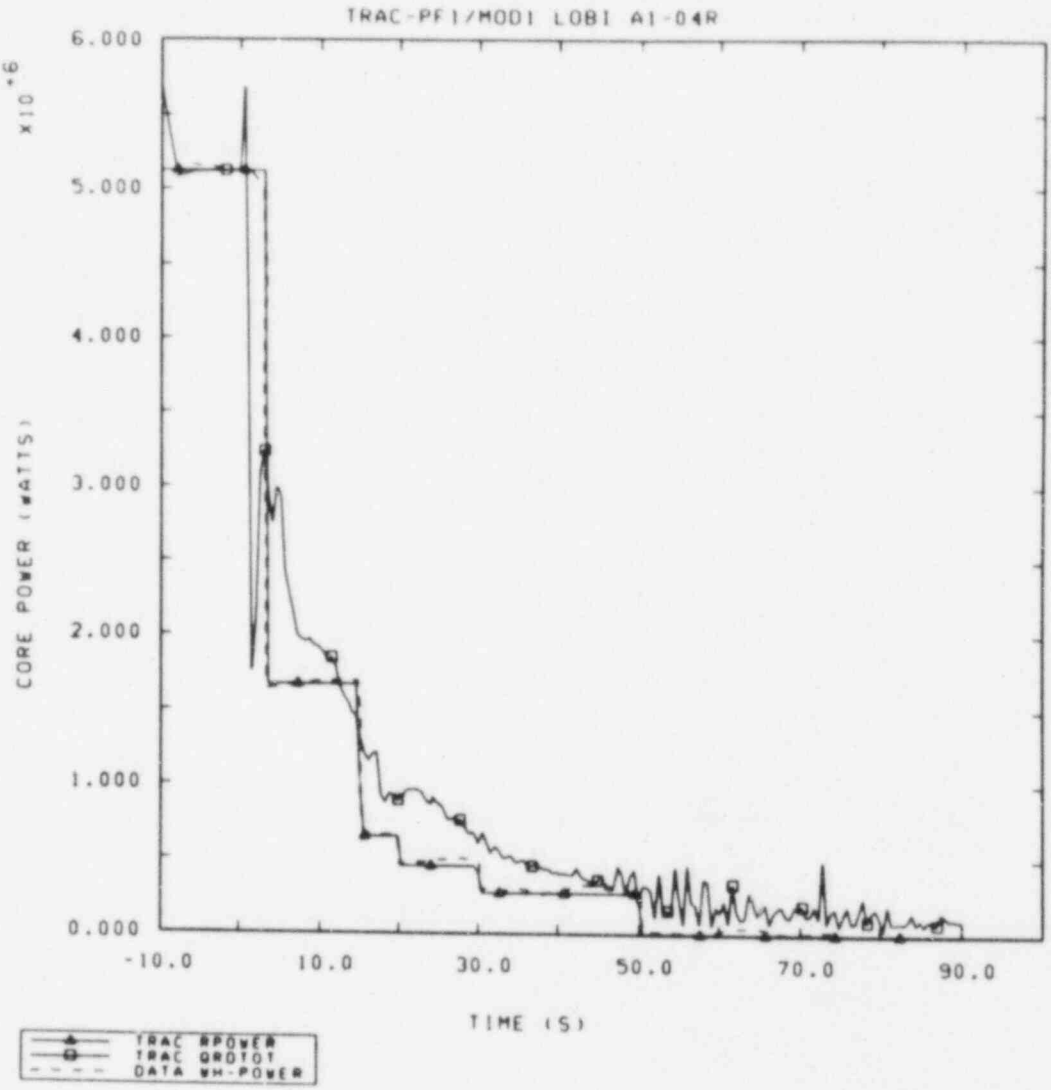

Figure 3.4.2 Core Power and Total Rod Heat Transfer Rate

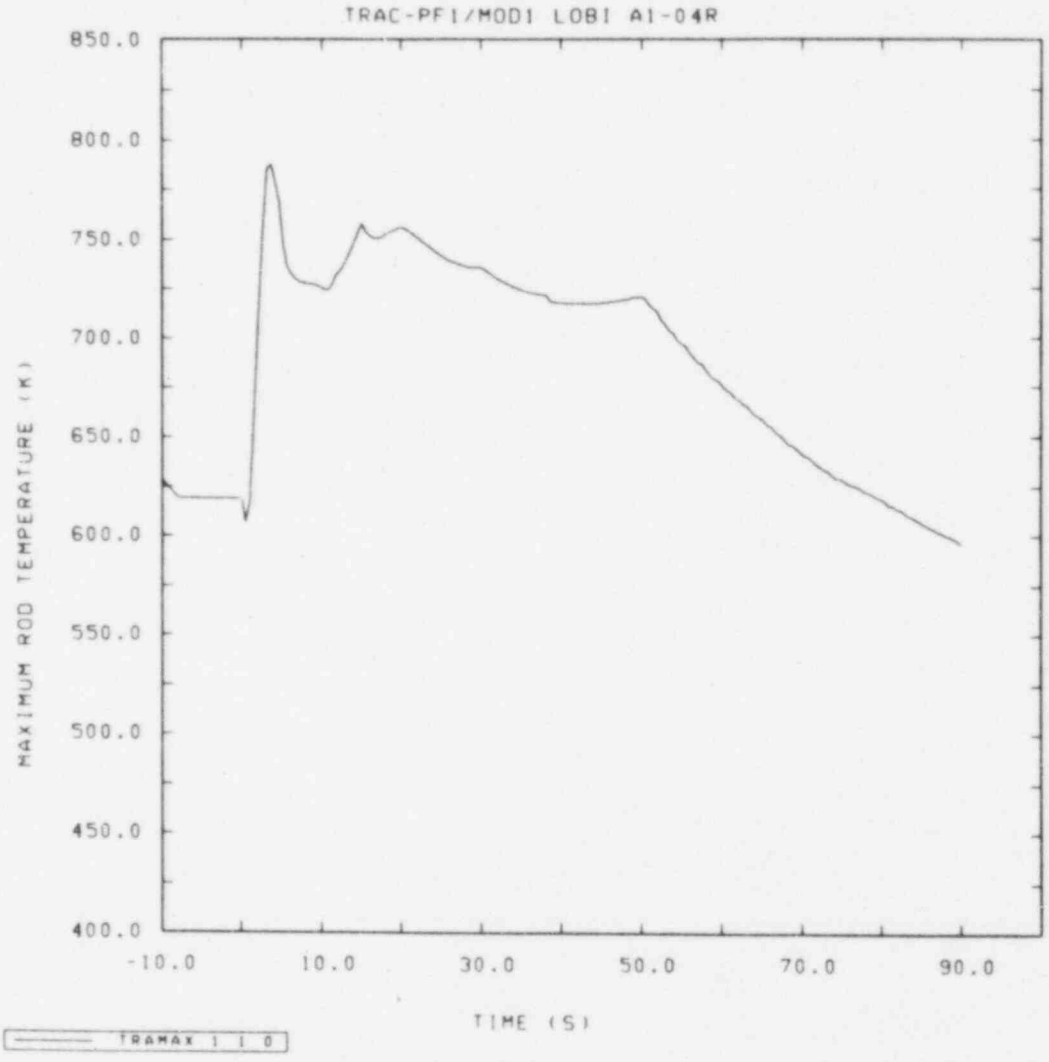

Figure 3.4.3 Maximum Heater Rod Temperature

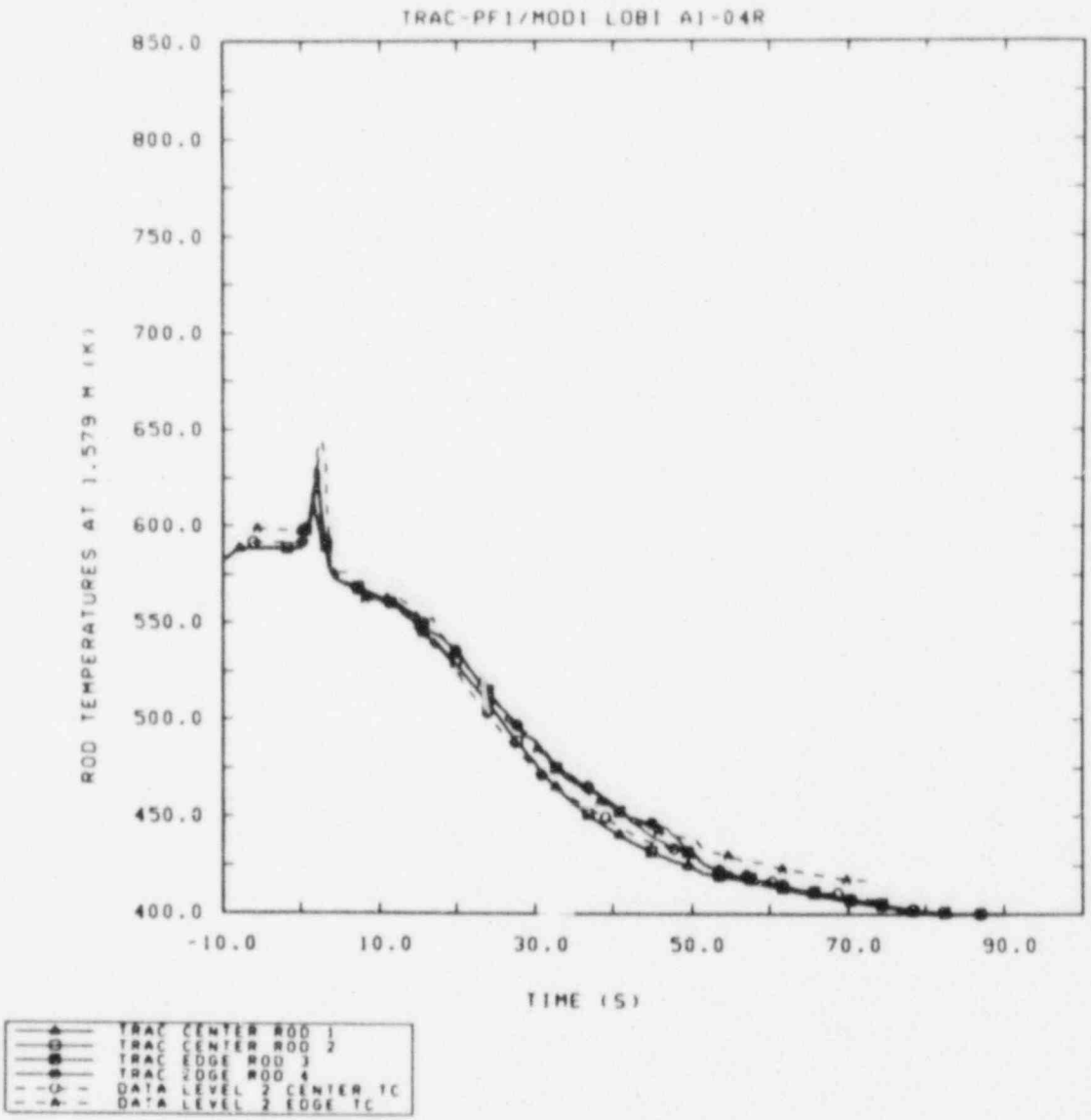

Figure 3.4.4 Heater Rod Temperatures at 1.5790 m Vessel Elevation

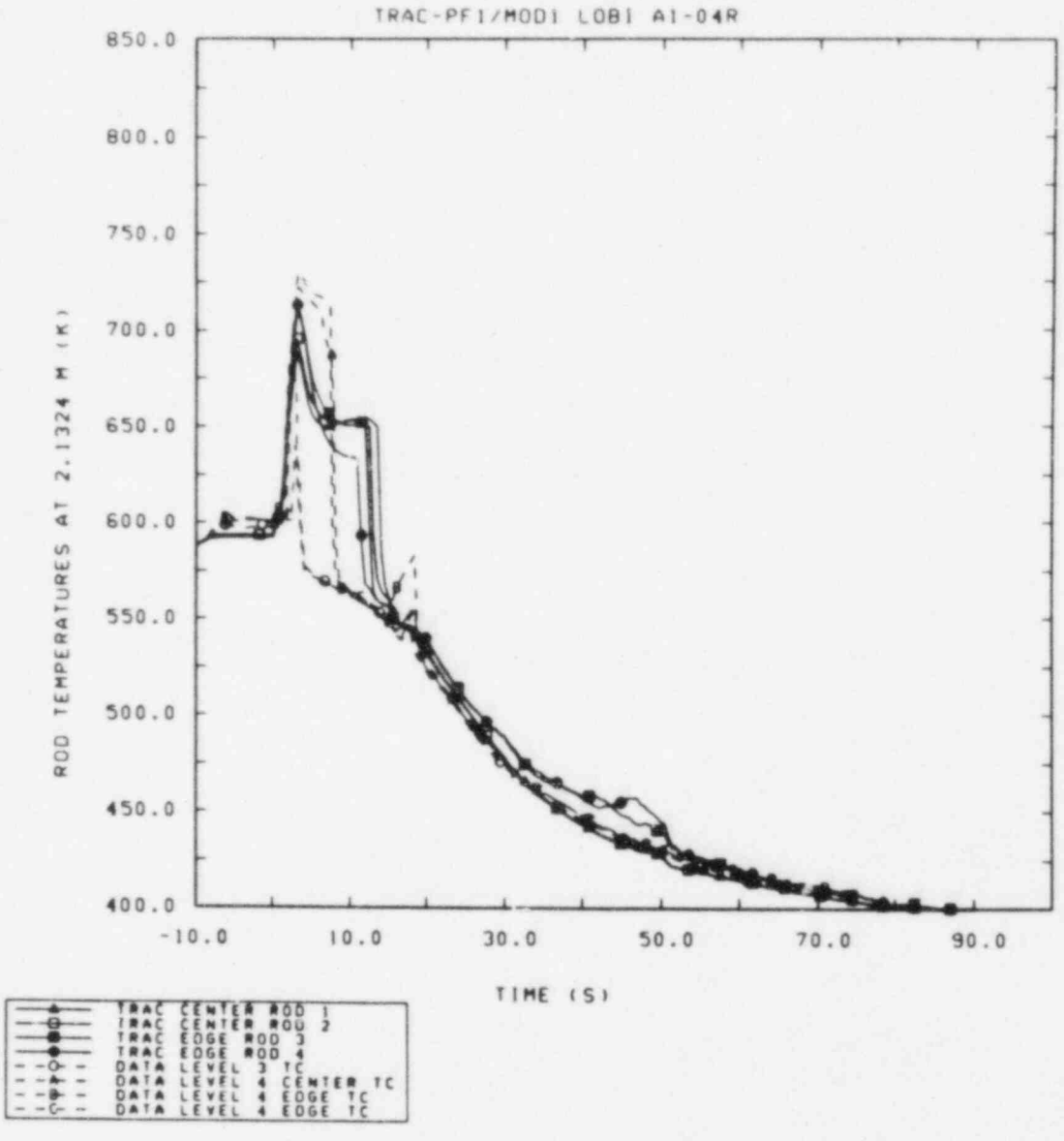

Figure 3.4.5 Heater Rod Temperatures at 2.1324 m Vessel Elevation

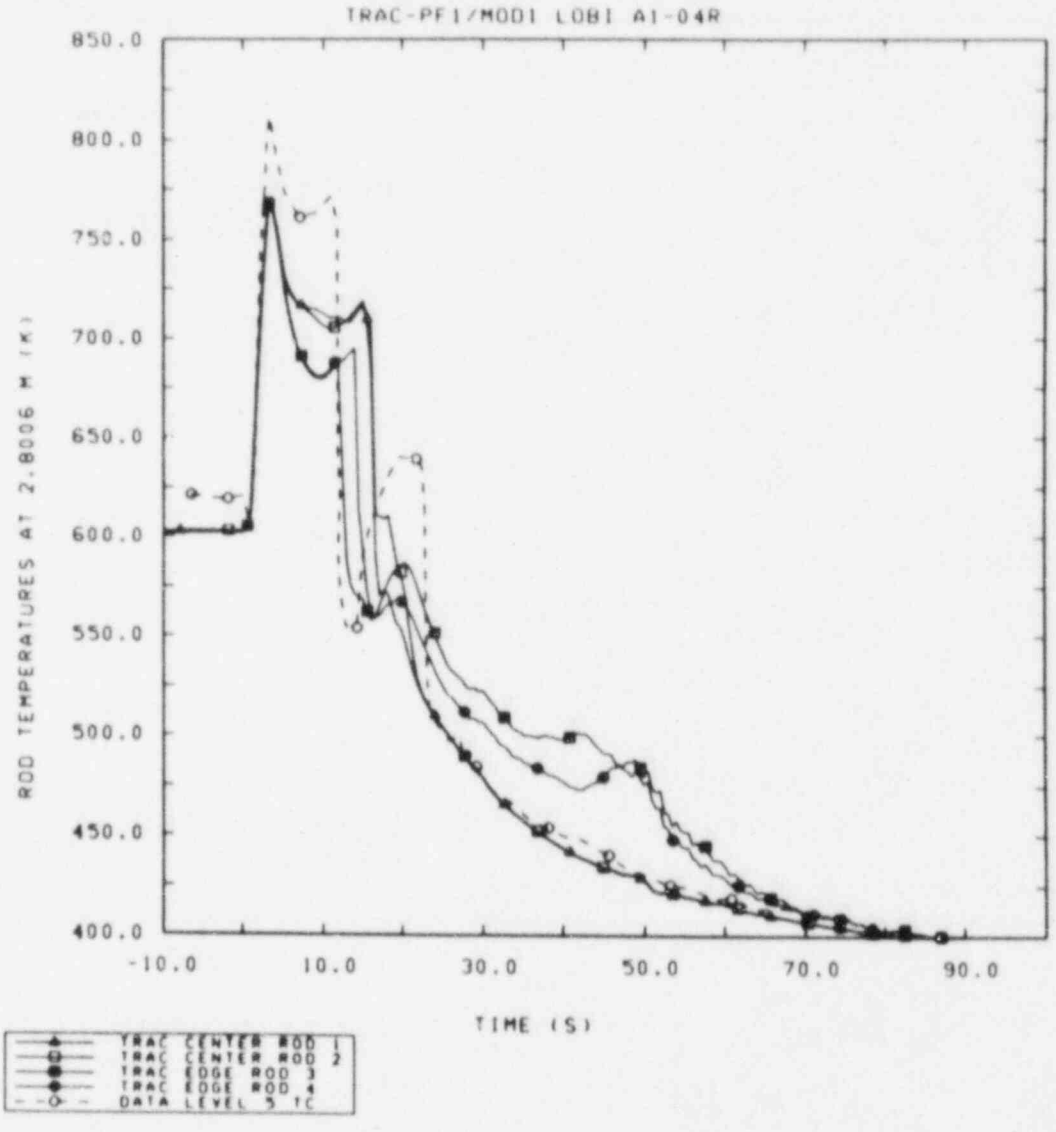

Figure 3.4.6 Heater Rod Temperatures at 2.8006 m Vessel Elevation

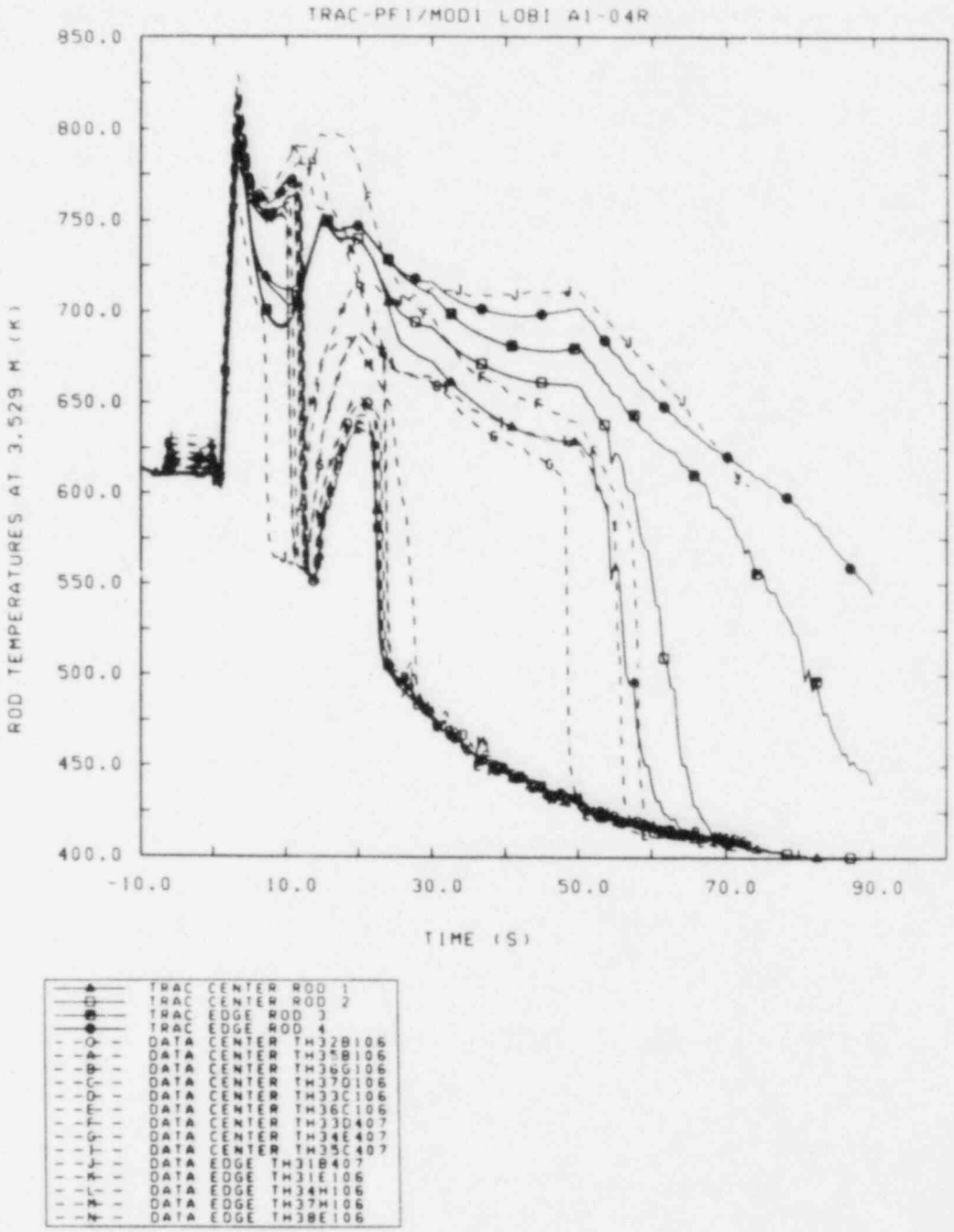

Figure 3.4.7 Heater Rod Temperatures at 3.5290 m Vessel Elevation

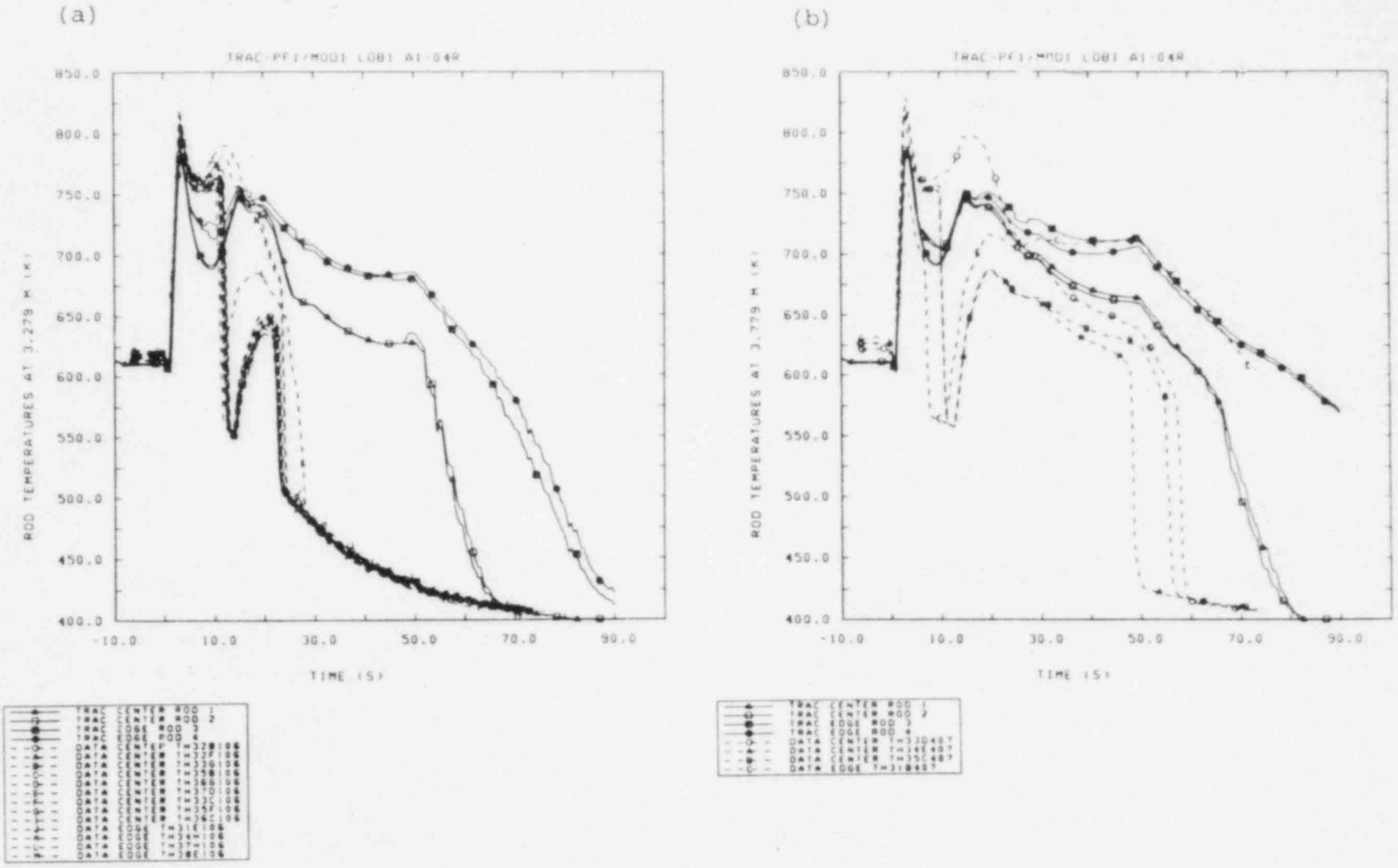

Figure 3.4.8 Heater Rod Temperatures at (a) 3.2790 and (b) 3.779 m Vessel Elevation

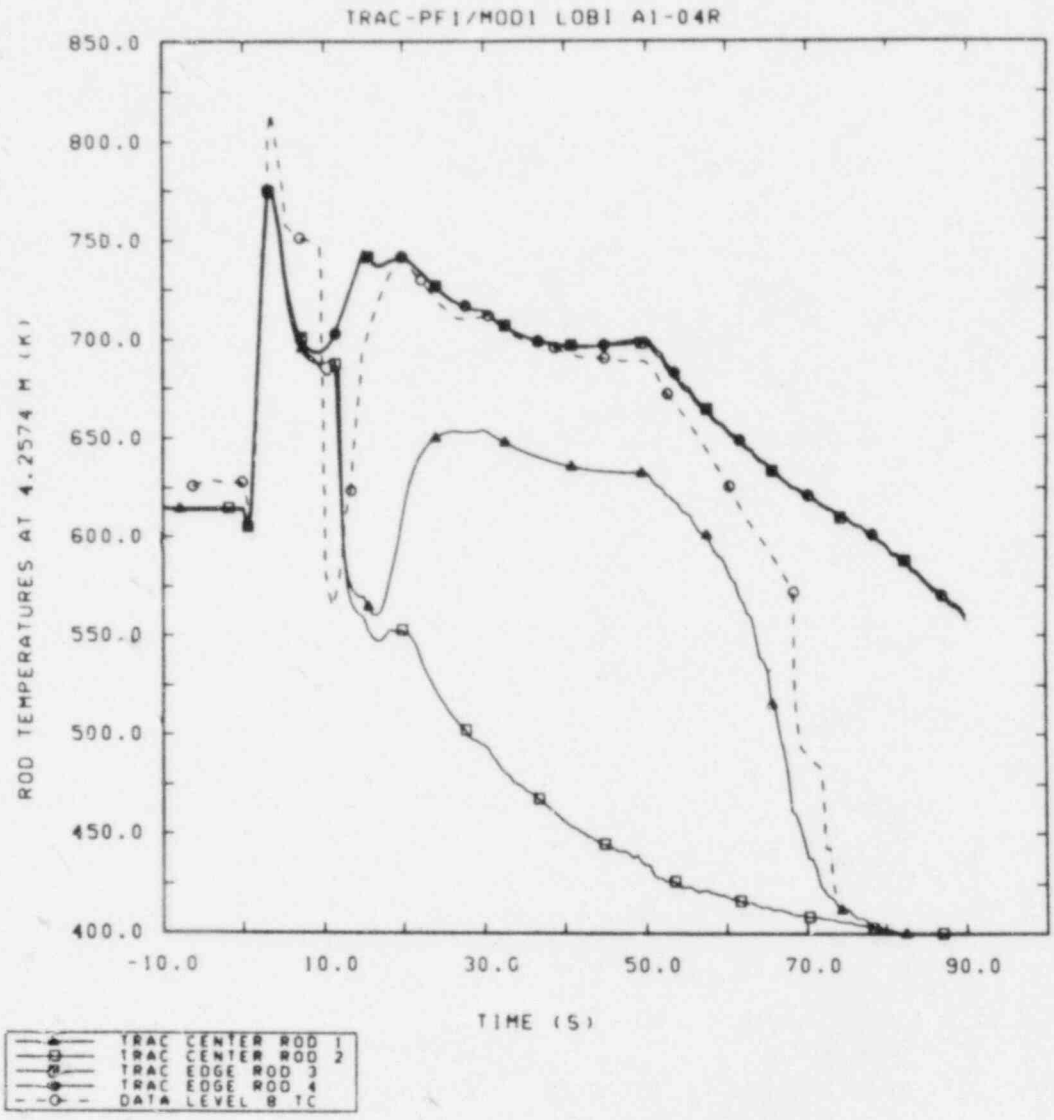

Figure 3.4.9 Heater Rod Temperatures at 4.2574 m Vessel Elevation

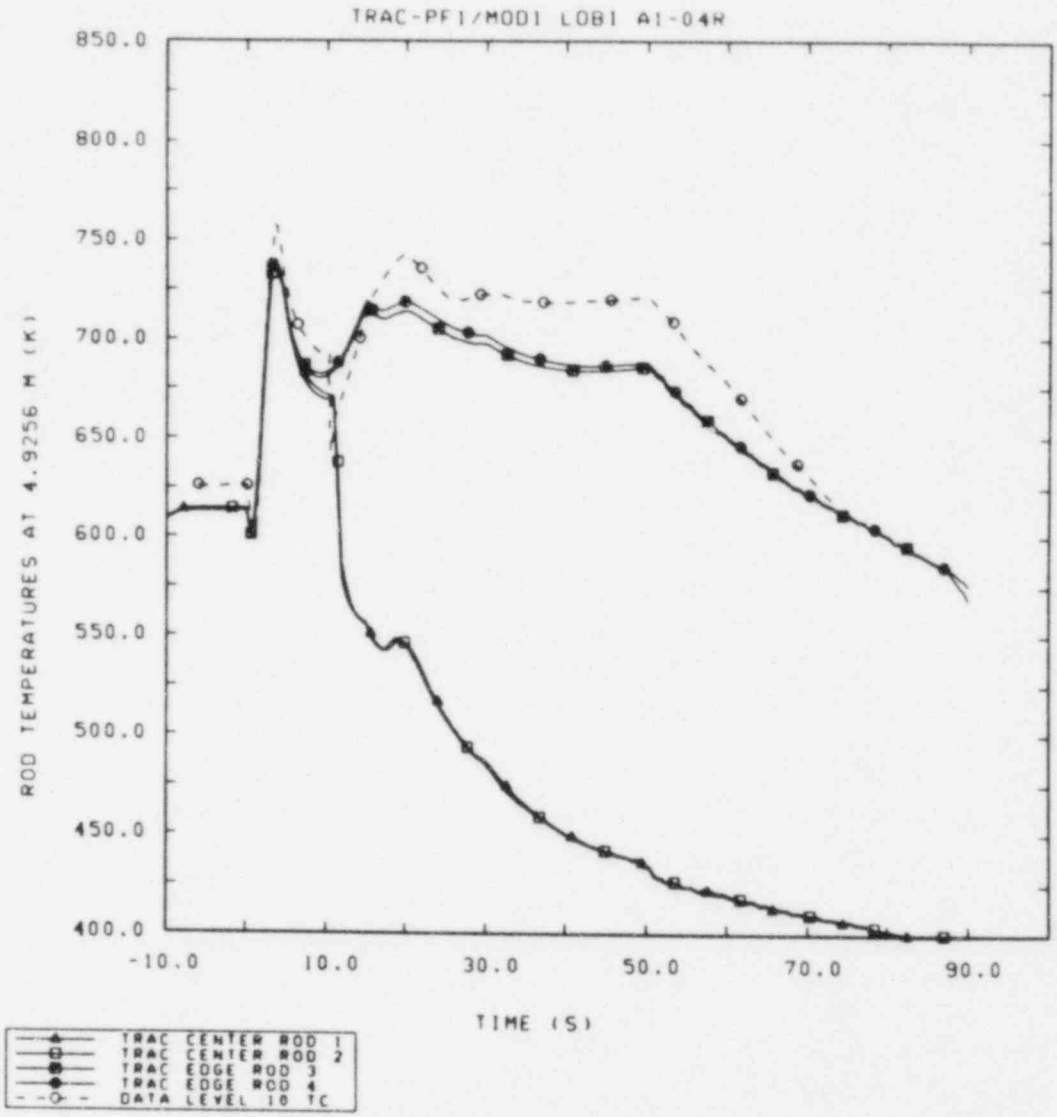

Figure 3.4.10 Heater Rod Temperatures at 4.9256 m Vessel Elevation

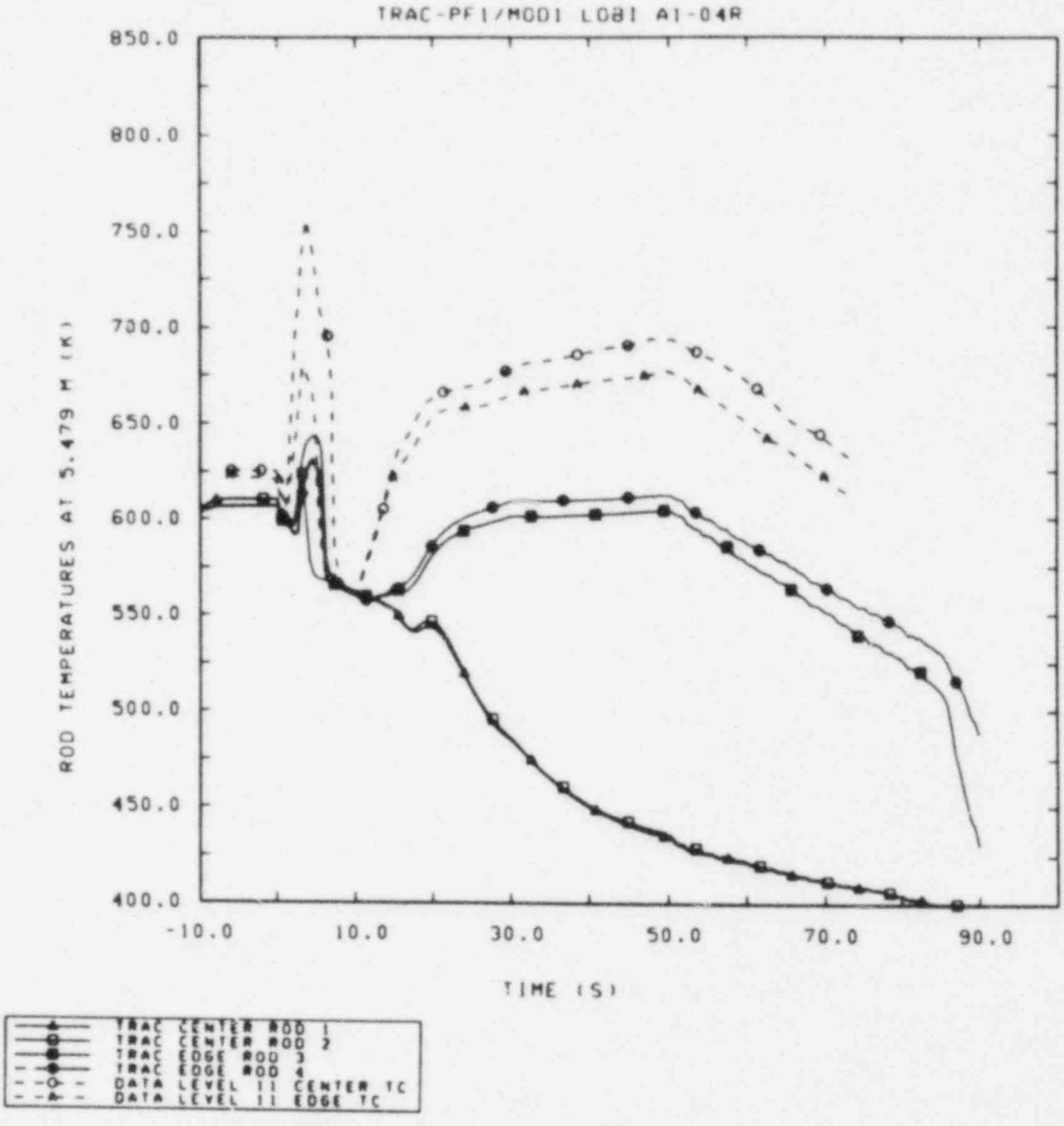

Figure 3.4.11 Heater Rod Temperatures at 5.479 m Vessel Elevation

4.0 BASECASE ANALYSIS DISCUSSION

Before discussing the results of some sensitivity studies we performed evaluating the impact of various input and/or modelling assumptions and values (given below in Section 5), some further discussion of the basecase transient results is presented in this section. In Section 3 we summarized the overall final transient results and, by comparing them to measured data, evaluated the ability of TRAC-PF1/MOD1 to correctly predict the physical phenomena dominating accident response in a large-break LOCA. In this section, differences in results and in run times due to machine variations are discussed; the basecase TRAC results are also briefly compared to the results of our previous RELAP5/MOD1 analyses of this same test.

4.1 CYBER-76 vs CRAY-1S Results

For reasons discussed below in Section 6.1, the A1-04R transient has been run on both the CYBER-76 and CRAY-1S computers at Sandia. Both calculations used the same input deck and the same code version, i.e., version 12.0 of TRAC-PF1/MOD1 with an additional Sandia-generated code update which corrected an error in the FILL component coding (discussed below in Section 6.3); neither calculation included the "FIX12" code updates later received from LANL. This allowed us to compare transient results and run times on the two machines for identical calculations. (We had not done any large, long comparison calculations on the two machines previously.)

While most of the calculated response (e.g., primary system pressures and accumulator injection) was virtually unchanged, two unexpected areas of difference were noted. The first of these involved some mass flow rates and was determined to be due only to an error in the graphics in the CRAY code version; this error is described in more detail in Section 6.4.

A potentially more serious discrepancy is seen in the core heater rod temperatures. Although all core levels show some very slight discrepancies between the CYBER and CRAY results, such variations are most readily visible in the middle region of the core. Some small differences are apparent at the 2.8006 m elevation, as can be seen by comparing the CRAY result shown in Figure 4.1.1 with the CYBER result in Figure 3.4.6.

The differences, in the late-time core temperatures in particular, can better be seen by comparing the heater rod temperatures at the core mid-plane in the CRAY run, shown in Figure 4.1.2, with those from the CYBER run shown in Figure 3.4.7. Both the two inner and the two outer rods in the CRAY

calculation have very similar temperatures while, in the CYBER run, each of the four rods has a very different temperature, particularly later in the transient.

Differences can also be seen easily in the heater rod temperatures at the 4.2574 m vessel elevation, by comparing the CRAY result shown in Figure 4.1.3 with the CYBER result shown in Figure 3.4.9. The CYBER calculation shows two inner rods rewetting completely at about 10 seconds and rod 1 then heating up again somewhat before cooling by the end of the transient. The CRAY run shows rod 1 rewetting completely at about 10 s and then generally remaining near the system saturation temperature except for a minor second heatup; in contrast, rod 2 heats up again after only partially rewetting and then remains relatively hotter until eventually cooling down at about the same time as rod 1 in the CYBER calculation. At this core level, besides the difference of two rods totally rewetting compared to only one in the inner core ring, the relative behaviors of rods 1 and 2 are reversed.

The different rod temperatures generally suggest some variance in the flow distribution being calculated in the vessel. The actual flow patterns are not compared because all components of the mass flow rate are not available edit or plot variables in a 3-D VESSEL component, and because the code logic for the mass flow rate signal variables does not allow for changes in the density donor-cell definition with changes in flow direction.

The reason for these differences is not known. The variations in rod temperatures between the CYBER and CRAY calculations are qualitatively and quantitatively similar to the variations seen between the CYBER basecase run and the preceding CYBER run, which had incorrect secondary side feedwater injection due to a code error (discussed further in Section 6.3). Changing the secondary feedwater flow did not result in any obvious differences in the calculated primary system response, particularly in and around the steam generators where some differences could have been expected. However, the change in feedwater flow apparently changed the calculation time step history slightly, resulting in small differences in the rod temperatures. Similar small differences in the time step history between the final CYBER and CRAY calculations may be the source of the discrepancies seen.

Neither of the calculations gives results that are obviously unphysical, or obviously more correct. However, the differences are worrisome because they suggest that the rod temperatures (particularly, the rod rewet and quench response at the core hot spot) are very sensitive to small differences in the vessel flow distribution. This in turn implies that the rod temperature

response may prove equally or more sensitive to the radial and azimuthal flow area fractions used, which are generally only educationally "guessed-at" values.

4.2 TRAC-PF1/MOD1 vs RELAP5/MOD1 Results

The results of our TRAC-PF1/MOD1 basecase analysis for the A1-04R test are generally comparable to those of our previous RELAP5/MOD1 calculations [3]. We have not crossplotted the RELAP5 and TRAC results because the various curves in such crossplots would be close enough together to make the plots hard to decipher. However, in this section, our earlier RELAP5 results are briefly summarized, for reference in discussing the TRAC vs RELAP5 results comparison.

Figure 4.2.1 shows the intact and broken loop cold leg pressures, and the pump-side and vessel-side break mass flow rates from our earlier RELAP5/MOD1 calculation. As can be seen by comparing these results to those calculated by TRAC-PF1/MOD1, shown in Figures 3.2.1 through 3.2.3, very similar break flow and primary pressure behavior were calculated, for similar break flow models in the two codes. However, the saturated break flow discharge coefficient used with RELAP5 was 0.85 rather than 1.0 as in TRAC; both analyses used subcooled break flow discharge coefficients of 1.0.

As discussed later in Section 5.4, similar accumulator injection flow rates were calculated by the two codes using very different user-input loss coefficients (for the same surge line lengths and flow areas). Figure 4.2.2 gives the accumulator injection flow rate, the intact loop fluid density and the liquid temperature downstream of the accumulator injection point from our RELAP5/MOD1 calculation, for comparison to the final TRAC-PF1/MOD1 results shown in Figures 3.3.1 through 3.3.3. For similar cold leg nodalizations, the RELAP5 downstream density and the TRAC downstream temperature are in better agreement with data respectively, although the differences are minor.

Another minor difference in the two codes' results is seen by comparing the RELAP5 intact and broken loop steam generator inlet and outlet temperatures shown in Figure 4.2.3 with the corresponding TRAC results shown in Figures 3.2.6 and 3.2.7. RELAP5/MOD1 generally calculated less vapor superheat by maintaining saturation conditions until all liquid had vaporized; TRAC-PF1/MOD1 in contrast generally has unequal liquid and vapor temperatures when both phases are present, so that nonequilibrium vapor superheat is calculated readily.

One major effect of these differences in calculating either equilibrium saturated liquid/vapor mixtures (in RELAP5/MOD1) or nonequilibrium saturated liquid/superheated vapor mixtures (in TRAC-PF1/MOD1) is seen in the late-time core rod temperature behavior, because the core in this test is recovered more by steam cooling than by reflood quenching. Figure 4.2.4 shows the lower core, mid-core and upper core rod temperatures from the RELAP5/MOD1 calculation. To facilitate comparison, the TRAC rod temperatures shown in Figures 3.4.3 through 3.4.10 have been replotted in the same abbreviated form in Figure 4.2.5 (but with different time scales); of the four rods in the TRAC model, rod 3 was used for these summary plots.

The (blowdown) PCT predicted by RELAP5/MOD1 (820 K) is in much better agreement with data than the final TRAC result, and lies within the experimental uncertainty of $\pm$3 K; the better agreement is probably because the staggered hollow-rod geometry could be explicitly modelled by RELAP5 and only approximated by TRAC. RELAP5/MOD1 predicted a larger core rewet at 5-15 s than that measured while TRAC-PF1/MOD1 gave a smaller partial core rewet in the same time period (for similar core bypass flows).

The rod temperatures calculated at later times by TRAC are in better agreement with data than those from RELAP5/MOD1 (which does not have a moving-fine-mesh reflood model); RELAP5 generally predicted a more uniform cooldown throughout the entire core, particularly visible in the mid-core region, rather than a quench front progressing up the core as actually observed. The absence of any sustained hot leg superheat in the RELAP5/MOD1 analysis indicates that the core is being cooled mostly by the heatup of a saturated two-phase mixture rather than mainly by the generation of superheated vapor within a two-phase mixture.

4.3 Computational Run Time

As shown in Figure 4.3.1, 90 seconds of the A1-04R transient calculation with TRAC required ~7250 seconds of CPU time on our CYBER-76. The ten seconds of steady state were much faster running than the transient, as would be expected. The time step was reduced, by input, to 10^{-4} s at "trouble spots", i.e., at times when phenomena were changing extremely rapidly such as the opening of the break valves and the onset of accumulator injection. Code failures were common at these points when no such adjustment was made, because the code could not adequately foresee the changing conditions and automatically reduce the time step quickly enough. These time step reductions did not add substantially to the overall run time and helped avoid the necessity of reruns with progressive time step reductions.

Figure 4.3.2 shows the time step used during the CYBER calculation. The apparent decrease in time step before transient start is an artifact of the plot edit frequency. There is a substantial time step decrease early in the transient, prior to 10 s, followed by a rapid time step increase to more than half of its steady-state (Courant-limited) value at about 10 seconds; afterwards, the time increment slowly decreases, with a brief user-imposed time step reduction at ~25 s due to the onset of accumulator injection. The time step drops then more or less continuously until the accumulator water begins appearing in the core at about 45 s. The resulting manometric flow oscillations being calculated (described in Section 3.3) are accompanied by large oscillations in the time step.

The same calculation was somewhat faster running on a CRAY-1S, as shown in Figure 4.3.3. The total CRAY CPU time was ~5200 seconds, with over ~5050 seconds of CPU time used for the 90 seconds of transient. In this calculation also, the time step was reduced to 10^{-4} s at the same expected trouble spots, using the same input. Figure 4.3.4 shows the time step used during the CRAY calculation. The overall behavior is very similar to that seen in the CYBER calculation, given in Figure 4.3.2, with the time steps appearing slightly different in portions of the transient; the plots may appear to be more different than they actually are because of a plot edit frequency which is too large to display all the oscillatory behavior. The small differences in time steps may cause the different core behavior in the two calculations discussed in Section 4.1, or may be a result thereof.

The various run time statistics on the two computers are summarized in Table 4.3.1. The overall results are somewhat surprising. We expected the CRAY version of the code to run about a factor of 2 or so faster than the CYBER version, especially since the CRAY version is not overlaid; instead the speed-up is only a factor of 1.4. Upon further investigation, we discovered that our CRAY version of the code had been inadvertently compiled with vectorization turned off. Test calculations done since that run was made suggest that vectorization causes a 35% speedup, so a production calculation with vectorization on should run nearly two times faster on the CRAY than on the CYBER, as originally expected.

Table 4.3.1 also gives the RELAP5/MOD1 run time statistics [3]. That calculation took ~10800 seconds of CPU time on our CYBER-76. As with the TRAC calculations, the ten seconds of steady state were much faster running than the transient portion of the calculation. During most of the transient (after 20 s), the time step was held down to a maximum of 2.5 ms via user input in order to eliminate spurious temperature oscillations in the steam generators; those oscillations, if not controlled,

were severe enough to eventually abort the calculation. Because of this drastic time step reduction (which we made no attempt to optimize), the RELAP5/MOD1 transient calculation was much slower running than the equivalent TRAC calculation. However, the "grind time" for the RELAP5 analysis is substantially smaller than for TRAC. The major reason for this is probably that TRAC, during most of the transient, is averaging two-to-three outer iterations per time step, in effect increasing the "number of time steps" used in the calculation; this increased number of effective time steps is not reflected in the table's grind time computation. (Because of the greatly user-reduced time step in our previous RELAP5/MOD1 calculation, RELAP5 is repeating less than 1% of its attempted time steps; a large number of repeated time steps should also show up as an increased grind time if only the number of successful time steps is used to calculate the RELAP5 run time efficiency.)

Table 4.3.1 Run Time Statistics

	CYBER-76		CRAY-1S		RELAP5/MOD1 (CYBER)	
	St.St.	Trans.	St.St.	Trans.	St.St.	Trans.*
Problem Time (s)	10.0	90.0	10.0	90.0	10.0	80.0
CPU Time (s)	227.	7278.	149.	5069.	234.	10773.
Number of Time Steps	237	5702	237	5652	817	33746.
Average Time Step Size (ms)	42.2	15.8	42.2	15.9	12.3	2.40
CPU-Time/Problem-Time	22.7	80.9	14.9	56.3	23.4	135.
CPU-Time/Problem-Time/Cell	0.09	0.32	0.06	0.22	0.13	0.72
CPU-Time/Time-Step (s)	0.96	1.28	0.63	0.90	0.29	0.32
CPU-Time/Time-Step/Cell (ms)	3.74	4.99	2.46	3.50	1.54	1.71

* Time step held down by user to a maximum of 2.5 ms after 20 s of transient to prevent divergent temperature oscillations

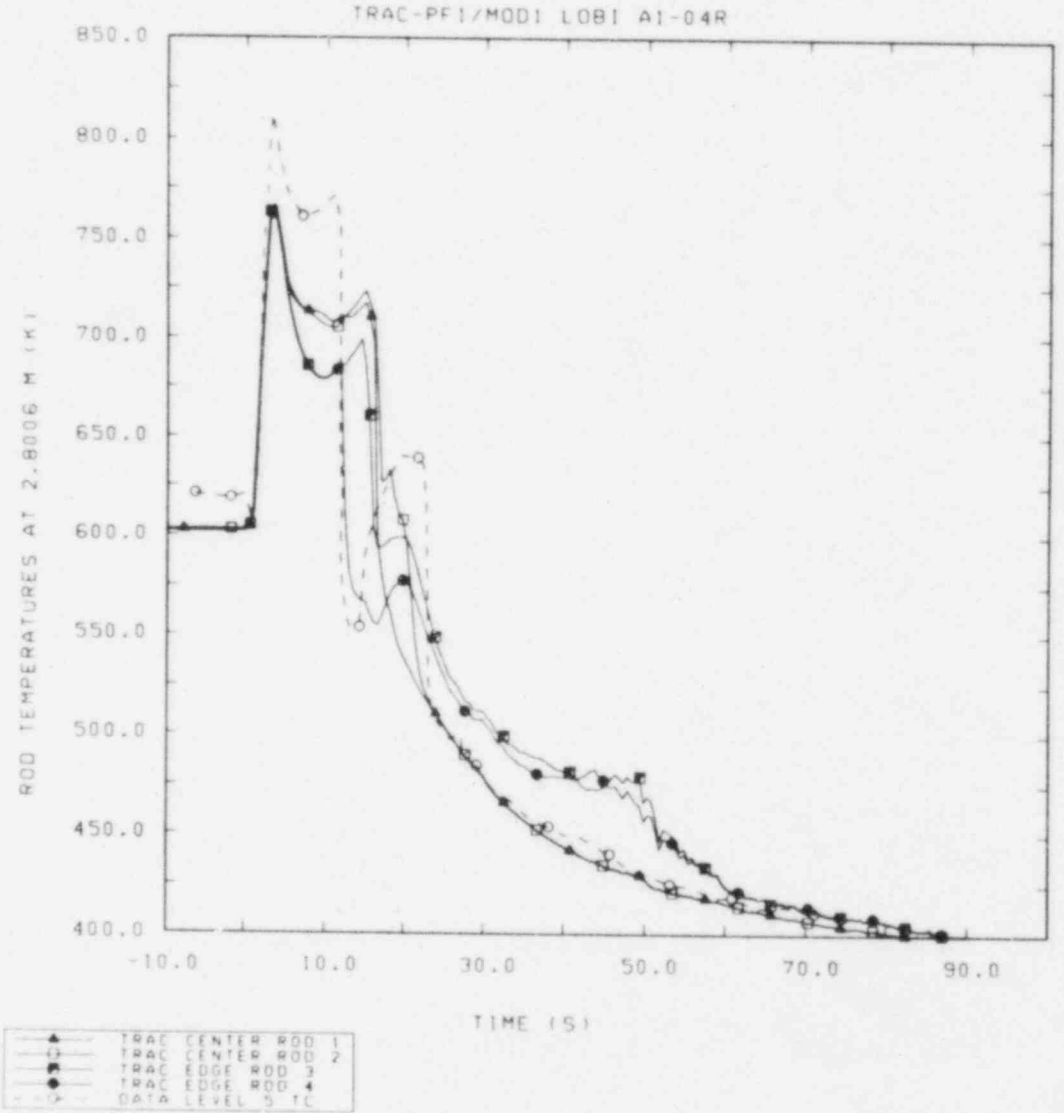

Figure 4.1.1 Heater Rod Temperatures at 2.8006 m Vessel Elevation from CRAY-1S Run

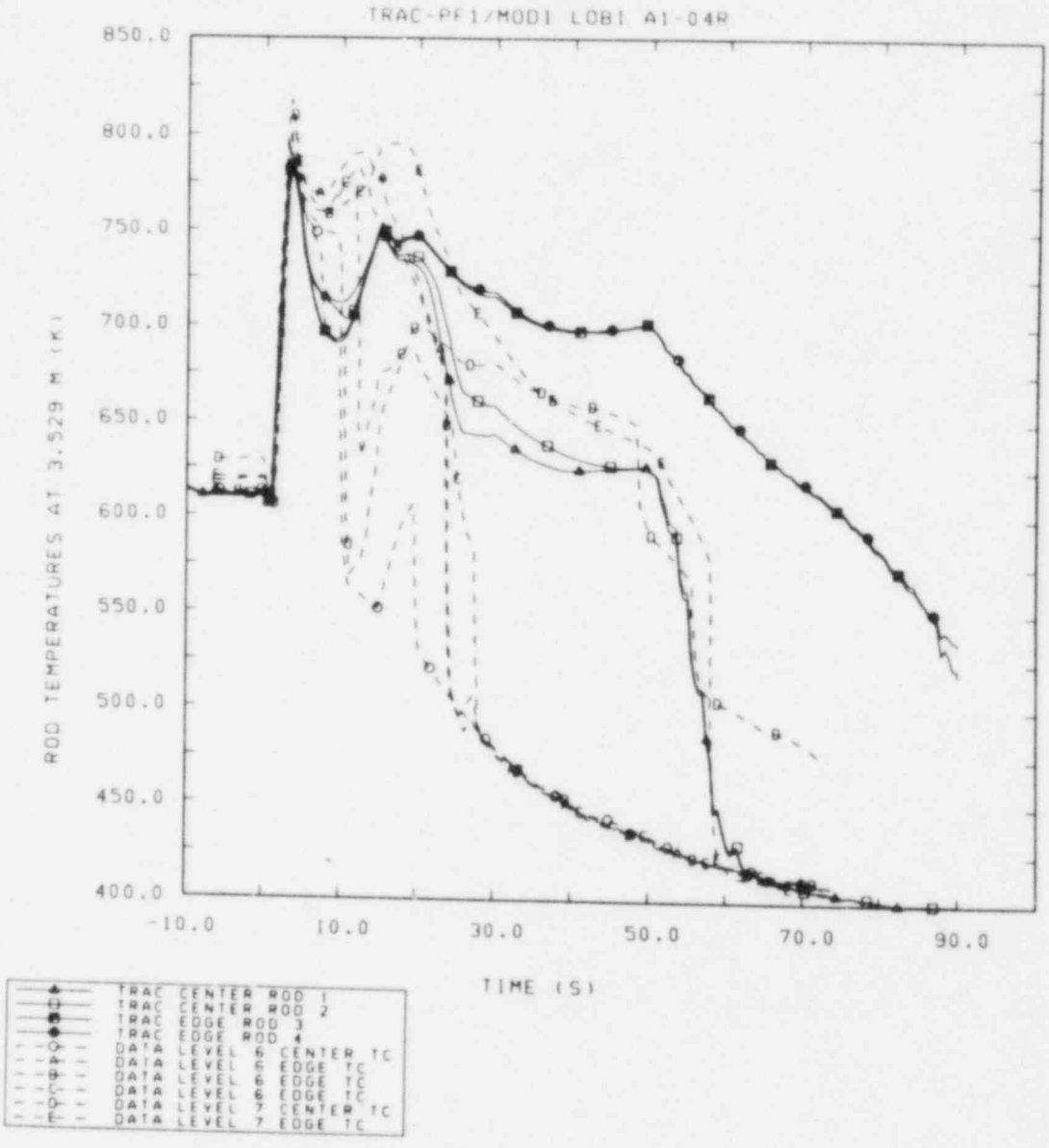

Figure 4.1.2 Heater Rod Temperatures at 3.5290 m Vessel Elevation from CRAY-1S Run

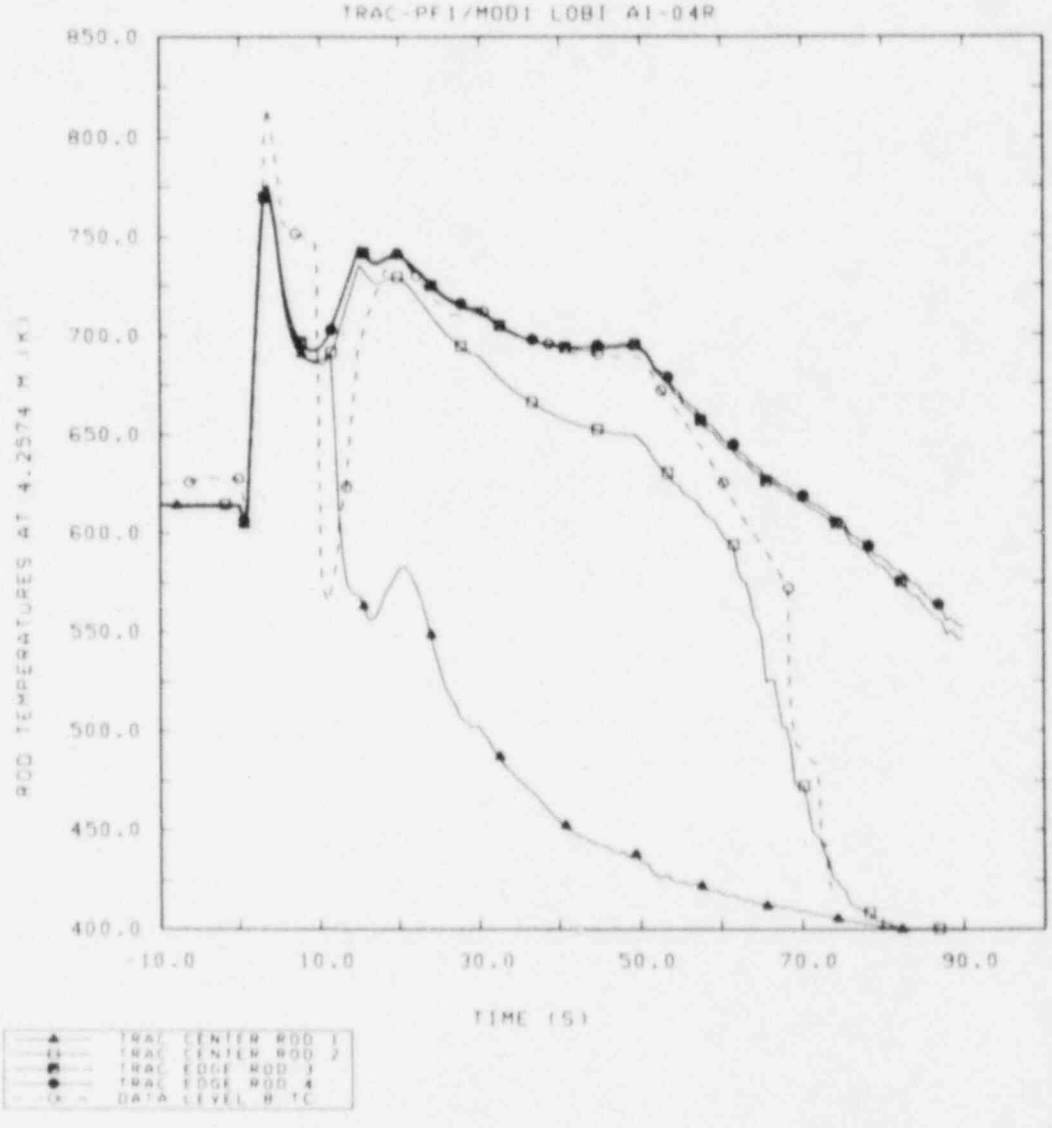

Figure 4.1.3 Heater Rod Temperatures at 4.2574 m Vessel Elevation from CRAY-1S Run

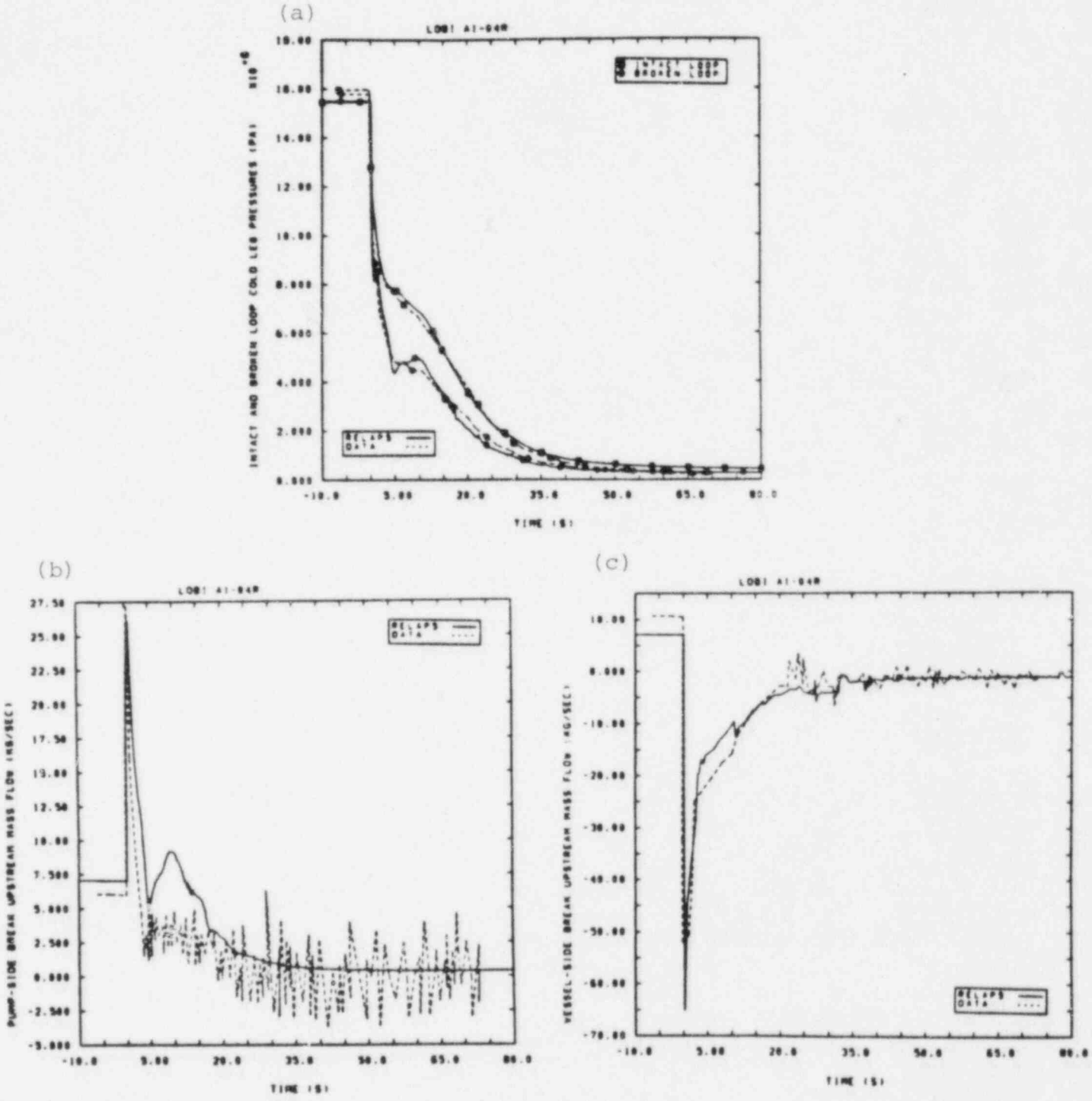

Figure 4.2.1 (a) Intact and Broken Loop Cold Leg Pressures, (b) Pump-Side and (c) Vessel-Side Break Mass Flow Rates from RELAP5/MOD1 Calculation

(a)

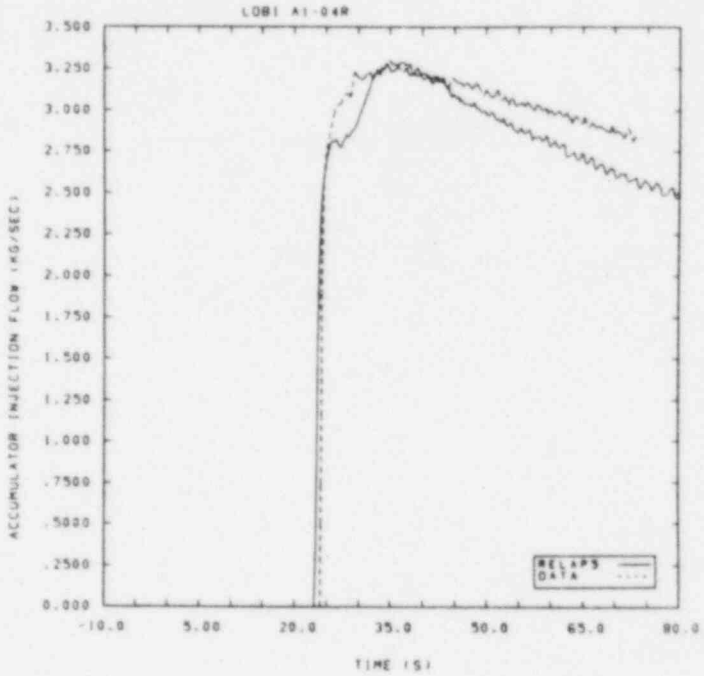

(b)

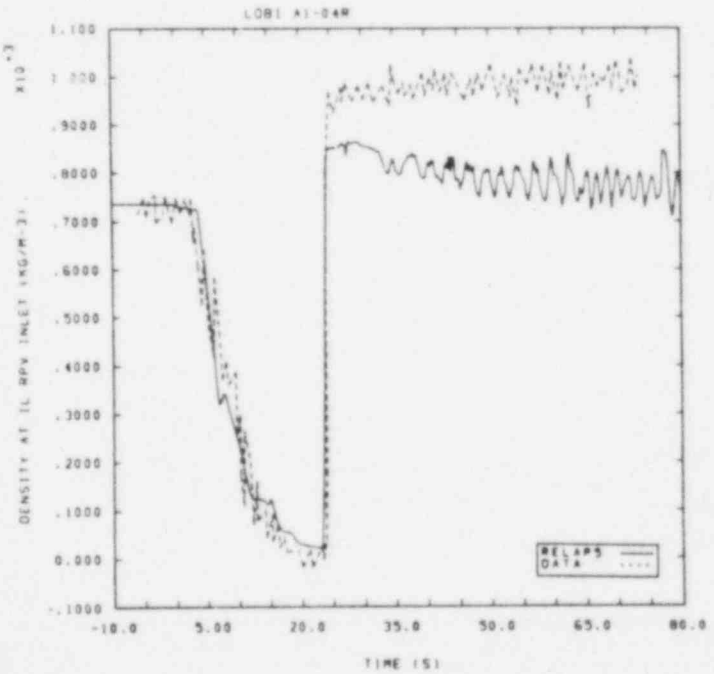

(c)

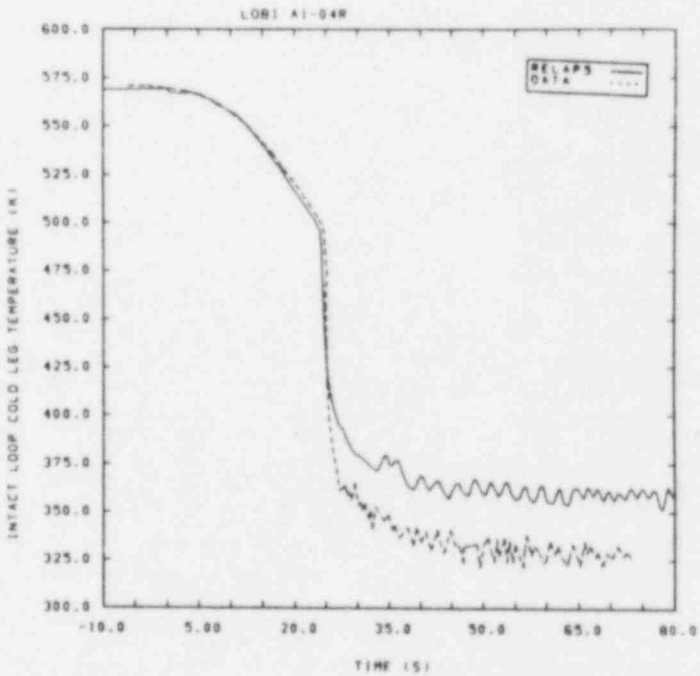

Figure 4.2.2 (a) Accumulator Injection Rate, and Intact Loop (b) Fluid Densities and (c) Temperatures Downstream of Accumulator Injection Point from RELAP5/MOD1 Calculation

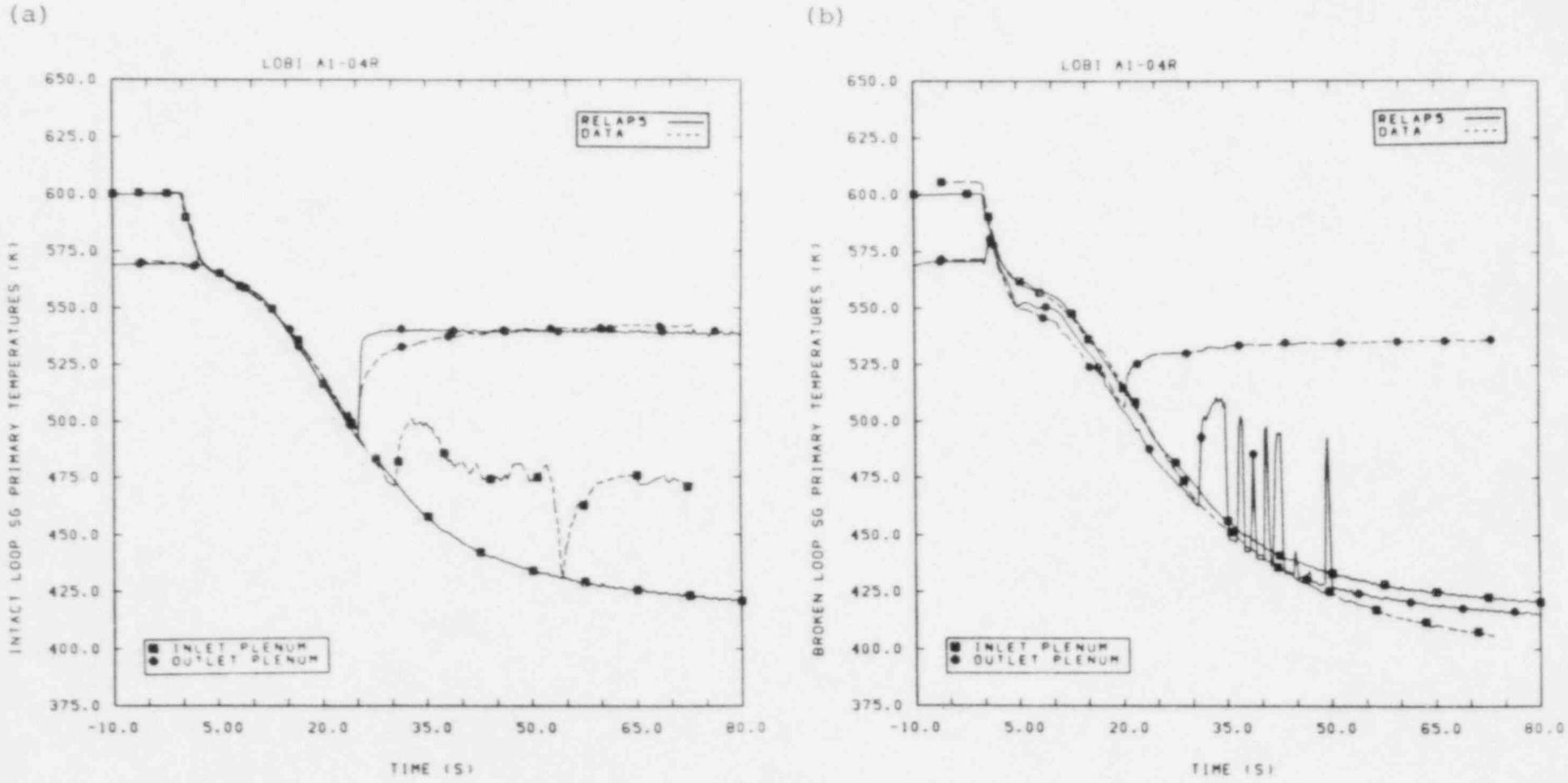

Figure 4.2.3 (a) Intact and (b) Broken Loop Steam Generator Inlet and Outlet Temperatures from RELAP5/MOD1 Calculation

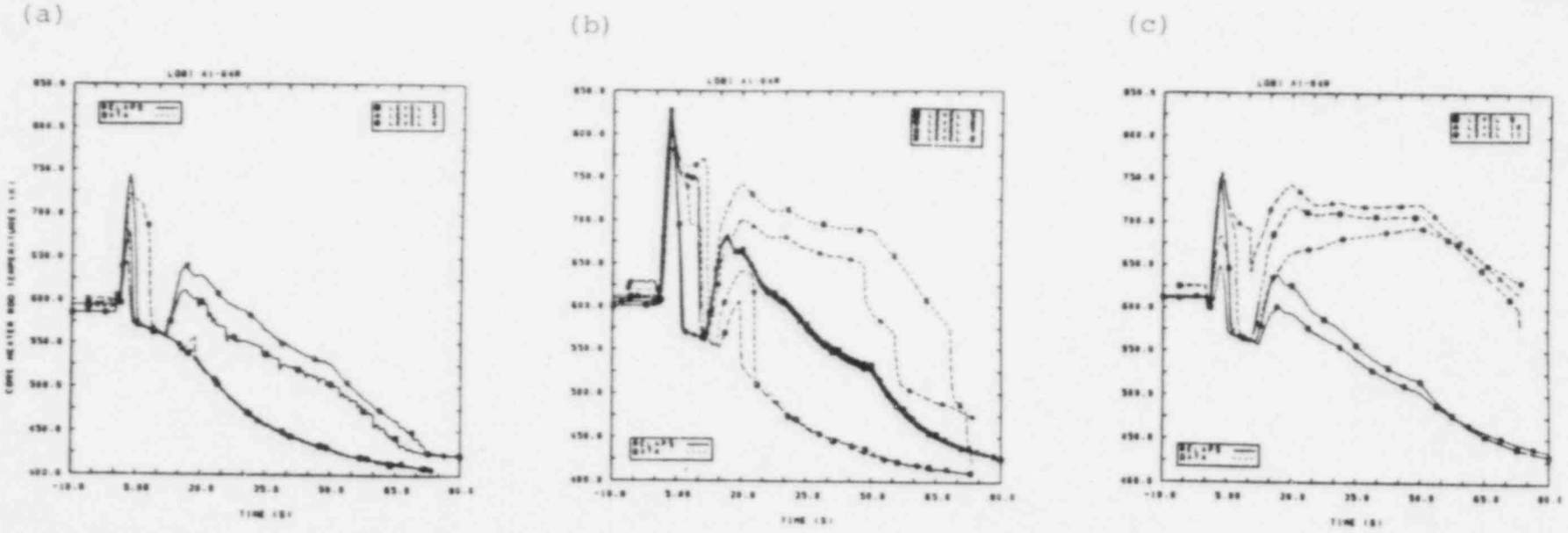

Figure 4.2.4 (a) Lower Core, (b) Mid-Core and (c) Upper Core Rod Temperatures from RELAP5/MOD1 Calculation

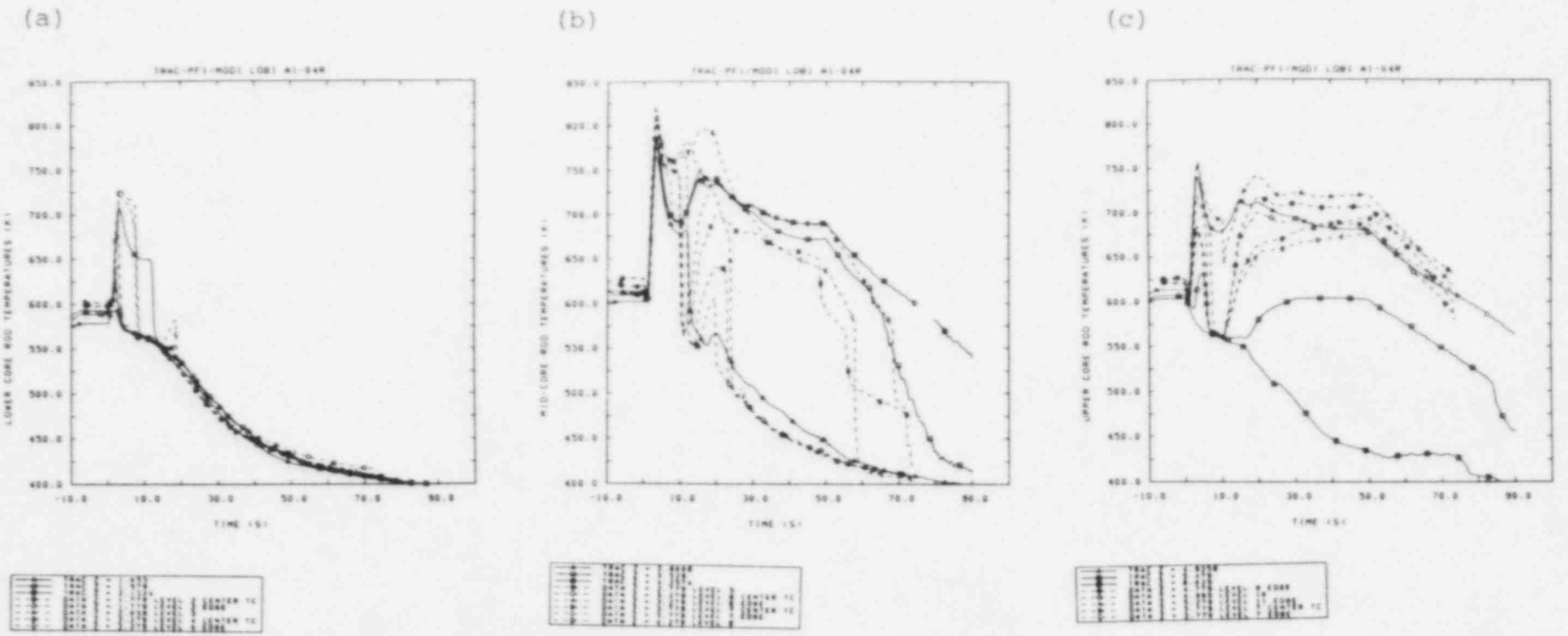

Figure 4.2.5 (a) Lower Core, (b) Mid-Core and (c) Upper Core Rod Temperatures from TRAC-PF1/MOD1 Calculation

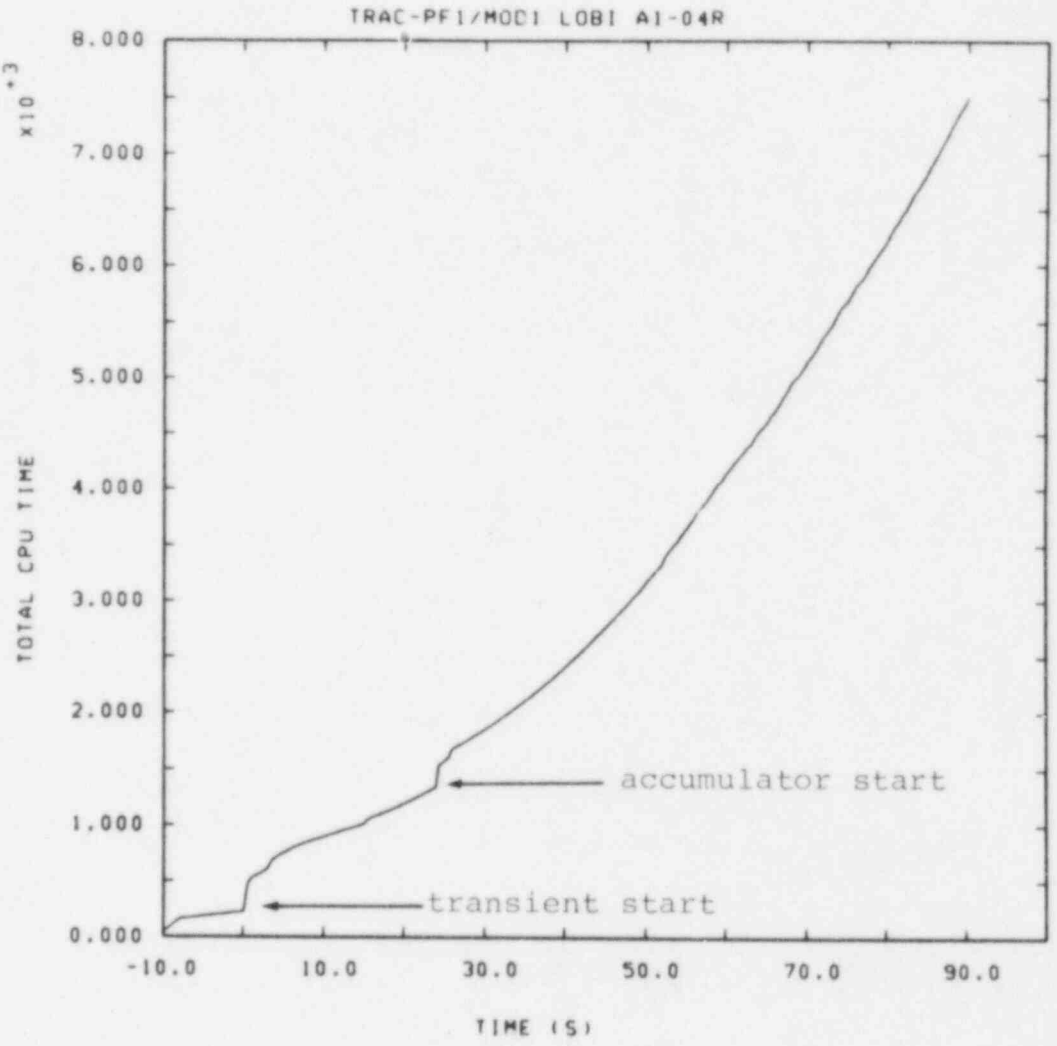

Figure 4.3.1 Total CYBER-76 CPU Time

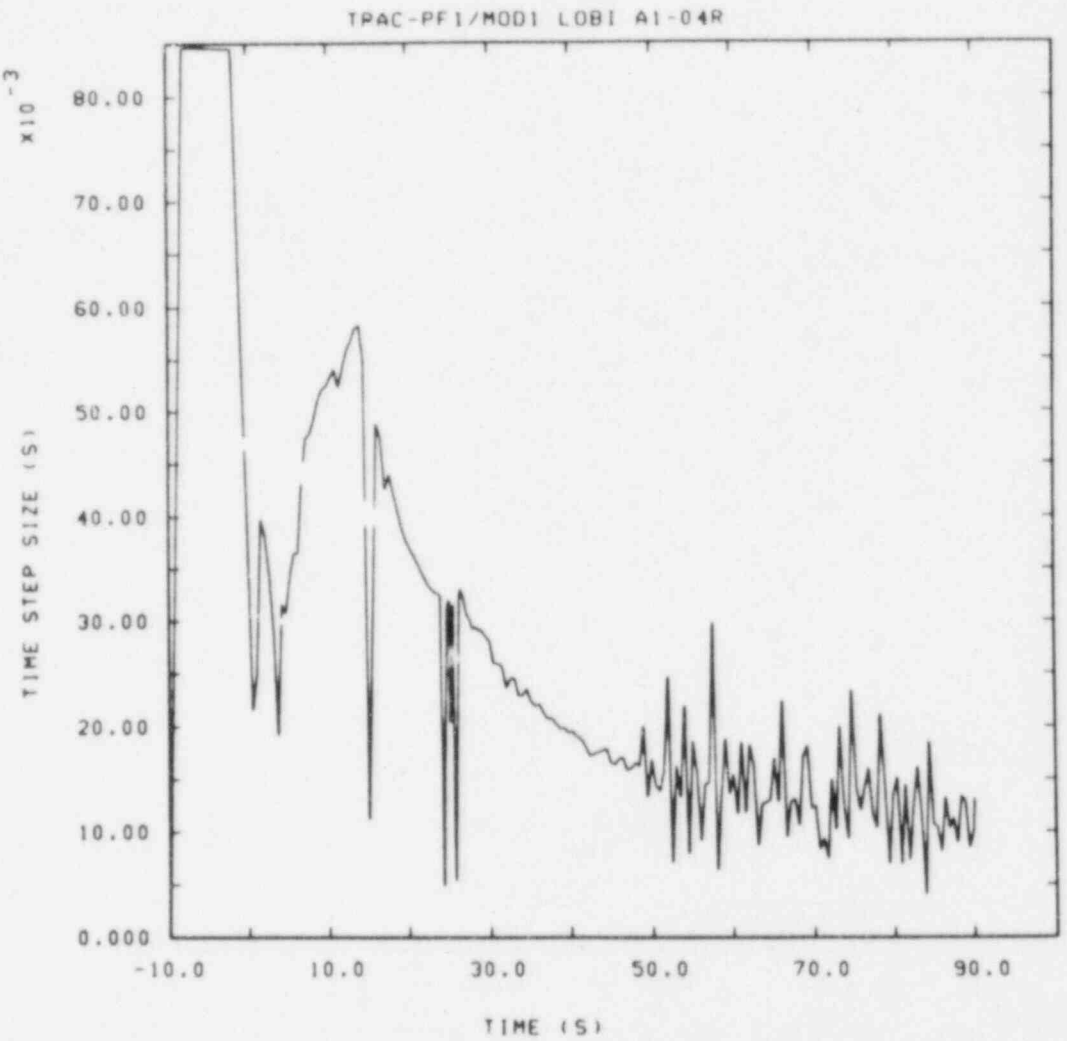

Figure 4.3.2 Time Step History (CYBER-76)

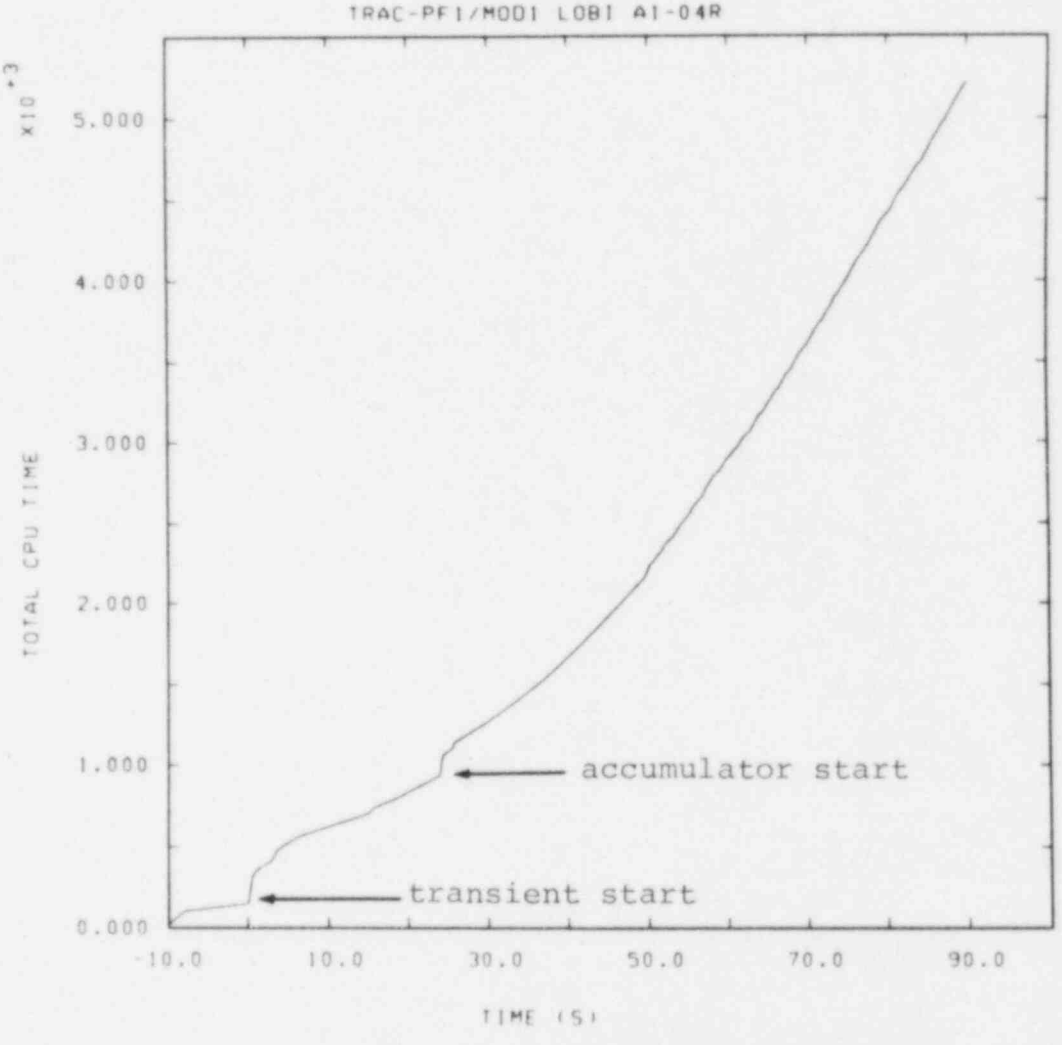

Figure 4.3.3 Total CRAY-1S CPU Time

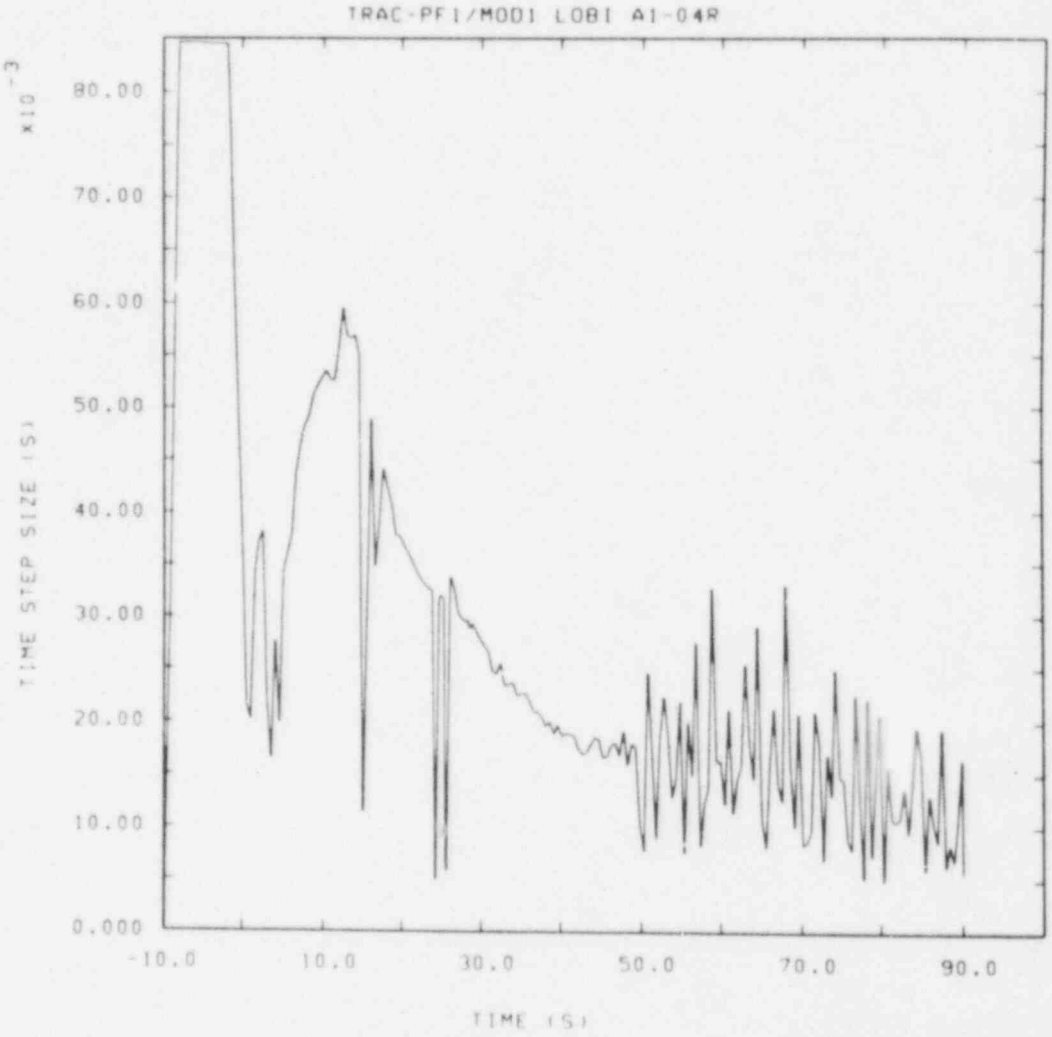

Figure 4.3.4 Time Step History (CRAY-1S)

5.0 SENSITIVITY STUDIES

Several preliminary and/or follow-up calculations were done to investigate the sensitivity of the predicted behavior to various input parameters and/or modelling assumptions. The results of these analyses are briefly discussed in this section.

5.1 Cold Leg Nodalization

One of the discrepancies between our basecase calculated results and the experimental data, mentioned in section 3.3, is in the cold leg densities downstream of the ECC injection port after accumulator injection begins. TRAC predicted the cold leg to be about 40% full of liquid, while the data at that location showed the cold leg to be liquid-full.

A presentation by C. Richards of the UKAEE Winfrith at a recent Code Assessment Review Meeting [13] showed that similar behavior had been seen by other TRAC users, and that the calculated behavior was very sensitive to the number of cells used in the cold leg.

We therefore restarted the A1-04R transient calculation, at the time that accumulator injection began, with more nodes in the intact loop cold leg. The base nodalization had only one cell between the injection node and the downcomer, as shown in Figure 5.1.1a; the subdivided nodalization had five cells between the injection cell and the vessel inlet, as shown in Figure 5.1.1b. The distance between the vessel and the injection point was accidentally changed slightly, with injection 0.841 m from the vessel inlet in the basecase model and 1.041 m from the vessel inlet in the finer-node model. The cell upstream of the injection volume was also subdivided for Δx consistency.

Figure 5.1.2 shows the cold leg densities at and downstream of the accumulator injection port for the restarted calculation, compared to data downstream of the injection. Unlike the results shown in Figure 3.3.2, the downstream density now indicates that a liquid-solid plug is being calculated in part of the cold leg downstream of the accumulator injection point; the density at the vessel inlet is also higher for the finer noded cold leg than in the basecase run. Injection oscillations are calculated in both cases. The density oscillations are exaggerated in the smaller cells of the finer noded cold leg when some void is present, but the flow oscillations are not large enough to disrupt the liquid-solid plug formed. The density at the injection point itself remains low, indicating substantial amounts of vapor remaining, and is very similar in both calculations.

For a different viewpoint, the density profiles in the cold leg 40 seconds into the transient for both the base calculation and the restarted calculation are shown in Figure 5.1.3; the profiles at other times during accumulator injection are very similar. A liquid-solid plug in the more finely noded cold leg extends through three cells, but does not include either the injection cell or the cell adjacent to the vessel. The densities downstream of this liquid plug in the vessel downcomer are also higher than those in the base calculation, although there is still substantial vapor present. (The measured density data indicate that the vessel inlet is only ~70% full of liquid even when the cold leg measurement location itself is liquid-full. [11,12])

This quite different behavior in the intact loop cold leg downstream of the accumulator injection port did not alter significantly any of the other calculated behavior. Thus, while a fine noding is apparently needed to calculate the cold leg density behavior seen, it is not obvious that such a fine noding is needed in order to predict the overall transient response.

5.2 Core Bypass Flow

Two different bypass flow paths exist in the LOBI vessel. A downcomer-to-upper plenum core bypass of approximately 5% is caused by 8 holes of 5.0 mm diameter at the upper end of the core barrel tube; a further estimated bypass between the lower and upper plena of about 2% occurs via the gap between the ceramic fillers and the core barrel tube. [12] The magnitude assumed for these bypass flows was found to have a significant effect on the calculated results, particularly in the early-time core rewet.

These two bypass flows were combined into a single flow path in our vessel nodalization, as a larger (to avoid small Courant time step limits) flow area from the second core ring to the downcomer ring in the topmost axial level of the 3-D VESSEL component. The radial flow loss coefficient was adjusted to give the desired total steady state bypass flow.

In several of our preliminary calculations, this bypass flow was accidentally zeroed out due to a user input error. The results showed no core rewet calculated during the ~5-15 second period, because of a reduced (compared to data) reestablished positive core flow. In later calculations, the core bypass was varied from 5% to 7% by changing the appropriate radial loss coefficients. (The basecase analysis discussed in Section 3 used an intermediate core bypass value of ~6%.)

The core inlet liquid and vapor mass flow rates for calculations with no core bypass, with 5% core bypass and with 7% core bypass are compared in Figure 5.2.1. The early-time negative liquid outflow is virtually identical in these three runs, but the subsequent positive core flow is significantly larger when the core bypass flow is modelled. This reestablished positive core flow is greater for 7% bypass than for 5% bypass, although this is hard to see from the plots in Figure 5.2.1.

The effect of the increase in positive core flow with increasing core bypass flow is better seen in Figure 5.2.2, which compares the core liquid masses for the same three calculations. The influx of liquid to the core due to reestablishment of positive flow shows up as a temporary increase in the core liquid mass in each case; this increase is greater with 7% core bypass than with 5% bypass.

The different liquid flows through the core in these three calculations result in different rod heat transfer rates. Figure 5.2.3 compares the (input) core power and the total rod heat transfer rates with no core bypass, with 5% core bypass and with 7% core bypass. While the core power remains the same in all three calculations, the rods transfer out progressively more heat as the core bypass flow is increased. The difference is particularly visible during the first 15 s of the transient.

The effect of core bypass flow on the rod temperatures is shown in Figure 5.2.4, which compares rod temperatures at the core mid-plane for these three calculations. The clad temperatures are progressively lower for increasing core bypass flow. There is some difference visible in the blowdown PCT, and a much greater difference in the reflood PCT. Although none of these runs showed a core rewet at this elevation during ~5-15 s, the clad temperatures with the higher core bypass rates are in much better agreement with the experimental data overall.

5.3 Discharge Coefficients

Our preliminary TRAC calculations done for the A1-04R transient used subcooled and saturated discharge coefficients of 1.0 and 0.85, respectively; these were the values which gave the best results in the previous RELAP5/MOD1 analyses of this and other LOBI large break tests. All the final TRAC calculations done also used a subcooled discharge coefficient of 1.0, because this gave good agreement on the peak break flows; no sensitivity studies on the effects of the subcooled discharge coefficient were done. However, we found that a saturated discharge coefficient also equal to 1.0 gave better agreement with experimental data on the time of accumulator injection start. (The RELAP5/MOD1 and TRAC-PF1/MOD1 break flow models are similar, although not identical.)

Figures 5.3.1 and 5.3.2 compare the vessel-side and pump-side upstream break flows, respectively, using saturated discharge coefficients of 0.9 and 1.0 in otherwise identical calculations. (The "truncated" peak vessel-side break flow data has already been discussed in Section 3.2.) The effect of changing the saturated discharge coefficient is hardly visible in the break flows being calculated, although some minor differences can be distinguished in the vessel-side flow; however, the overall effect is visible when more global system variables are studied.

The intact and broken loop cold leg pressures for these two calculations are shown in Figure 5.3.3. The lower saturated discharge coefficient of 0.9 results in higher pressures in both loops throughout most of the latter part of the transient. The lower intact loop pressures obtained using a saturated discharge coefficient of 1.0 are in better agreement with experimental data and thus also give better agreement on the initiation time for accumulator injection (23.8 s vs the measured 24 s; the run with the 0.9 discharge coefficient had accumulator injection beginning at 25.5 s).

The discharge coefficient used also affects the inventory remaining in the system at any given time, as would be expected. Figure 5.3.4 compares the vessel liquid masses calculated using saturated discharge coefficients of 0.9 and 1.0. After subcooled blowdown ends and saturated break flow controls the transient, the vessel shows a progressively lower inventory for the greater discharge coefficient and resulting higher break flow. (The flattening out of the vessel liquid inventory after about 26 s in the calculation with the saturated discharge coefficient of 1.0 is a result of accumulator injection; the calculation with the later accumulator injection should show a similar flattening at about 30 s.)

The retention of more liquid in the vessel when using lower saturated discharge coefficients in turn causes lower clad temperatures, as shown in Figure 5.3.5, which shows the core mid-plane rod temperatures for these two calculations. There are no differences in the behavior until the partial rewet starting at ~5 s, when slightly lower temperatures are calculated using a saturated discharge coefficient of 0.90; later in the transient, substantially lower clad temperatures are predicted, using this lower saturated discharge coefficient.

5.4 Accumulator Surge Line Resistance

The TRAC nodalization for A1-04R was originally set up with a total user-input accumulator surge line resistance of 4.895,

the value which gave excellent agreement with data in our earlier RELAP5/MOD1 analyses of this test [3]; this user-input resistance was divided equally among the 11 junctions used in the surge line modelling in our TRAC input.

Figure 5.4.1 shows the accumulator injection rate calculated using this resistance. The resulting flow rate is generally about a third higher than the experimental data (where the RELAP5/MOD1 results using this line resistance were within ~1-5% of the experimental data throughout the transient, with the peak flow within 1%). With hindsight, some part of this discrepancy is likely due to the "hardwired" assumption of a constant high Fanning friction factor f of 0.03 in the accumulator surge line model in RELAP5/MOD1 [14], which is not explicitly used in TRAC.

The user-input accumulator surge line resistance was then progressively increased in several runs, with the results shown in Figure 5.4.2, which compares the accumulator injection rates from two calculations using user-input surge line resistances of 13.75 and 24.75 (with the latter being that used in the base calculation discussed in Section 3). As expected, the injection decreases as the resistance is increased.

The different injection rates in these various calculations do not result in any visibly different behavior in density and temperature at and downstream of the accumulator injection point. The late-time vessel inventories differ slightly, as do the late-time rod temperatures. Figure 5.4.3 compares the mid-core rod temperatures calculated using total surge line resistances of 13.75 and 24.75. The rod temperatures at vessel heights of 2.8006 and 4.2574 m are very similar for these two runs but the rod temperature at the core mid-plane (3.529 m) is decreasing more quickly for the calculation with the higher accumulator injection flow rate (i.e., with the lower accumulator surge line resistance).

The final line resistance of 24.75 thus obtained ad hoc is also derivable from the facility data in the test documentation [9]. Based on measured total Δp from the accumulator to the intact loop cold leg, a total resistance of 37 is cited. Assuming the high wall friction generally typical of accumulator injection (in fact, f=0.03) and using a surge line length of 10.25 m and diameter of 0.025 m, the wall friction fL/d gives a resistance of 12.3, leaving 24.7 to be user-input to represent bends, valves, orifices, turbometers, loop-entrance effects, etc.

If the TRAC results for accumulator injection flow rate vs accumulator surge line loss coefficient are correct in this case, then the RELAP5/MOD1 results must be in error; considering the many known and acknowledged problems in calculating accumulator injection with RELAP5, this is quite possible.

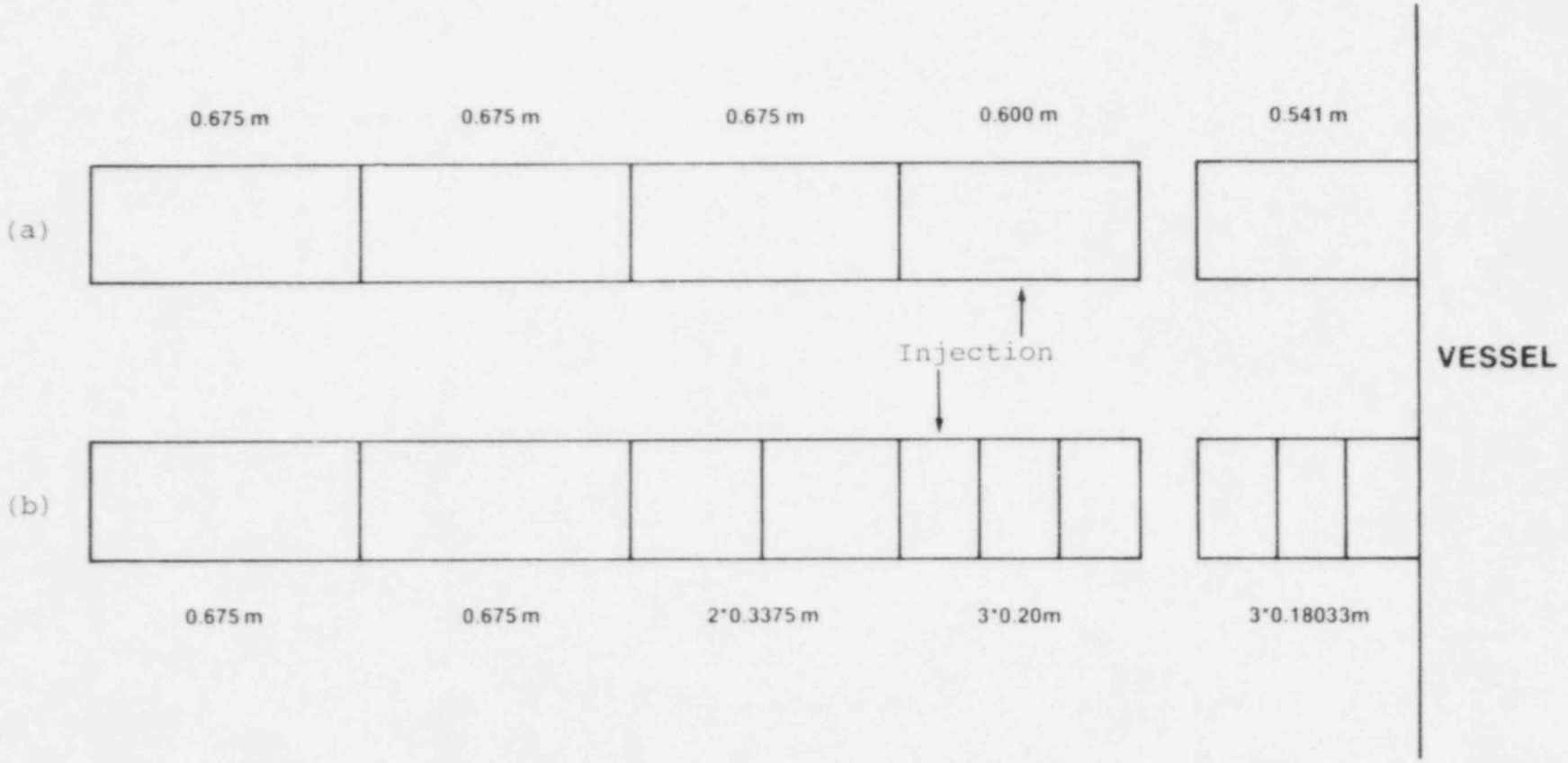

Figure 5.1.1 (a) Base and (b) Fine Noding of Intact Loop Cold Leg

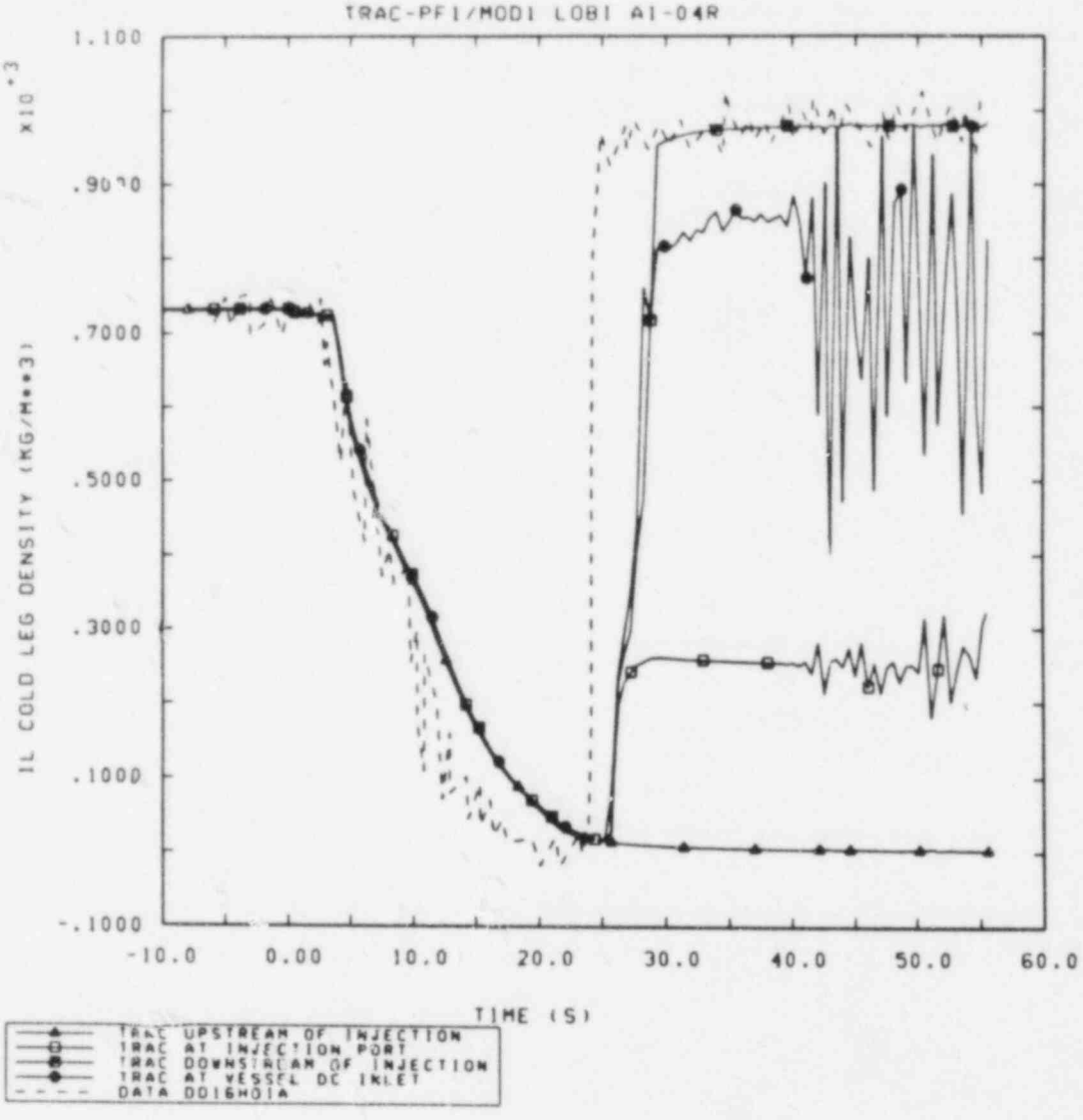

Figure 5.1.2 Fluid Densities at and Downstream of Accumulator Injection Point using Fine Node Cold Leg Model

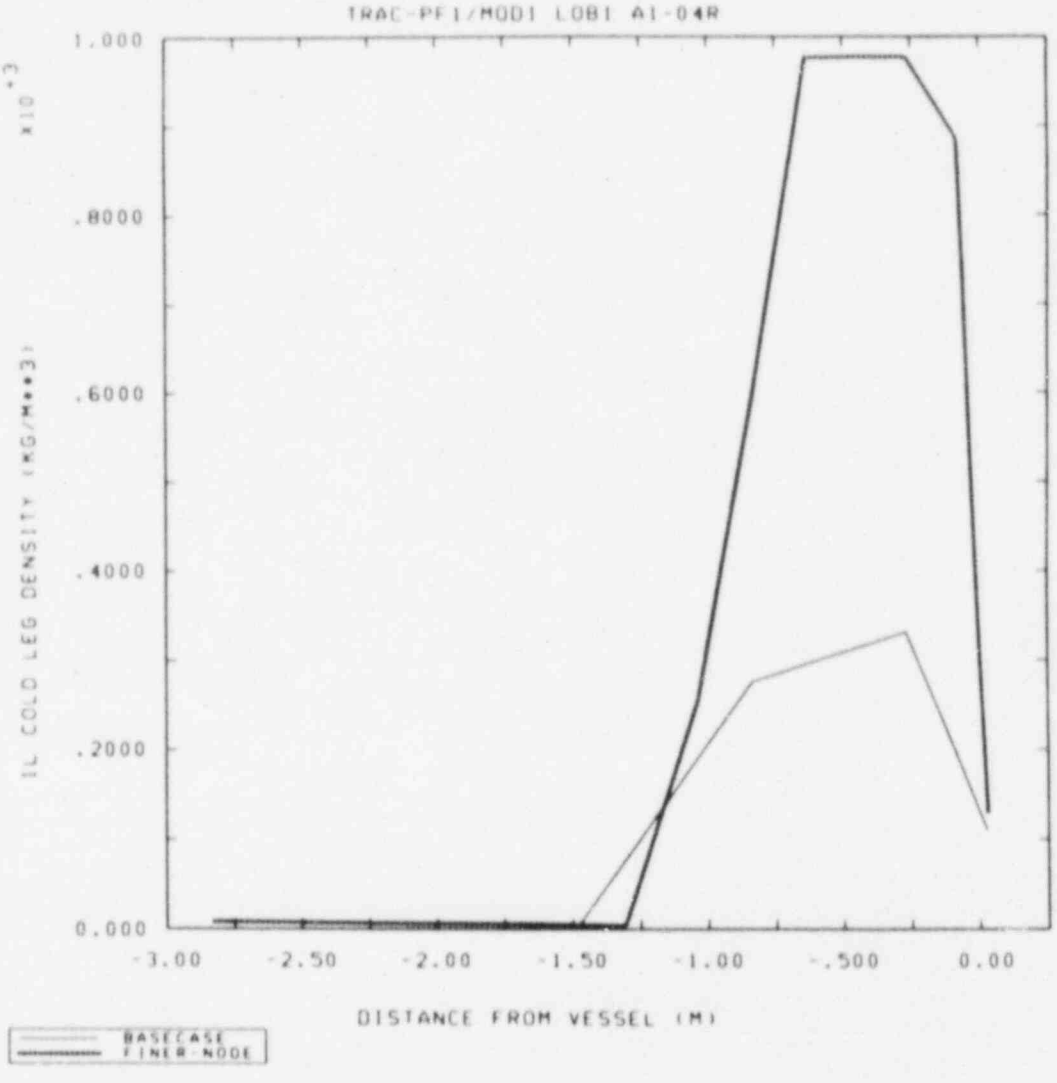

Figure 5.1.3 Fluid Densities along Intact Loop Cold Leg at 40 s using Base and Fine Node Cold Leg Models

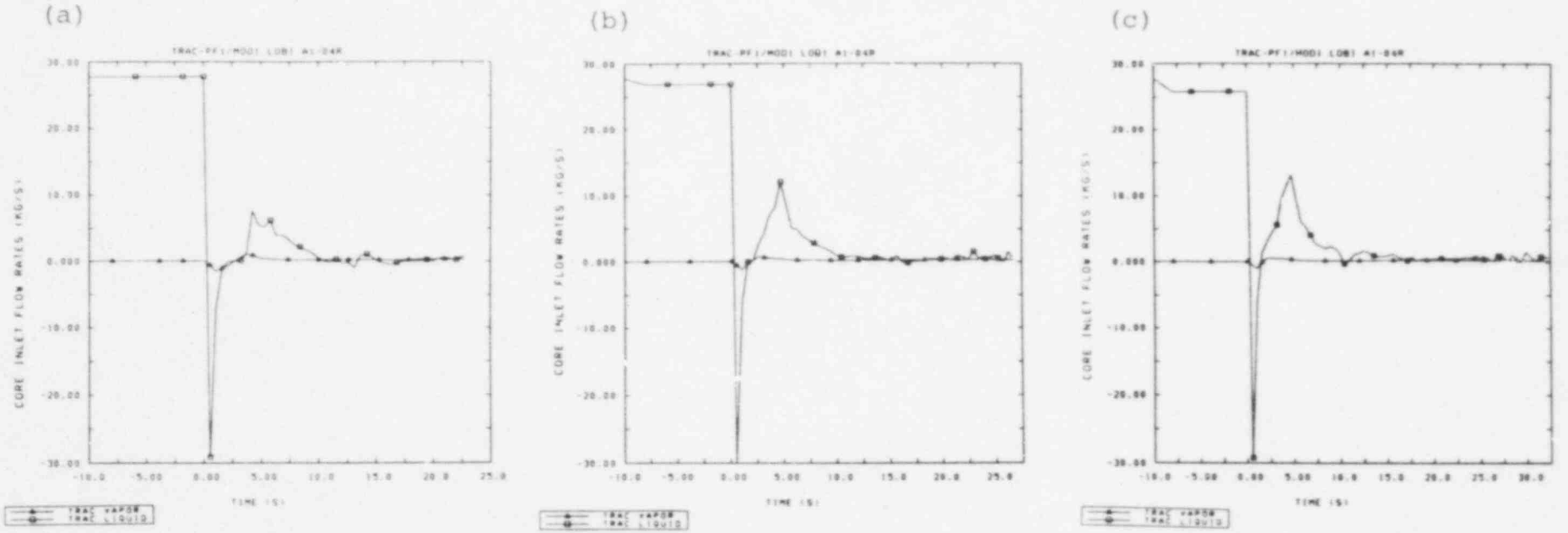

Figure 5.2.1 Core Inlet Liquid and Vapor Mass Flow Rates with (a) No Core Bypass, (b) 5% Core Bypass and (c) 7% Core Bypass

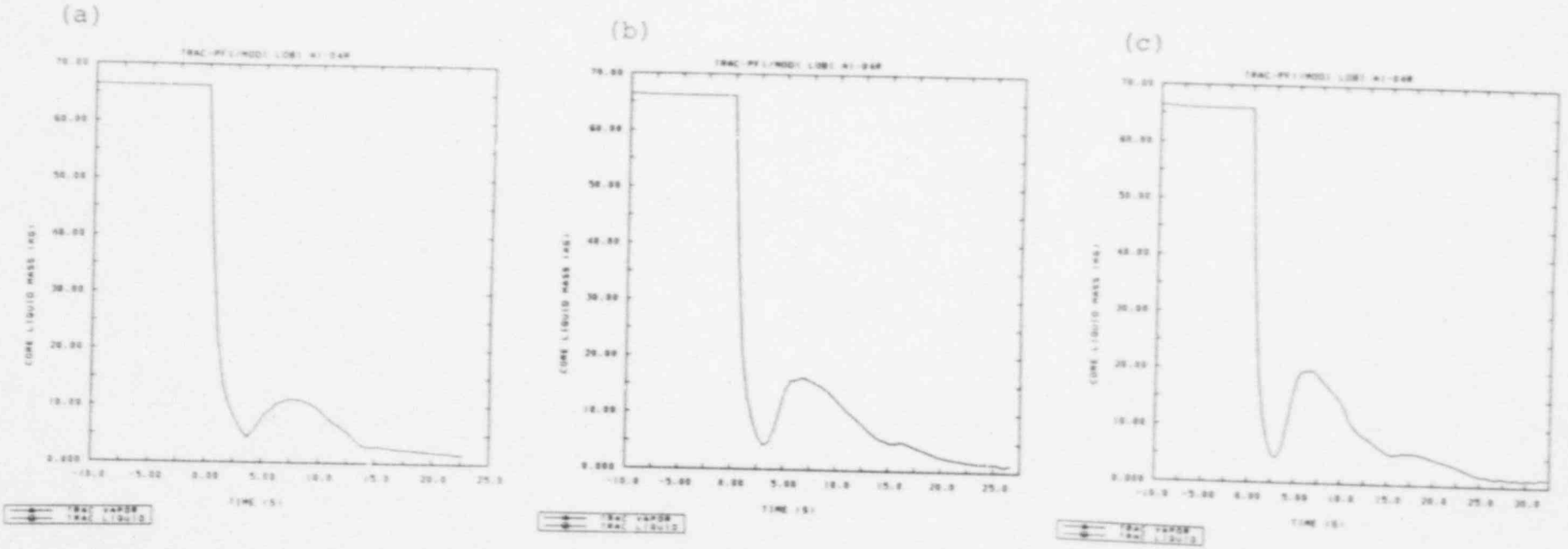

Figure 5.2.2 Core Liquid Mass with (a) No Core Bypass, (b) 5% Core Bypass and (c) 7% Core Bypass

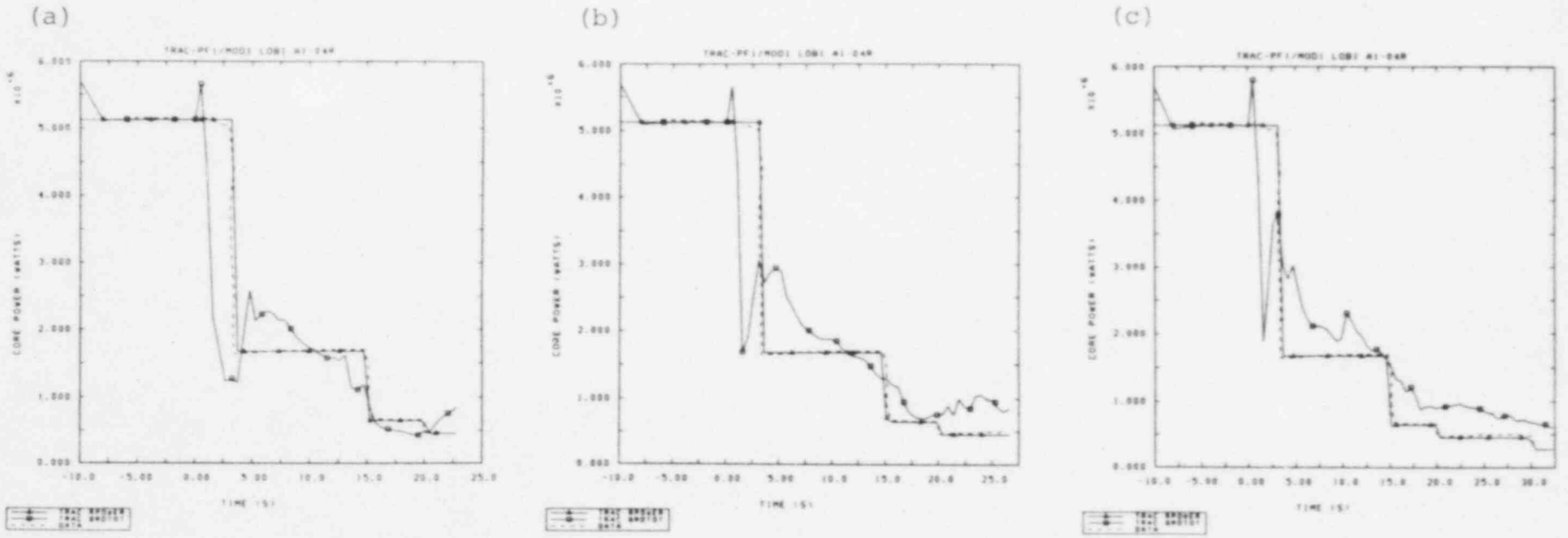

Figure 5.2.3 Core Power and Total Rod Heat Transfer Rate with (a) No Core Bypass, (b) 5% Core Bypass and (c) 7% Core Bypass

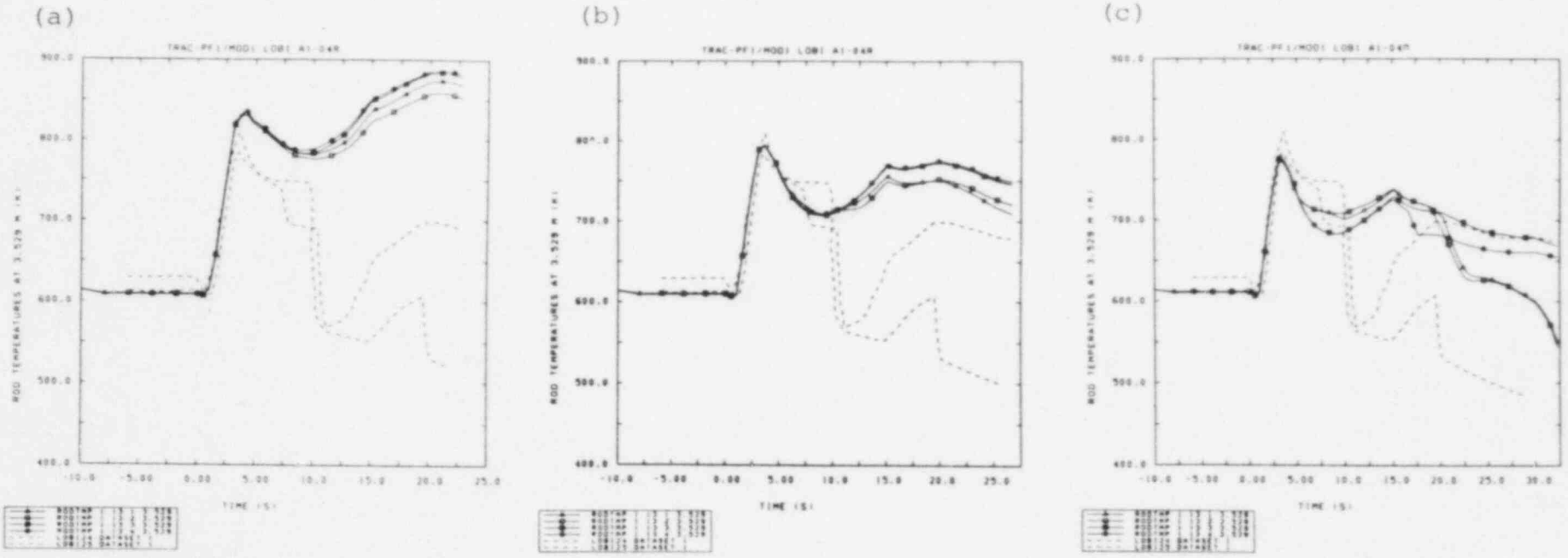

Figure 5.2.4 Core Mid-Plane Rod Temperatures with (a) No Core Bypass, (b) 5% Core Bypass and (c) 7% Core Bypass

(a)

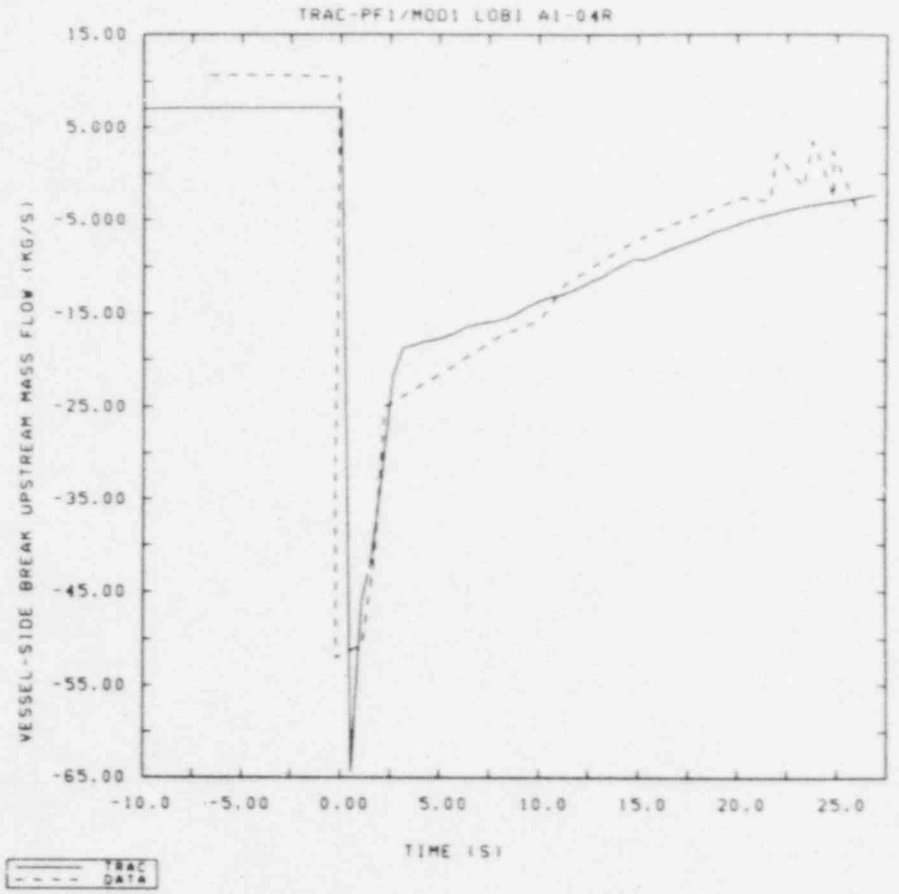

(b)

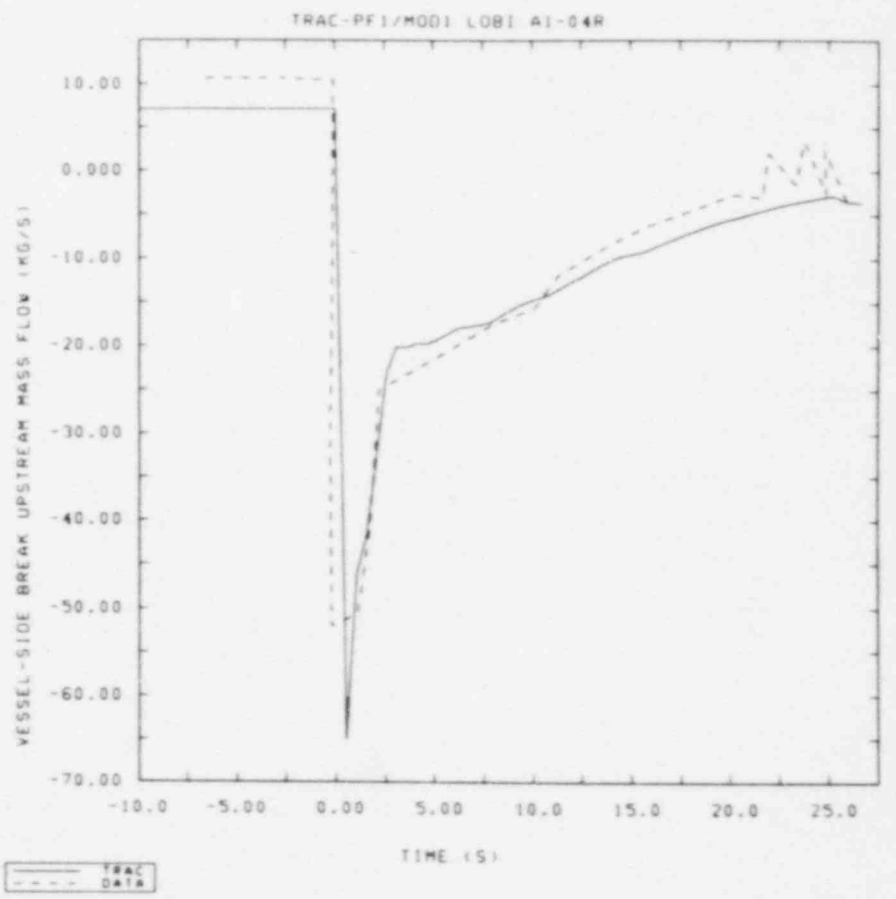

Figure 5.3.1 Vessel-Side Break Flow Rates using Saturated Discharge Coefficients of (a) 0.9 and (b) 1.0

(a)

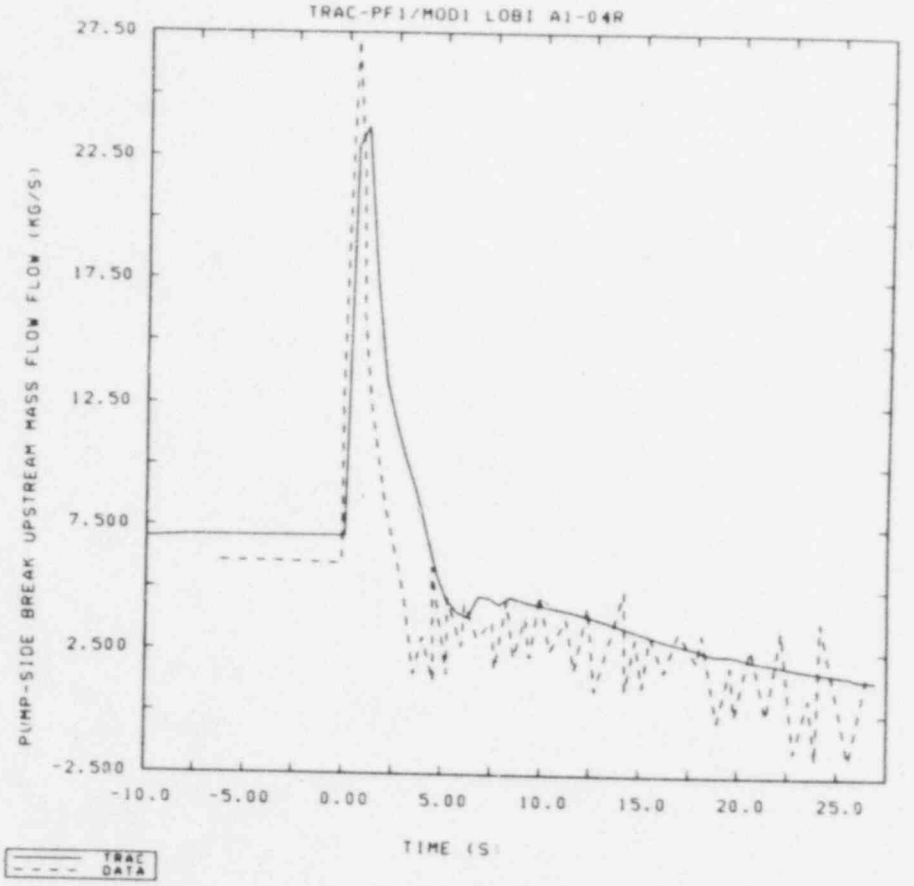

(b)

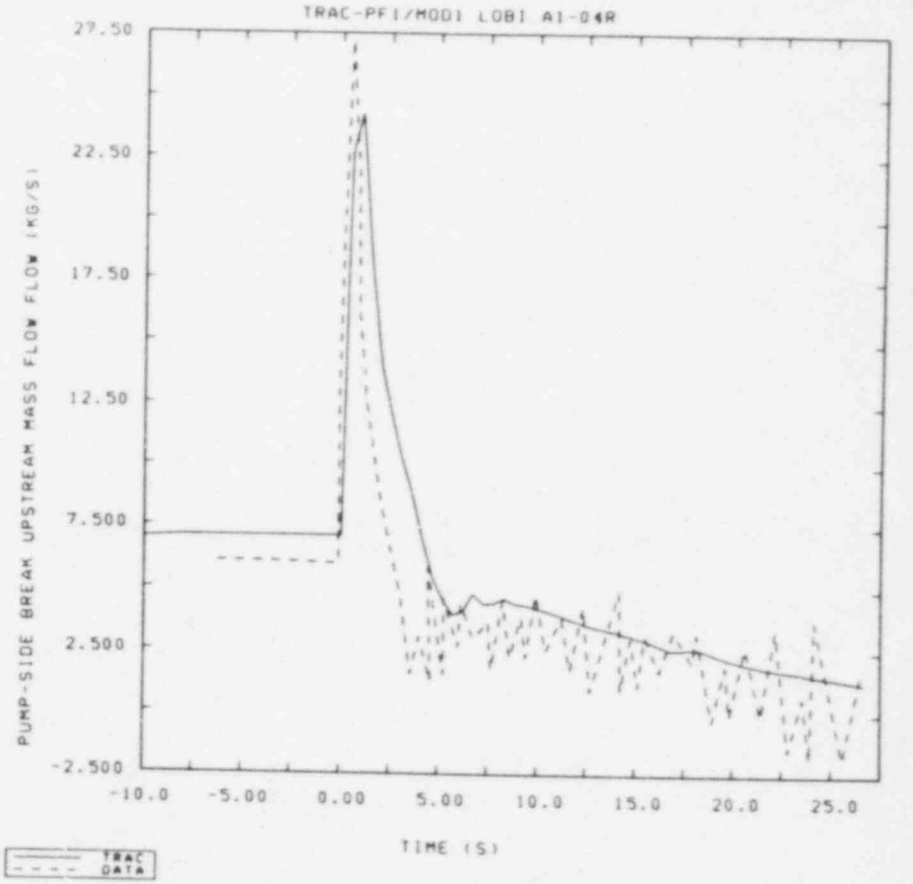

Figure 5.3.2 Pump-Side Break Flow Rates using Saturated Discharge Coefficients of (a) 0.9 and (b) 1.0

(a)

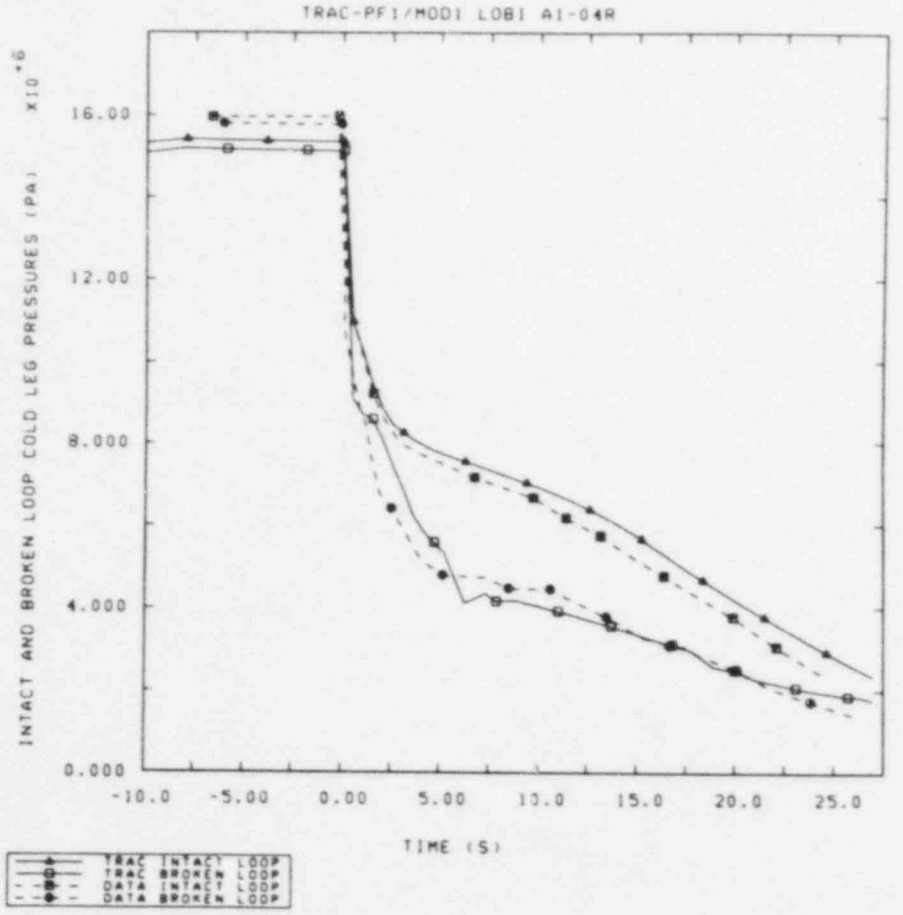

(b)

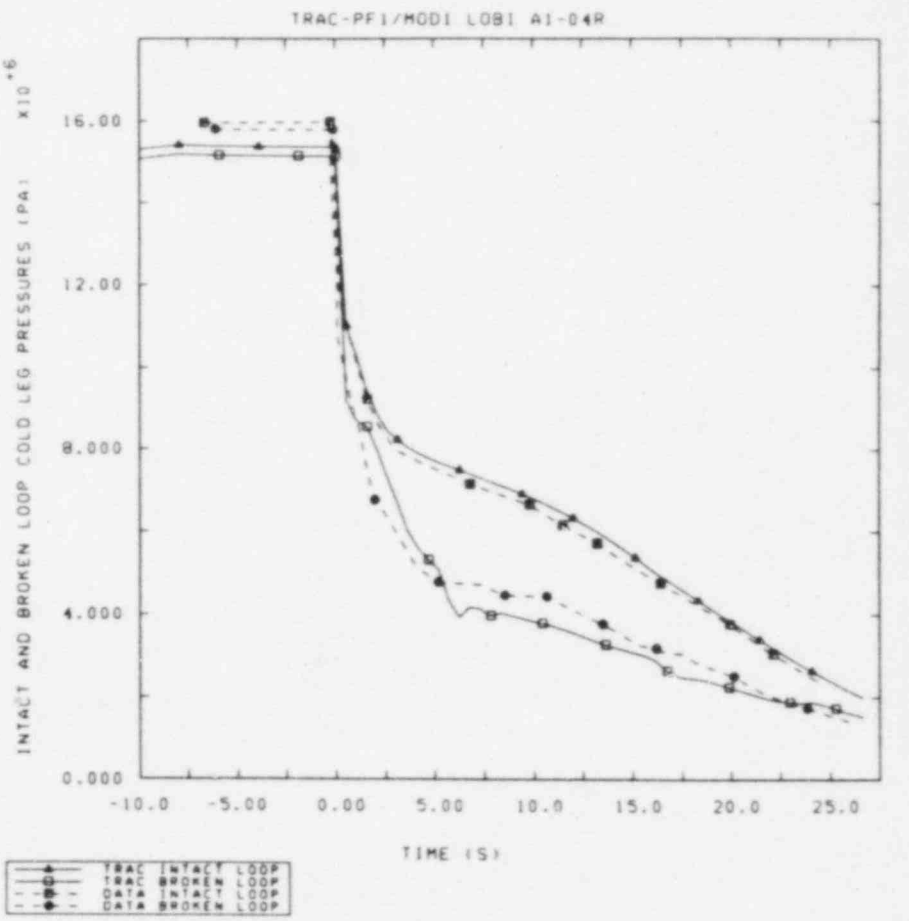

Figure 5.3.3 Intact and Broken Loop Cold Leg Pressures using Saturated Discharge Coefficients of (a) 0.9 and (b) 1.0

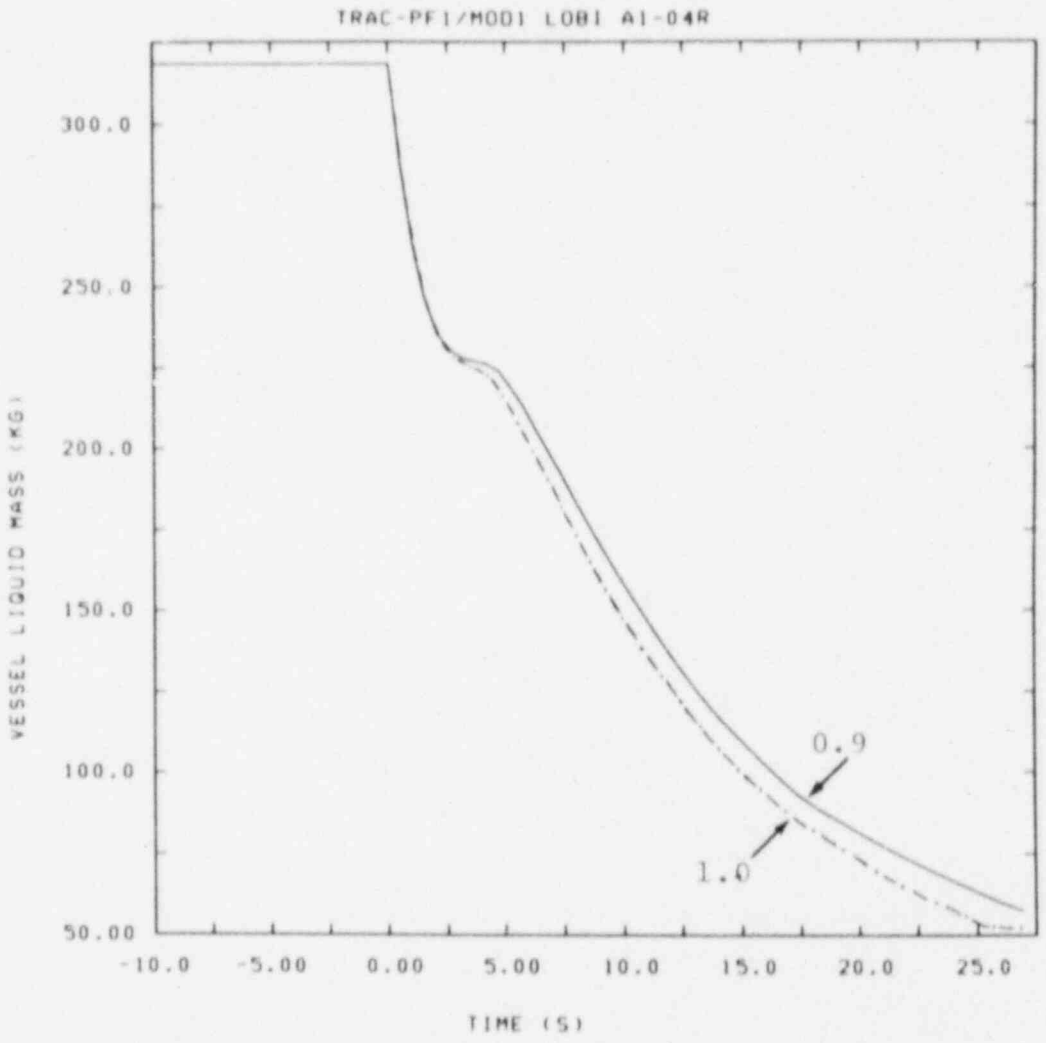

Figure 5.3.4 Vessel Liquid Mass using Saturated Discharge Coefficients of 0.9 and 1.0

(a)

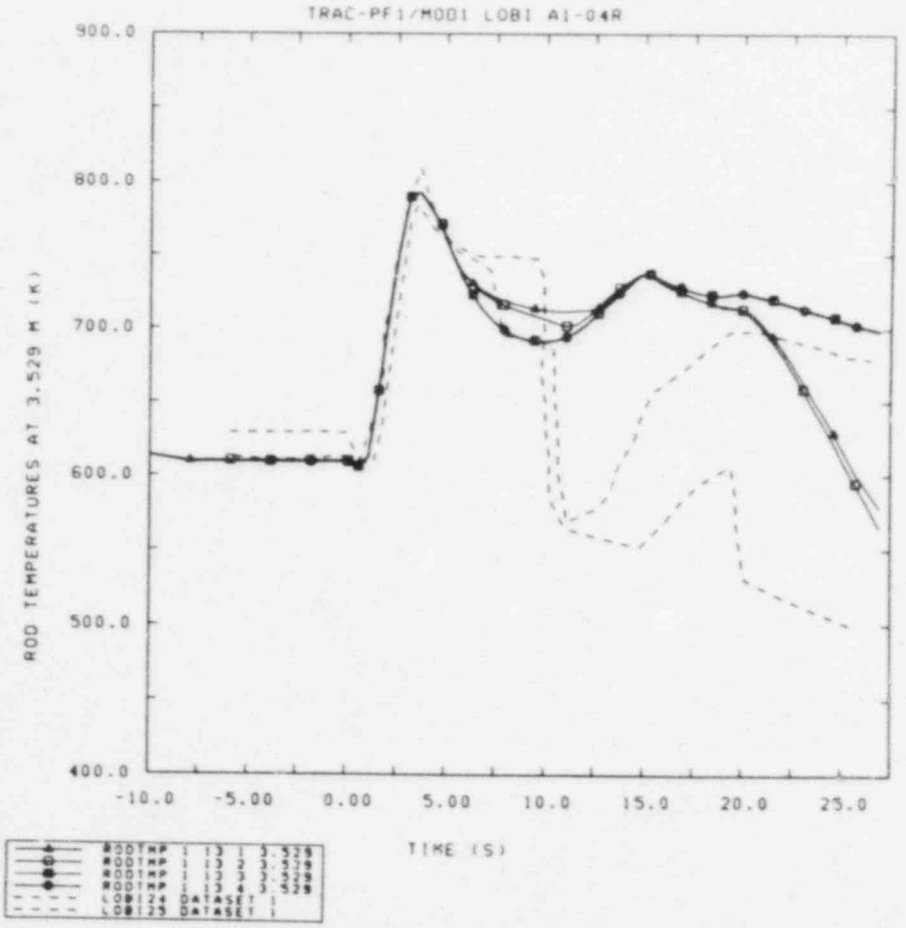

(b)

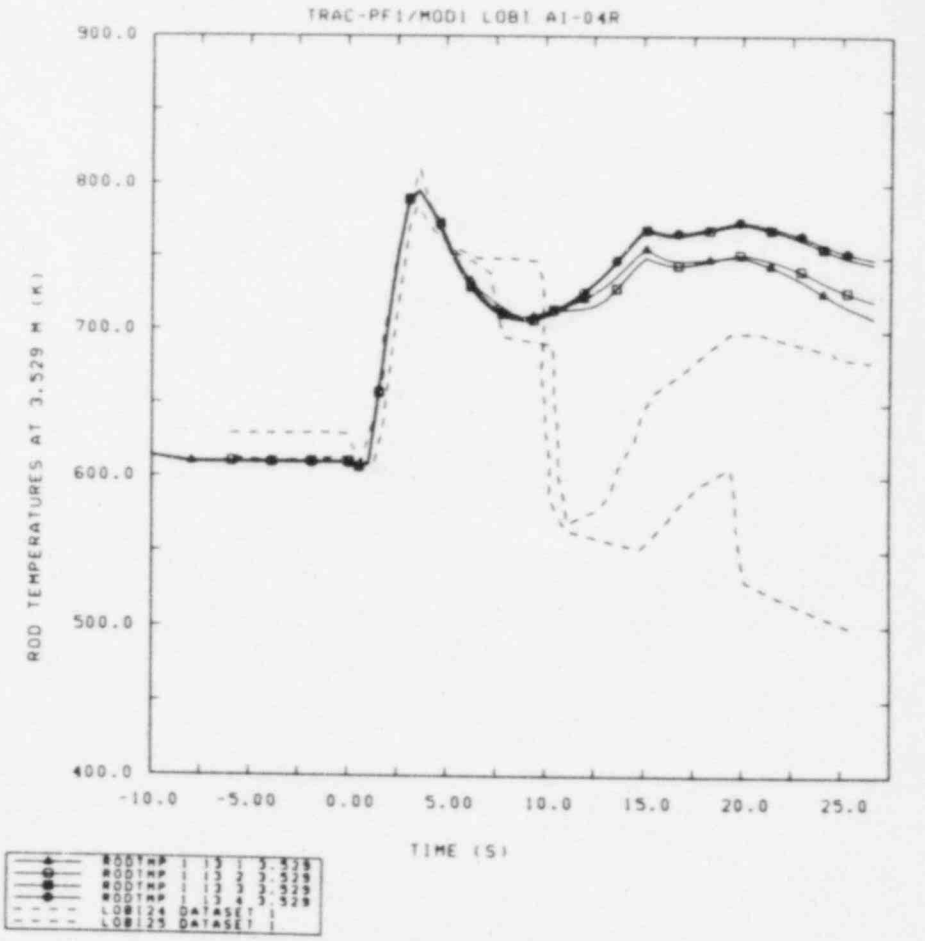

Figure 5.3.5 Core Mid-Plane Rod Temperatures using Saturated Discharge Coefficients of (a) 0.9 and (b) 1.0

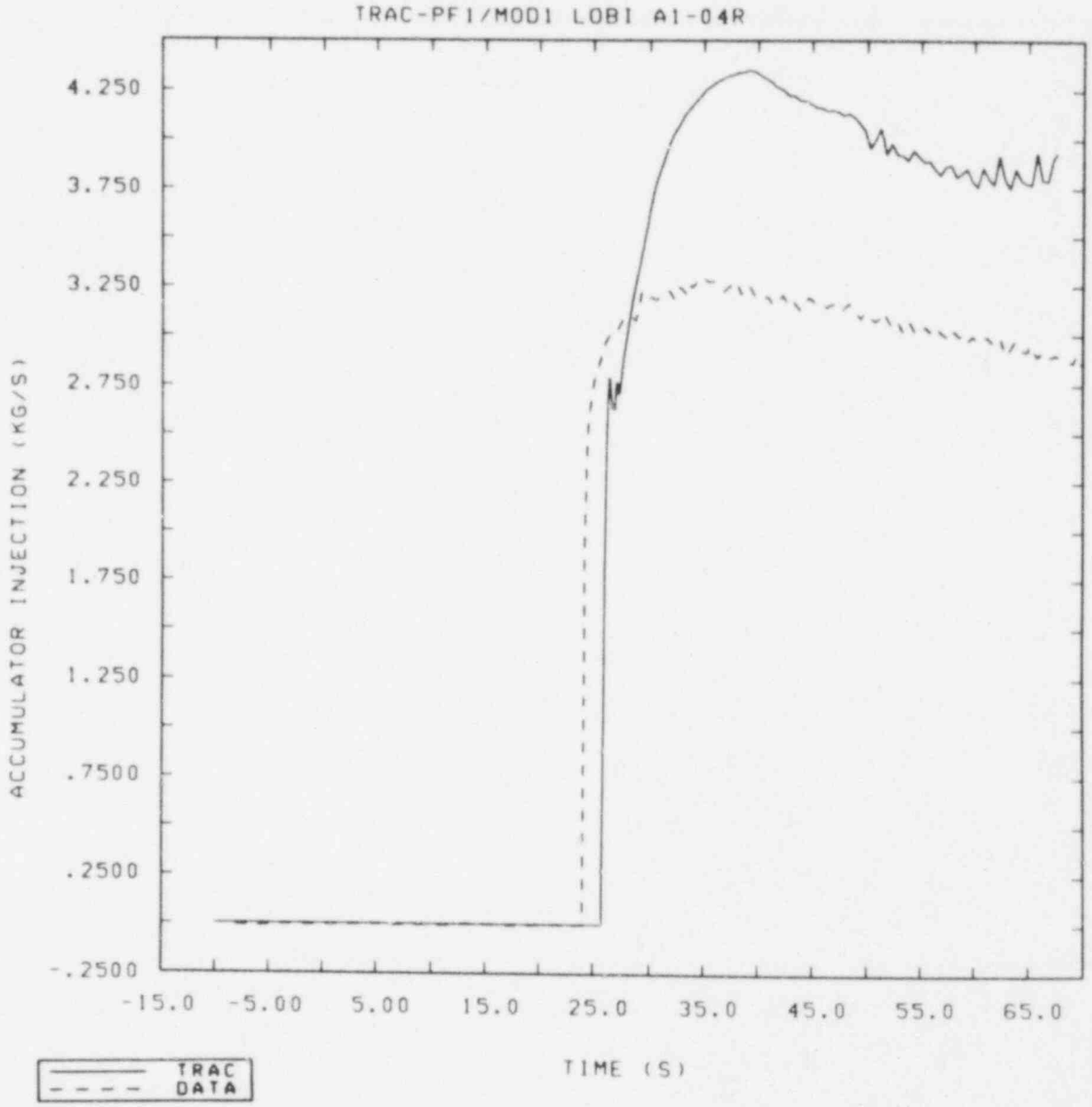

Figure 5.4.1 Accumulator Injection Rate using Total Surge Line Resistance of 4.895

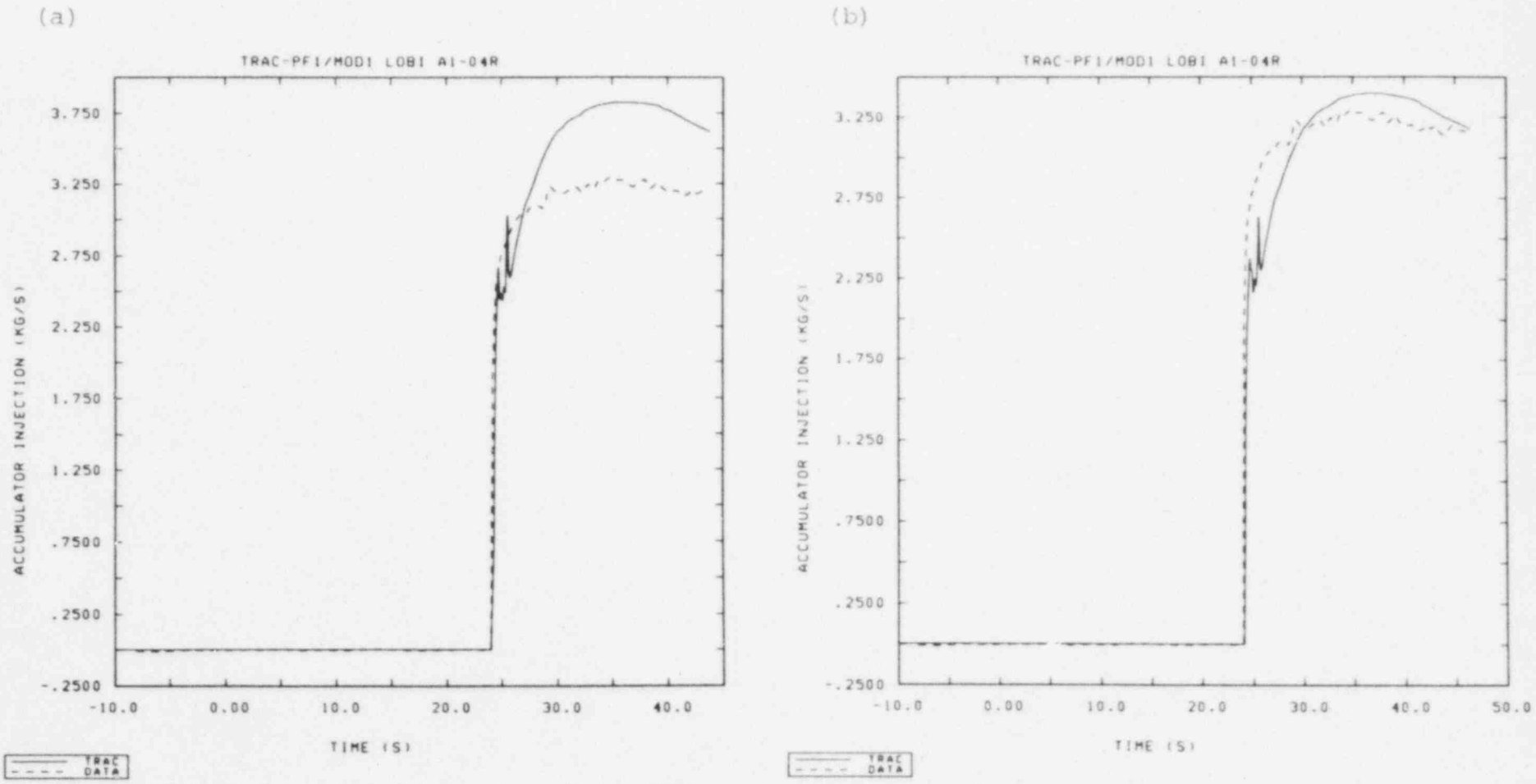

Figure 5.4.2 Accumulator Injection Rates using Total Surge Line Resistances of (a) 13.75 and (b) 24.75

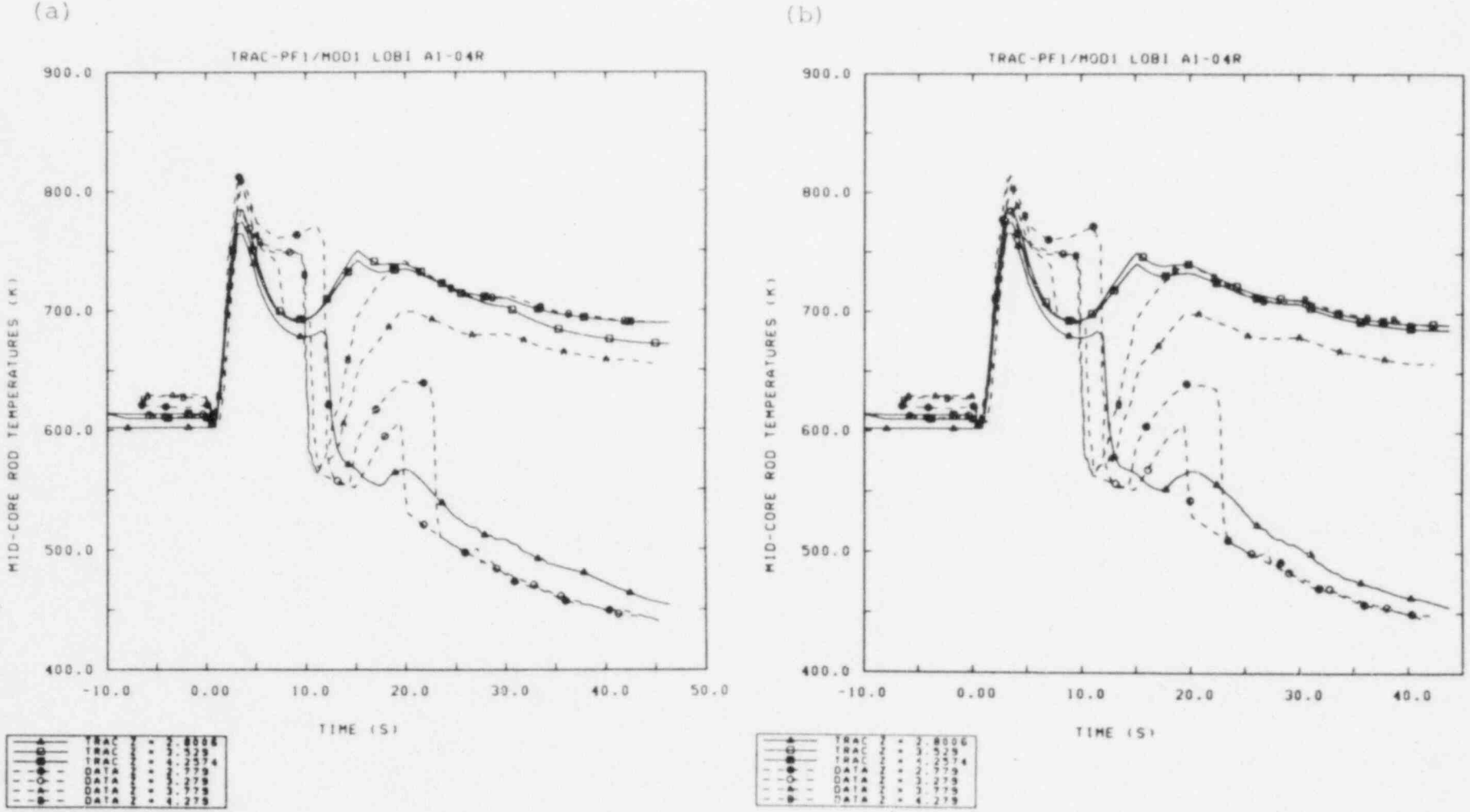

Figure 5.4.3 Mid-Core Rod Temperatures using Total Surge Line Resistances of (a) 13.75 and (b) 24.75

6.0 USER EXPERIENCE AND CODE ERRORS

In this section, we present the history of this LOBI A1-04R transient analysis, describing the numerous iterations due to user and/or code errors and/or updates leading to the final "basecase" analysis discussed in Sections 3 and 4. The various code errors discovered and documented in this section have been reported to the code developers, and either have been or will be corrected in later code versions.

6.1 Calculation History

After completing a preliminary steady state initialization using Version 11.1 of TRAC-PF1/MOD1, we ran a transient calculation for almost 70 seconds. The calculated pressures and break flows were in reasonably good agreement with data, using the same values for the discharge coefficients as in our earlier RELAP5/MOD1 analyses (i.e., 1.0 for subcooled flow and 0.85 for saturated flow). The calculated peak clad temperature, however, was significantly higher (by ~40 K) than the measured value; the core rewet at 5-15 seconds was not calculated (except at the very top of the core); and the code results showed no signs of a quench front moving up the core at late times, although the data shows the middle core quenching from 25 to 55 seconds.

After studying these results, we found and corrected some errors in our LOBI input model. The major impact on the A1-04R results came from correcting the power shape input to a power density shape input, which resulted in a calculated PCT in excellent agreement with data, within 1 K of the measured value. With the early-time core response now in better agreement with data, we next searched for possible causes of not calculating the total core rewet at 5-15 seconds; missing this rewet could be largely responsible for the lack of a calculated core quench later in the transient, since without this rewet the rods in the calculation are significantly hotter late in the transient compared to data.

At the time, a possible cause of not calculating the observed total core rewet at 5-15 seconds appeared to be the prediction of substantial liquid superheat in many of the core cells during the relevant period. This was found to be due to a code error, discussed in more detail in Section 6.2; with this error corrected, no spurious liquid superheat was calculated. However, the other calculated results were generally unchanged.

Because a number of other code errors in Version 11.1 had been found and fixed by the time the liquid superheat error had been corrected, we reran the calculation with Version 11.6, up to the time accumulator injection begins. Despite the numerous code changes, the overall results with 11.6 were very little different from those calculated with Version 11.1.

The first ~20 seconds were then rerun with a modified version of TRAC-PF1/MOD1 Version 11.6 which had the vessel interface sharpener disabled, because we thought that this special model might be retaining water in the lower plenum and lower core and thus damping the liquid slug passing through the core at ~5-15 s; the results, however, showed no significant differences compared to the behavior previously calculated with the code as released.

The first ~15 seconds, until accumulator flow initiation, were later rerun with Versions 11.9 and 12.0 of the code in hopes that some peculiar "bug" we could not find was causing the poor prediction; again, no significant changes in results were seen.

Because of some comments made at the Code Assessment Review Meeting in December 1984 [13], we rechecked the input yet again and found that the core bypass flow had accidentally been zeroed out in all these preliminary runs due to an input error. With this corrected, a larger slug of liquid was calculated to go through the core and the resulting clad temperatures were in much better agreement with data throughout the latter portion of the transient, although the PCT calculated was now lower than that measured (by ~40 K) and a total rewet at ~5-15 s was still not being calculated in most of the core (as already discussed in Section 5.2). A few runs were then done with different core bypass flow rates and accumulator surge line resistances to study the sensitivity of the results to these parameters.

Also based on comments during a presentation at the December 1984 Code Assessment Review Meeting, the final basecase calculation was restarted at the time of accumulator injection with a more finely noded intact loop cold leg to see if nodalization would affect the calculated plugging of the cold leg downstream of the ECC injection point (which it did, as discussed above in Section 5.1).

After the A1-04R transient calculation and analysis were considered complete, we found a code error in Version 12.0 which prevented the steam generator feedwater from shutting off as specified (described in Section 6.3). Although we would not expect differences in secondary side feedwater to visibly affect the major behavior in a 200% large break transient, we decided to rerun the transient with the corrected feedwater flow in the interest of completeness. In order to maximize the benefit of this rerun, we then decided to do the corrected calculation on the CRAY-1S in order to compare run times for almost identical calculations. (All previous A1-04R calculations had been done on a CYBER-76.) Some differences in transient results, particularly in the rod quench at the core mid-plane, were seen; also, the CRAY calculation did not run as much faster than the CYBER equivalent as expected, as discussed in Section 4.3.

Although we felt that this unexpected behavior could not possibly be due to the only known difference between the two calculations (i.e., the FILL flow coding fix), the A1-04R transient was rerun one last time on the CYBER with the same corrected code. Thus, the same input deck was being run with the same code version and the same code correction updates on both the CYBER and CRAY computers. The differences in transient results were still observed. These results have been reported to the code developers at LANL.

6.2 "Liquid Superheat" Code Error

As mentioned above, one possible cause of not calculating the observed total core rewet at 5-15 seconds with Version 11.1 appeared to be the prediction of substantial (~10 K) and sustained (~10 s) liquid superheat in much of the liquid slug entering the core from the lower plenum during the relevant period. This liquid superheat was seen in the three levels below the core mid-plane (i.e., vessel levels 4, 5 and 6).

Figure 6.2.1 shows the void fractions in each of the inner four core cells in level 5 from one of our preliminary runs. The low void fraction during the ~5-15 second time period in the inner two cells indicates a substantial amount of liquid is present. During the same time period, the liquid temperature in these cells remains nearly constant, as shown in Figure 6.2.2. As the system continues to blow down and the saturation temperature continues to drop (also shown in Figure 6.2.2), the liquid in these cells becomes progressively more superheated, until it eventually flashes into vapor.

Although some liquid superheat before flashing is possible, we would expect only fractions of a degree superheating for a much shorter time. The liquid retained an obviously unphysical degree of superheat in this calculation because the liquid-to interface heat transfer term ALV was identically zero during this period, as indicated in Figure 6.2.3. Thus, although the vapor-to-interface term CHTI was nonzero (Figure 6.2.4), the excess heat could not leave the liquid and was retained until the conditions changed sufficiently to activate a different flow regime of the interfacial heat transfer logic.

After a number of discussions with the code developers at LANL (in particular, John Mahaffy), a coding error in the 3-D constitutive package was identified; with this error corrected in the Version 11.6 correction updates, no spurious liquid superheat is calculated. However, as mentioned earlier, the other calculated results were generally unchanged.

6.3 "FILL Table" Code Error

After a number of transient calculations had been run, a code error was discovered (actually, first by studying the calculated results for LOBI intermediate break test B-R1M, also being analyzed for this assessment program) which resulted in the feedwater being only partially shut off after transient start. This code error involved the "flow vs time-since-trip" logic in a FILL component in Version 12.0 of PF1/MOD1 and in previous code versions.

Most of our input decks use a linear rate factor table multiplying the FILL trip set-status (set to 1 when the trip is on) to calculate "time since trip" as the independent variable for tabular lookups, as documented in the input manual. The code error in the FILL logic caused that multiplication to be omitted, so that the tabular lookup always returned the dependent variable corresponding to an independent variable value of 1. The resulting flow rate would thus be equal to the flow rate specified at 1 second after trip, generally not yet zero because more typical ramp times for steam generator feedwater shutoff would be 5 to 25 seconds.

Because this coding error was located within the FILL logic, the same input formulation worked correctly in other components (i.e., for PUMP speed ramps, VESSEL core power tables, VALVE motions and BREAK pressure boundary conditions). Thus, the only change this made in the A1-04R calculation was in shutting off the secondary side feedwater to both steam generators. The error caused substantial feedwater injection (at about half the steady state value) throughout the transient, resulting in higher liquid inventories and more liquid subcooling on the secondary sides. This was not expected to significantly affect the primary side transient response in a large-break LOCA; in fact, correction of the error produced no visible differences in the primary side behavior at or near the steam generators. (The secondary side response did change, as expected.)

This error was reported to the code developers at LANL together with the fix we had developed, and has since been corrected in later code versions.

6.4 "CRAY Plot" Code Error

While most of the calculated response (e.g., primary system pressures, accumulator injection) was virtually unchanged between the CYBER and CRAY calculations, some unexpected areas of difference were noted. One of these involved several of the mass flow rates compared and is due to an error in the packed graphics output file produced by the CRAY code version.

Figure 6.4.1 shows the vessel-side break mass flow from the CRAY run. The intermittent flow interruptions are obviously unphysical, and are not seen in the CYBER results given in Figure 3.2.2a. Such flow interruptions were also seen in other mass flow plots from the CRAY run (e.g., for the pressurizer outflow). Besides being obviously unphysical, they can be seen to be only an artifact of the graphics in Figure 6.4.2, which shows the (same) mass flow rates at the common junction between the two components upstream of the vessel-side break from this CRAY run. Depending on which component the mass flow rate plot request is referenced to, the mass flow is either smooth as expected, or intermittent.

This problem also affects the liquid and vapor velocities plotted at this common junction in the CRAY run, while the densities in the adjacent cells are well-behaved. The same intermittent flow behavior has been seen in CRAY calculations at LANL [15], where it has since been confirmed to be only a graphics problem and has been corrected. Subroutine PACKIT was sometimes packing negative numbers onto the graphics output file incorrectly.

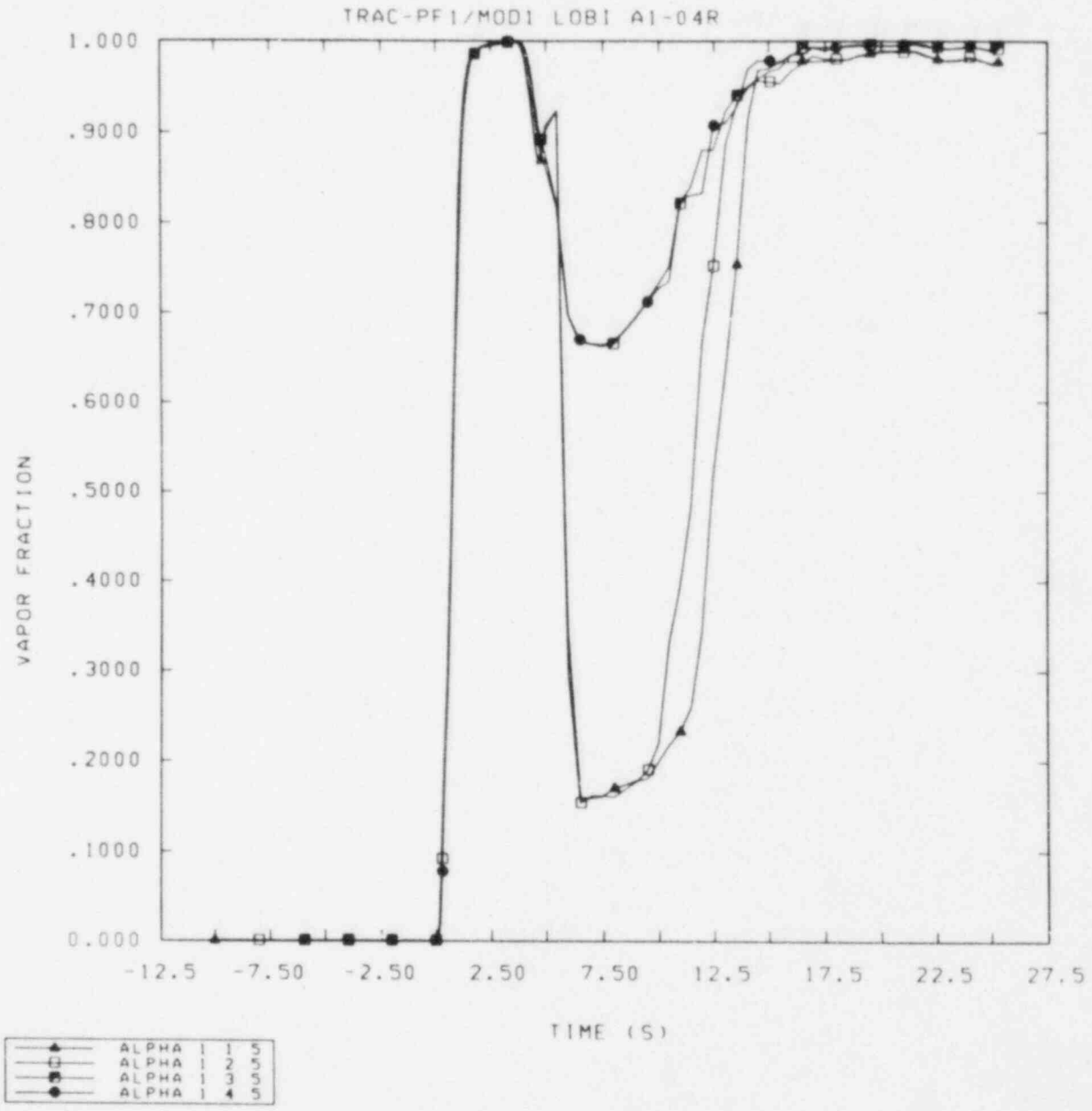

Figure 6.2.1 Void Fractions in Core Cells in Vessel Level 5

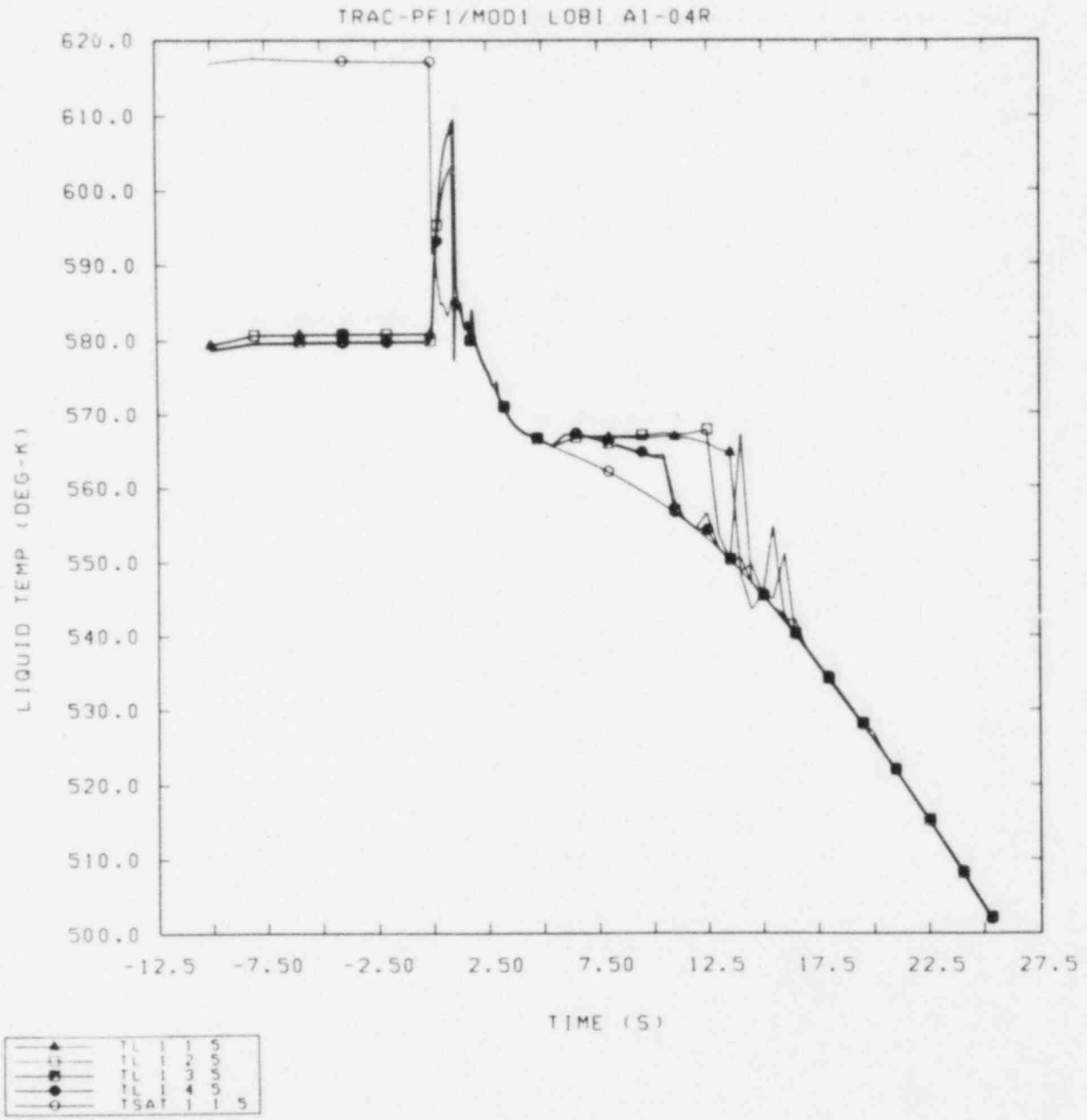

Figure 6.2.2 Liquid and Saturation Temperatures in Core Cells in Vessel Level 5

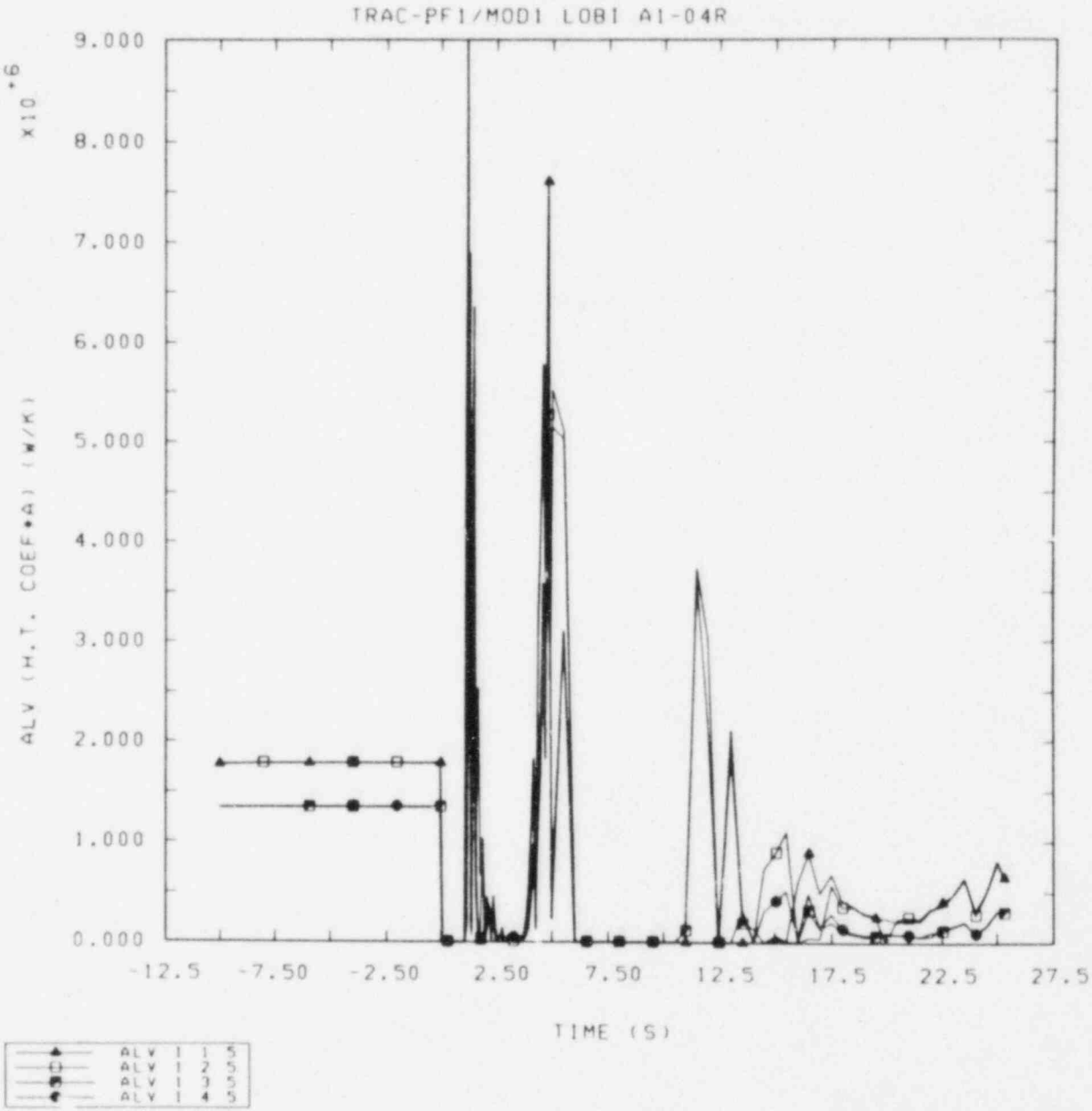

Figure 6.2.3 Liquid Interfacial Heat Transfer (ALV) in Core Cells in Vessel Level 5

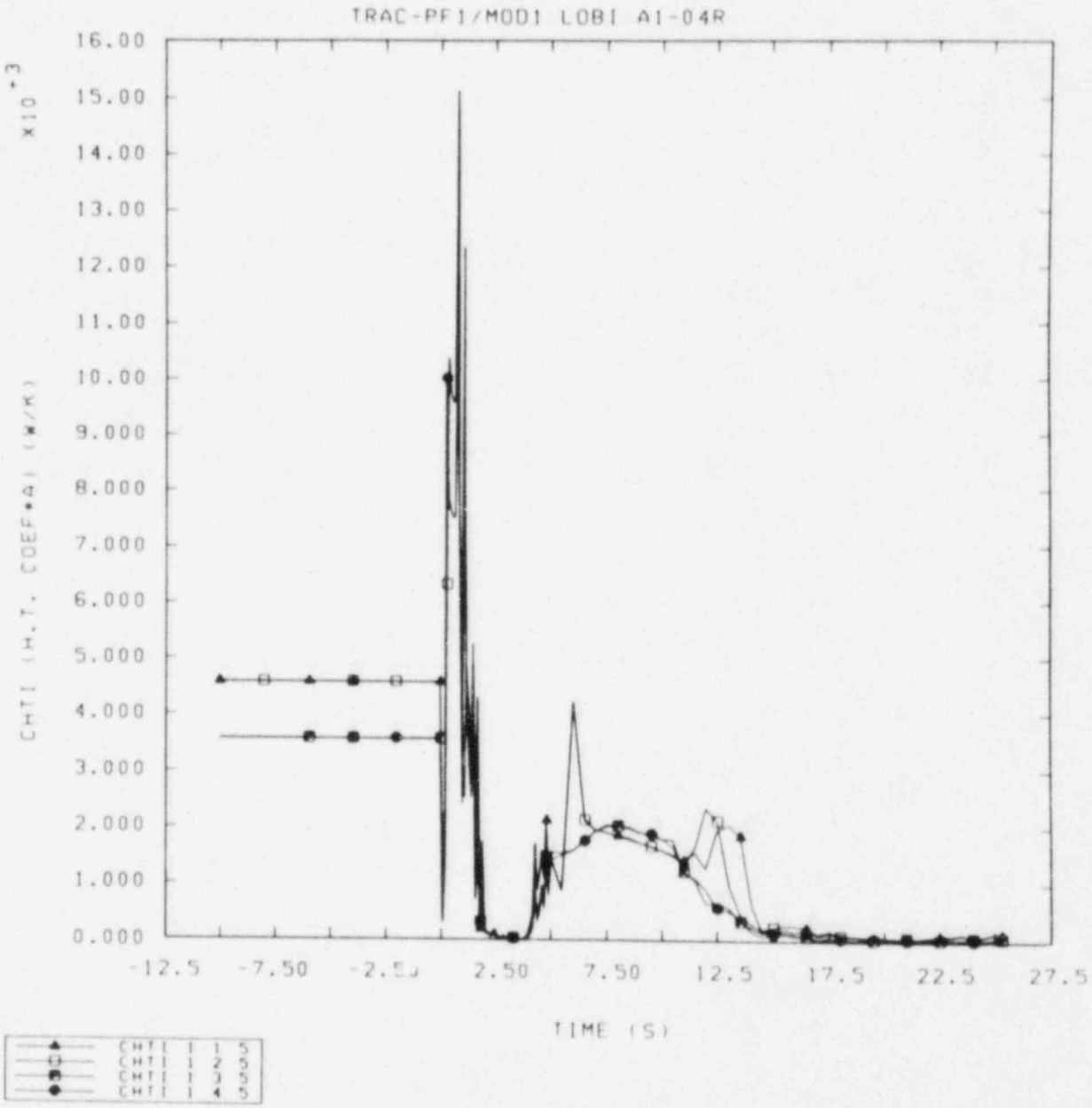

Figure 6.2.4 Vapor Interfacial Heat Transfer (CHTI) in Core Cells in Vessel Level 5

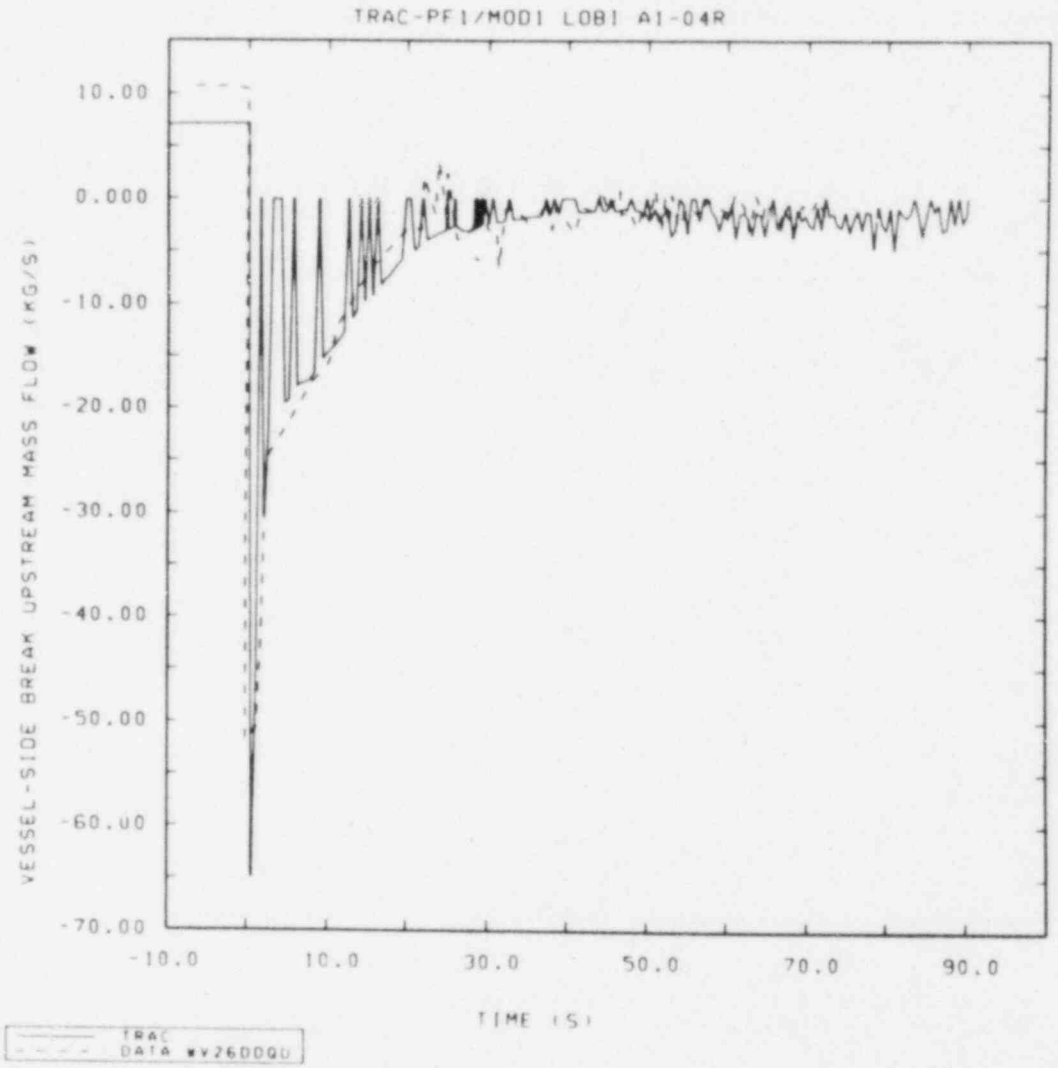

Figure 6.4.1 Vessel-Side Break Mass Flow Rate from CRAY-1S Run

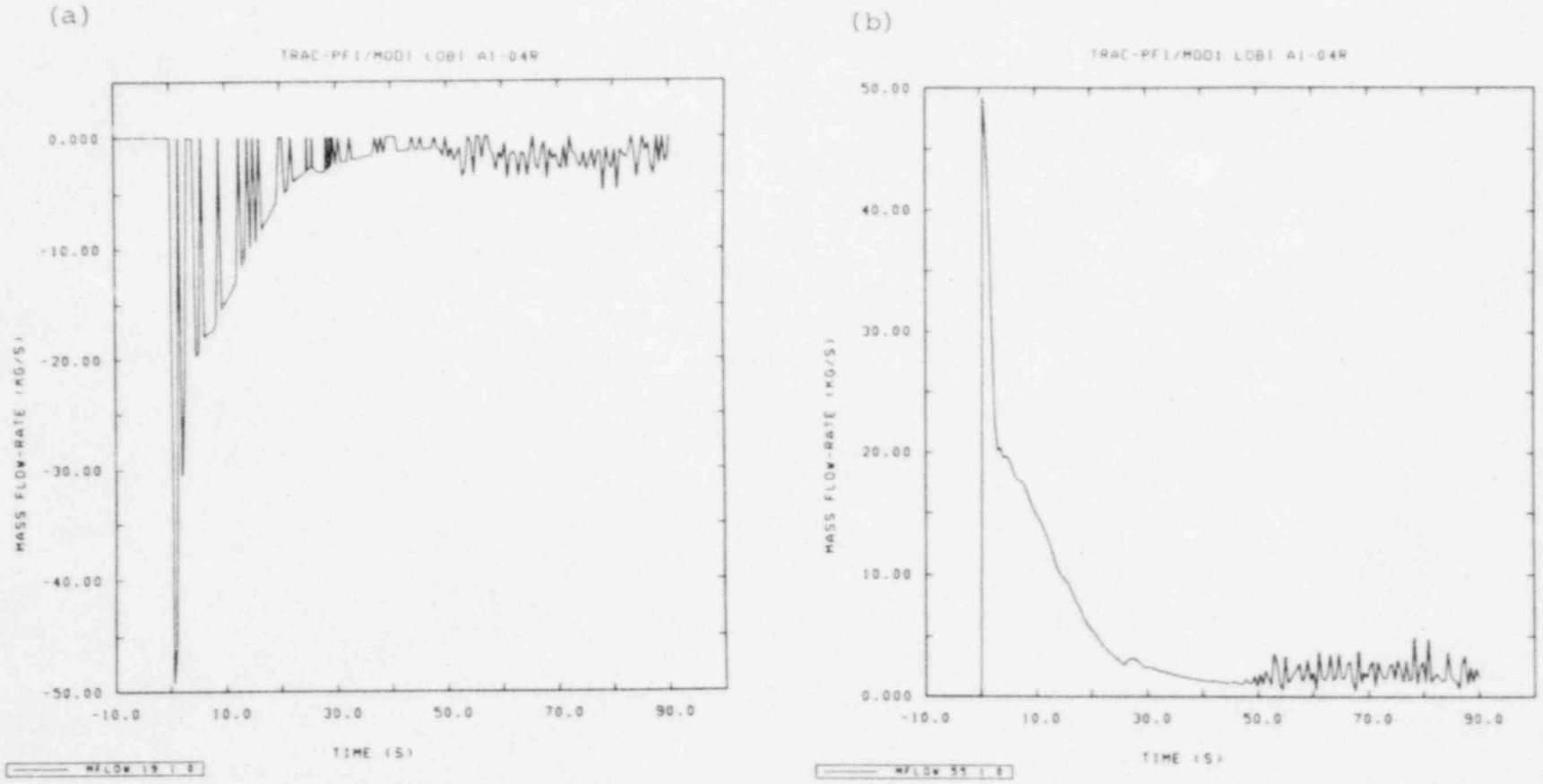

Figure 6.4.2 Mass Flow Rate at Common Junction in (a) TEE and (b) VALVE Upstream of Vessel-Side Break from CRAY-1S Run

7.0 SUMMARY AND CONCLUSIONS

The LOBI A1-04R results presented in this report show that TRAC-PF1/MOD1 correctly predicts the major phenomena occurring during a large break accident. Subcooled and saturated discharge coefficients both equal to 1.0 give good agreement with data for break flows and primary system depressurization. Accumulator flow is calculated to begin within 1 s of the observed time; the predicted accumulator injection is generally within ~5% of the measured value, although there are some small qualitative differences in the injection curves. Both the peak clad temperature and the overall heater rod temperatures are in acceptable agreement with data; again, there are some qualitative differences, with the data showing a total core rewet at ~5-15 seconds and the calculation showing a later and only partial rewet.

Most of the key parameters for a large break LOCA were well predicted, as shown in Table 7.1. In these tests, the agreement for the time at which PCT occurs is not very significant, since it occurs when the power is first ramped down from 100%, which is an input number. The calculated PCT of 788 K is in reasonably good agreement with the experimental value of 823 K, representing a 15% lower heatup relative to saturation and a 4% difference in absolute value. This discrepancy in PCT may be due primarily to the approximation of the actual staggered hollow-rod geometry required in the TRAC input. To ensure the correct initial stored energy in each power region in our model, we matched the power input to each section and the total mass in each section, using the rod average thickness and adjusting the heights of the various core levels. However, the actual hollow rod thickness in the high-powered middle section of the core heated length where PCT occurs is smaller than the average thickness in that region, used in the input, which would increase the characteristic conduction time in the calculation and thus slow the rod heatup. (There is no way to match all the staggered hollow-rod geometry within the current TRAC input limitations.)

When the A1-04R basecase transient was run on both the CYBER-76 and CRAY-1S computers at Sandia (to compare transient results and run times on the two machines for identical calculations), some discrepancies were seen in the core heater rod temperatures, most readily visible in the middle region of the core. The variations in rod temperatures between the CYBER and CRAY calculations are qualitatively and quantitatively similar to the variations seen between the CYBER basecase run and preceding CYBER runs. Neither of the calculations gives results which are obviously unphysical, or obviously more correct. However, the differences are worrisome because they suggest that the rod temperatures (particularly, the rod rewet and quench response at the core hot spot) are very sensitive to small

differences in the vessel flow distribution, which may be affected by small differences in the time step history. This in turn implies that the rod temperature response may prove equally or more sensitive to the radial and azimuthal flow area fractions used, which are generally only "guessed-at" values.

These TRAC-PF1/MOD1 results are generally comparable to our previous RELAP5/MOD1 results for this same LOBI test. The key parameters from that RELAP5 analysis are given in Table 7.1 for comparison. Very similar break flow and primary pressure behavior were calculated, but for a saturated discharge coefficient in RELAP5 of 0.85 rather than 1.0 as in TRAC. The PCT predicted by RELAP5/MOD1 (820 K) is in much better agreement with data than the current TRAC result, and lies within the experimental uncertainty of $\pm$3 K, probably because the staggered hollow-rod geometry could be modelled explicitly in the RELAP5 input. RELAP5 predicted a larger core rewet at 5-15 s than that measured while TRAC gave a smaller partial core rewet in the same time period. The rod temperatures predicted subsequently by TRAC are in better agreement with data than those from RELAP5/MOD1 (which does not have a moving-fine-mesh reflood model); RELAP5 generally predicted more uniform cooldown throughout the entire core rather than a quench front progressing up the core as actually observed. The two codes calculated similar accumulator injection, but very different user-input surge line loss coefficients were required (with the TRAC results considered to be more correct).

Sensitivity studies were done on a number of input modelling assumptions and values. The cold leg noding detail affected the calculation of a liquid plug after accumulator injection begins, with a finer nodalization being required to calculate the formation of a liquid plug in the cold leg downstream of the injection point, as observed in the data. Varying the core bypass flow by a few percent changed the magnitude and timing of the reestablished positive core flow occurring at ~10 seconds, affecting the rod temperatures and the early-time core rewet behavior in particular; there are no direct measurements of the magnitude of this bypass flow, only estimates. The overall system depressurization rate, and thus the onset time of accumulator injection, is controlled by the saturated break flow discharge coefficient used; similarly, the rate of accumulator injection is controlled by the accumulator surge line resistance used, as would be expected.

In the course of this analysis, several coding errors were discovered. One resulted in the calculation of substantial liquid superheat (~10 K) for long periods of time (~10 s) in the

core. This error zeroed out the interfacial area for liquid heat transfer under certain flow conditions and did not allow any heat transfer to the vapor-liquid interface, which would normally remove any excess liquid energy. Correcting the error did not, however, significantly change any of the global behavior calculated. Another error was identified in the time-since-trip logic for tabular lookups in a FILL component, which resulted in only partial shutoff of the secondary side feedwater during this transient; the behavior of interest in a large-break LOCA, however, is in the primary system response and is largely independent of any secondary system behavior. An error was found in the CRAY version of the code, which resulted in some odd-looking mass flow rate plots; the error was only in the way the data was written to the graphics file, not in the values actually calculated by TRAC.

We did not identify any obvious model deficiencies which could affect reactor plant analyses. The necessity of approximating the LOBI staggered hollow-rod geometry and its possible impact on PCT are not expected to occur elsewhere. The extreme sensitivity of individual rod temperatures (in particular, the rewet and quench behavior around the hot spot) to minor differences in the overall calculation suggest that small differences in the calculated flow pattern could have a large effect on rod temperatures. This in turn indicates that the local rod temperatures might also be very sensitive to the radial and azimuthal flow areas assumed. These values are not usually known and both user guidelines from the developers and sensitivity studies on these parameters would help in future analyses.

Table 7.1 Key Parameters

Parameter	Exp.	TRAC	RELAP5
Global (Blowdown) PCT (K)	823	788	820
Time for Global PCT (s)	3	3	3
Time for CHF at Hot Spot (s)	1	1	1
Time for Accumulator Start (s)	24	24	24
Time for Hot Spot Quench (s)	60	60-90*	~80

* Differences between rods at same elevation

8.0 REFERENCES

1. TRAC-PF1/MOD1: An Advanced Best-Estimate Computer Program for Pressurized Water Reactor Thermal/Hydraulic Analysis (DRAFT), Safety Code Development Group, Energy Division, Los Alamos National Laboratory, 1983.

2. W. Riebold et al., Specifications: LOBI Pre-Prediction Exercise, Influence of PWR Primary Loops on Blowdown (LOBI), Technical Note No. I.06.01.79.25, Commission of the European Communities, J.R.C.-Ispra, February, 1979.

3. L. N. Kmetyk, RELAP5 Assessment: LOBI Large Break Transients, NUREG/CR-3075, SAND82-2525, Sandia National Laboratory, March 1983.

4. L. Piplies and J. Bachler, Single-Phase Performance Characteristics of the LOBI Pump, Technical Note No. I.06.01.79.80, Commission of the European Communities, J.R.C.-Ispra, August 1979.

5. L. Piplies and W. Kolar, Preliminary Two-Phase Performance Characteristics of the LOBI Pump (Curves for Fully Degraded Head), Technical Note No. I.06.01.81.13, Commission of the European Communities, J.R.C.-Ispra, February 1981.

6. E. Ohlmer et al., Pressure Drop Behavior of the LOBI Installation, EUR 6971 EN, Commission of the European Communities, J.R.C.-Ispra, September 1980.

7. S. Thompson et al., Thermal/Hydraulic Analysis Research Program Quarterly Report, January-March 1984, NUREG/CR-3820, SAND84-1025/1, Sandia National Laboratory, June 1984.

8. L. D. Buxton and L. N. Kmetyk, TRAC-PF1/MOD1 Independent Assessment: PKL Natural Circulation Tests, NUREG/CR-4423, SAND85-2181, Sandia National Laboratory, to be published.

9. D. Dobranich and L. D. Buxton, TRAC-PF1/MOD1 Independent Assessment: B&W 19-Tube Once-Through Steam Generator Tests, NUREG/CR-3877P, SAND84-1229, Sandia National Laboratory, July 1984.

10. W. Riebold and H. Stadtke, LOBI - Influence of PWR Primary Loops on Blowdown First Results, paper presented at 9th Water Reactor Safety Research Information Meeting, Gaithersburg, MD, October 26-30, 1981.

11. L. Piplies and W. Kolar, Quick Look Report on LOBI Test A1-04R, Communication LQC 80-03, Commission of the European Communities, J.R.C.-Ispra, December 1980.

12. E. Ohlmer et al., Experimental Data Report on LOBI Test A1-04R, Communication LEC 80-03, Commission of the European Communities, J.R.C.-Ispra, December 1980.

13. Code Assessment Review Meeting, Albuquerque NM, December 12-13, 1984.

14. V. H. Ransom et al., RELAP5/MOD1 Code Manual Volume 1: System Model and Numerical Methods; Volume 2: Users Guide and Input Requirements, NUREG/CR-1826, EGG-2070, Idaho National Engineering Laboratory, March 1982.

15. Private communication, L. D. Buxton (Sandia) with C. Booker (LANL), January 1985.

APPENDIX I

LOBI FACILITY

The Loop Blowdown Investigations (LOBI) test facility (shown in Figure AI.1) is located at Ispra, Italy, and supported by the EURATOM Joint Research Centre [3]. The facility was designed to supply experimental data on simulated light water reactor primary coolant system response during the initial high pressure blowdown portion of a LOCA. It is an approximately 1:700 scale model of a four-loop 1300 MWe pressurized water reactor (PWR), consisting of two primary coolant loops connected to the reactor pressure vessel model. While both experimental loops are active loops containing a circulation pump and a steam generator, one (the intact loop) has three times the water volume and mass flow of the other (the single or broken loop). The test facility is designed for 16 MPa and 600 K operation pressure and temperature, respectively. Tube ruptures of various sizes, ranging from double-ended large breaks to single-ended small leaks, may be simulated at three different positions in the single or broken loop (hot leg, cold leg or pump suction leg). Other possible break locations are in the vessel lower plenum and in the steam generator U-tubes. Heat is removed through the steam generators from the primary loops by an active secondary cooling circuit, shown in Figure AI.2, containing two condensers and a cooler (simulating the heat sink represented by the turbines and condensers in the real plant) and a feedwater circulation pump. The nominal operating conditions of the secondary side are 5.5 MPa and 543 K pressure and temperature, respectively, but may be extended to about 8.0 MPa and the corresponding saturation temperature.

For the layout of the LOBI test facility, a scaling factor of 712 has been applied to the thermal power, coolant mass flow and coolant volume of the primary cooling system of the reference plant. This results in 5.3 MWe heating power supplied to a 64 (8x8) heater rod bundle of 1:1 PWR design, 21 kg/s and 7 kg/s coolant mass flow for the intact and broken loops, respectively (resulting in 28 kg/s core mass flow), and 0.82 m^3 coolant volume within the primary loop system (the pressurizer included); this last value holds for a not-scaled 50 mm downcomer gap width. The design of the experimental primary loops and the individual components was chosen to maintain the power-to-volume ratio, the volume ratios of the various components and piping sections to each other, the break size-to-primary coolant system volume ratio, and the single-phase steady state pressure drops and temperature distributions as close as possible to the values in the reference plant. (With respect to the piping in each loop, these criteria led to a reduced length and a relatively too large diameter. Thus the steady state single phase

coolant velocity and mass flux are reduced by about a factor of 2 when compared to the reference plant, since the mass flows are scaled but the flow areas are not.) The heights and elevations of components are scaled 1:1, preserving gravitational heads; the heat transfer surfaces in the core rod bundle and steam generators are full length.

The reactor model (shown in Figure AI.3) consists of the pressure vessel, the core barrel tube and the 64 heater rod bundle, simulating the internal annular downcomer, the core, and the lower and upper plena. With the present core barrel tube of 7 mm wall thickness, the downcomer gap width is 50 mm and is out-of-scale with respect to both the volume and the pressure drop of the downcomer. The average channel fuel rods with average linear power of 20.6 kW/m are simulated full-scale with respect to outer diameter (10.75 mm) and heated length (3.9 m) by electrically heated hollow tubes. As indicated in Figure AI.4, a stepwise varying wall thickness yields a chopped cosine axial power distribution. Each heater rod tube is supplied with three sheathed thermocouples, embedded in the outer surface at different locations, leading to a total of 188 surface temperature measurements at 12 different elevations within the heated length, as shown in Figure AI.5. As in the reactor vessel of the reference plant, grid spacers are equidistantly placed over the heated length; five additional spacers are arranged in the upper unheated part of the rod bundle.

The two U-tube generators, shown in Figures AI.6 and AI.7, are different in volume (3:1) and number of U-tubes (18 and 6) for the intact and broken loops, but equal in height. Their design is geometrically similar to that of the reference plant steam generator, with an annular downcomer for the secondary water. The primary and secondary water volumes are only globally scaled (the total ratio is maintained).

The main coolant pumps for the two loops are equal in size and type. They are operated at different speeds in order to obtain the two different steady-state mass flows of 21 kg/s and 7 kg/s for the intact and broken loops, respectively, at similar pressure heads. The geometrical configuration of the main coolant piping (shown in Figures AI.8 and AI.9) is similar to that in the reference plant; the pipe inner diameters are 73.7 and 46.1 mm for the intact and broken loops, respectively. The pressurizer (Figure AI.10) is scaled down in both the steam and the water volumes, while the height and elevation are full-scale. A 20 kW heat source is installed to generate the system pressure; five cooling tubes placed in the vapor region form a heat sink to regulate the system pressure. The surge line can connect the pressurizer to either the intact or the broken loop hot leg.

Special rupture devices for simulating single- and double-ended pipe breaks are installed in the broken loop, as shown in Figure AI.9 for a cold leg break. Breaks are simulated by quick-opening (~20 ms) flap valves which are mounted at the straight pipe outlets of the rupture devices. These devices are situated within a concrete bunker, which is vented to the atmosphere through two open steel pipes of 400 mm ID. The flap valves are connected to break nozzles, shown in Figure AI.11. When the flap valves are opened, the normal flow path is sealed off by closing a slow-moving (~1 s) ARGUS valve, also shown in Figure AI.9.

Two accumulators, one for each loop, are installed for ECC water injection, the accumulator for the intact loop having three times the volume and capacity of that for the broken loop. While their total volume is scaled down from that of the reference plant accumulators, their height and elevation are full-scale. ECC injection is started automatically by differential pressure controlled quick-opening ball valves as soon as the system pressure has dropped below the accumulator driving gas pressure. Injection lines connect each accumulator to both hot and cold leg piping of its loop, allowing hot leg, cold leg or combined hot and cold leg injection as desired for a particular test. The accumulator surge line geometry for the test we analyzed is shown in Figure AI.12.

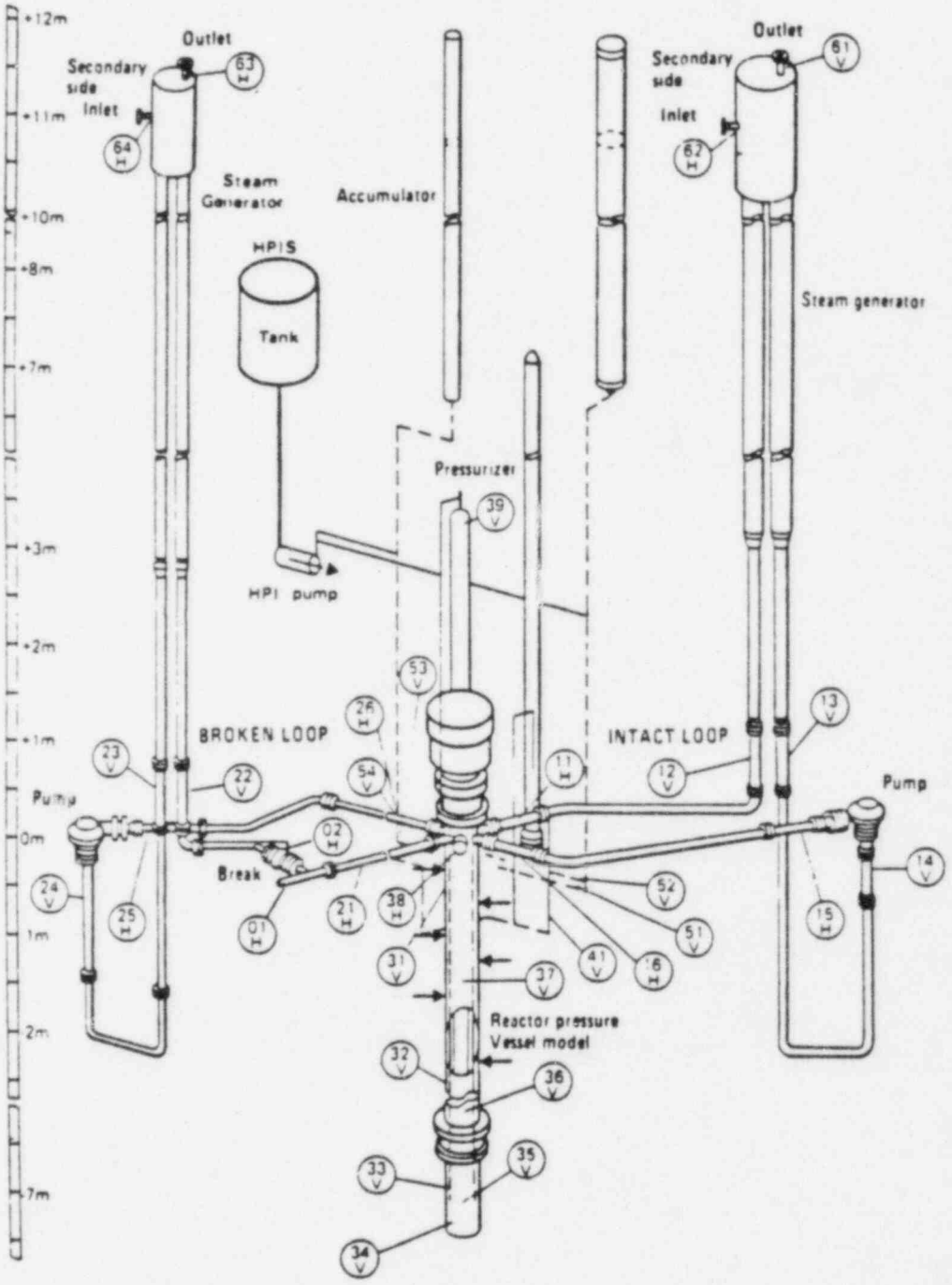

Figure AI.1 LOBI Test Facility

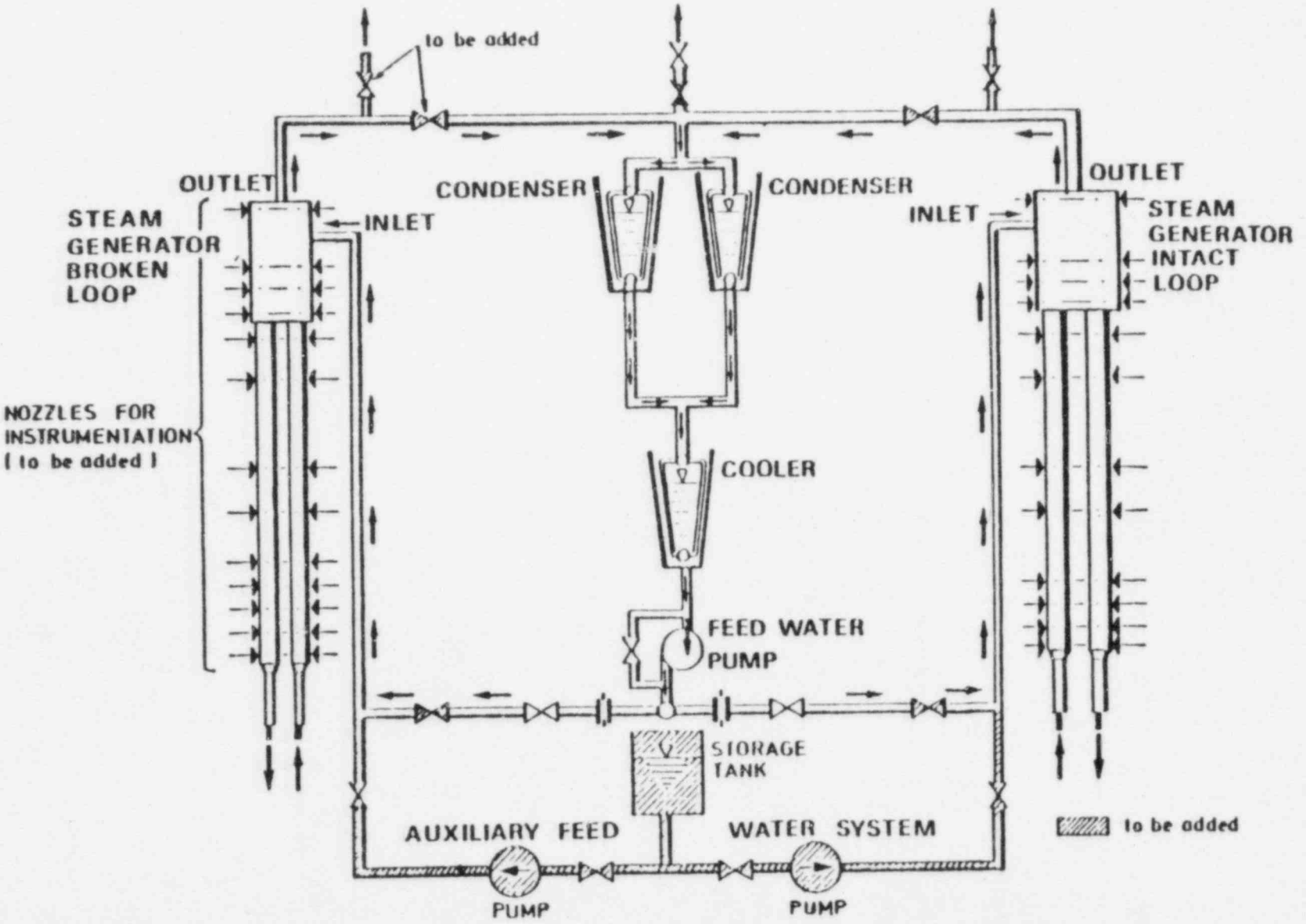

Figure AI.2 Secondary Loop System

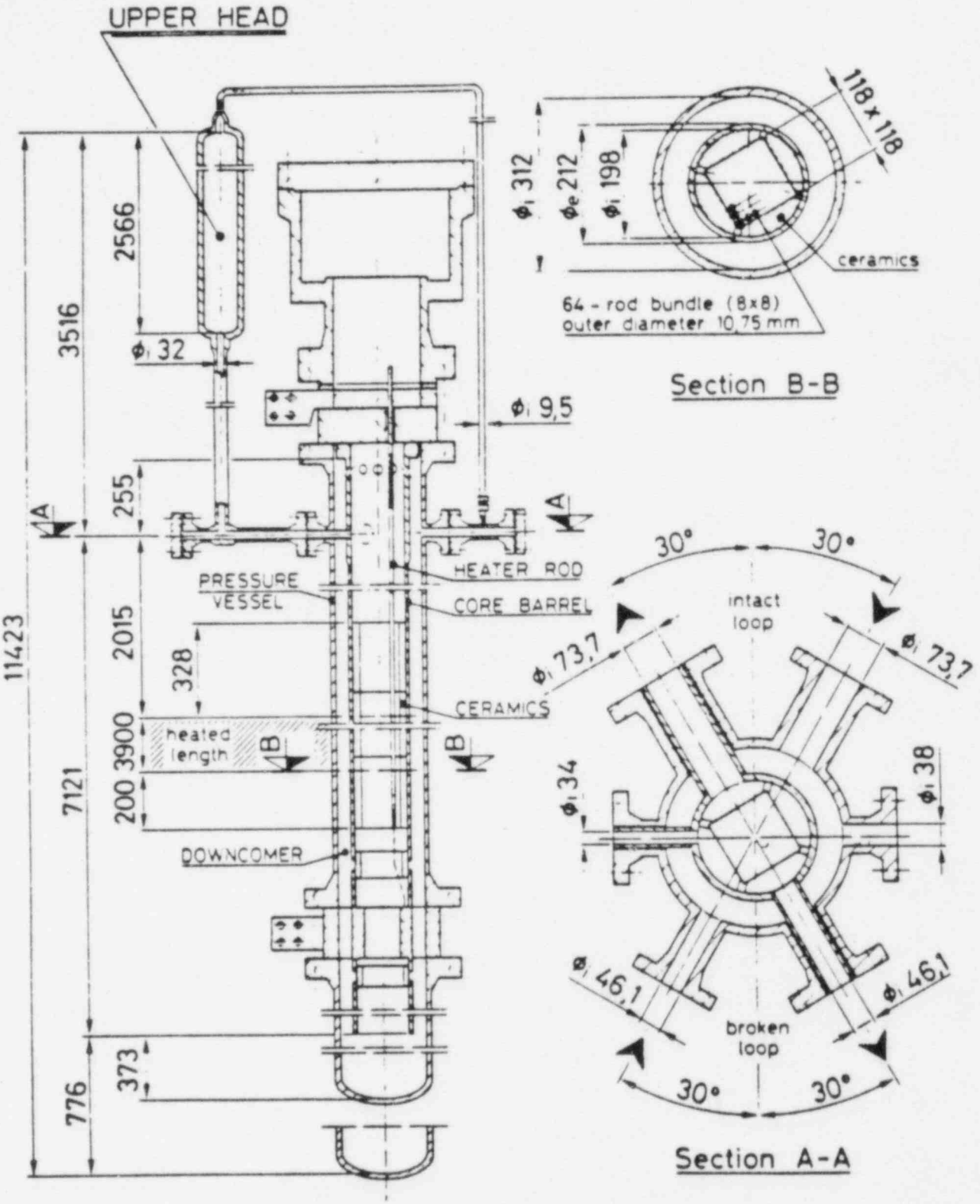

Figure AI.3 Reactor Pressure Vessel

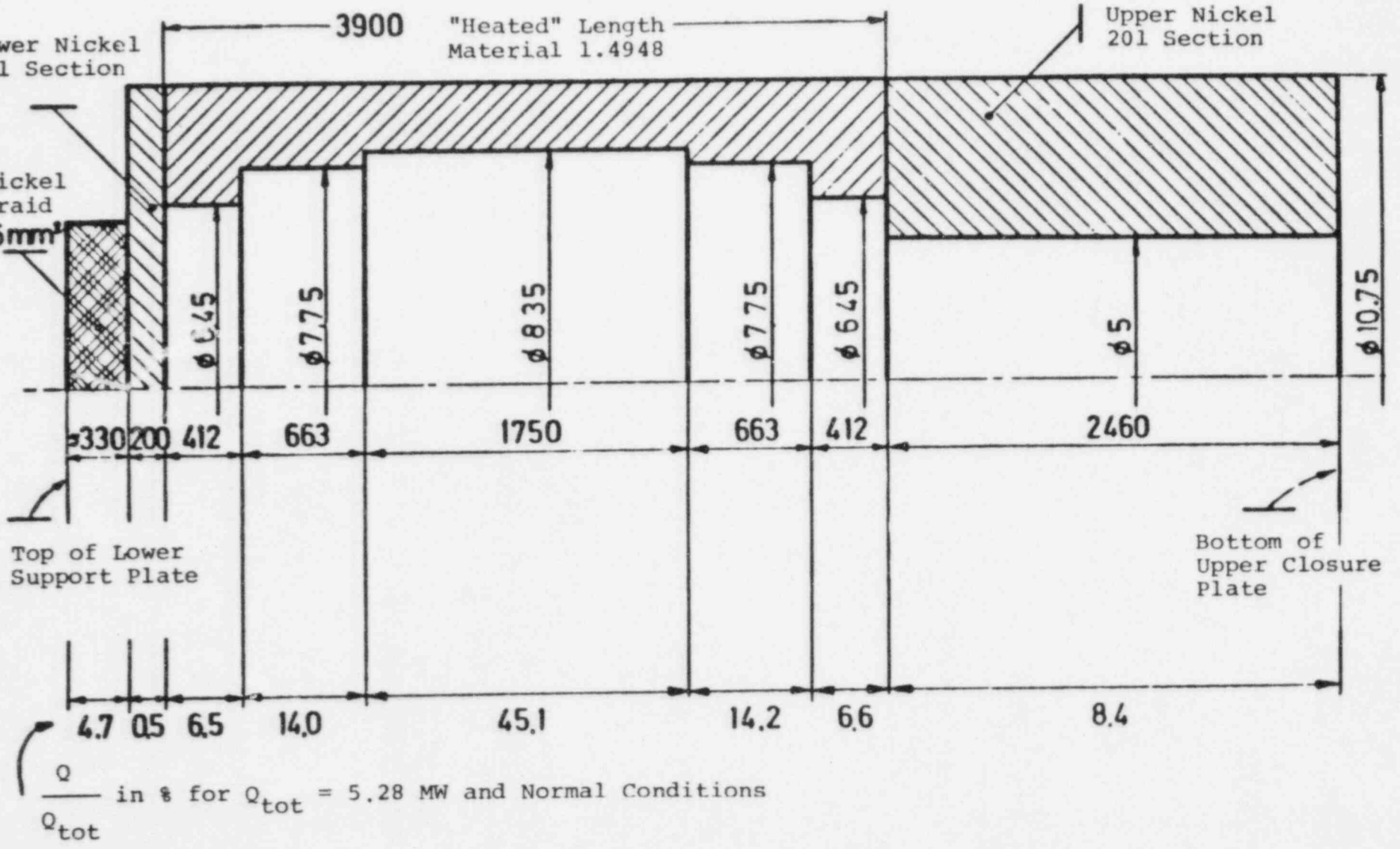

Figure AI.4 Heater Rod (Section and Power Distribution)

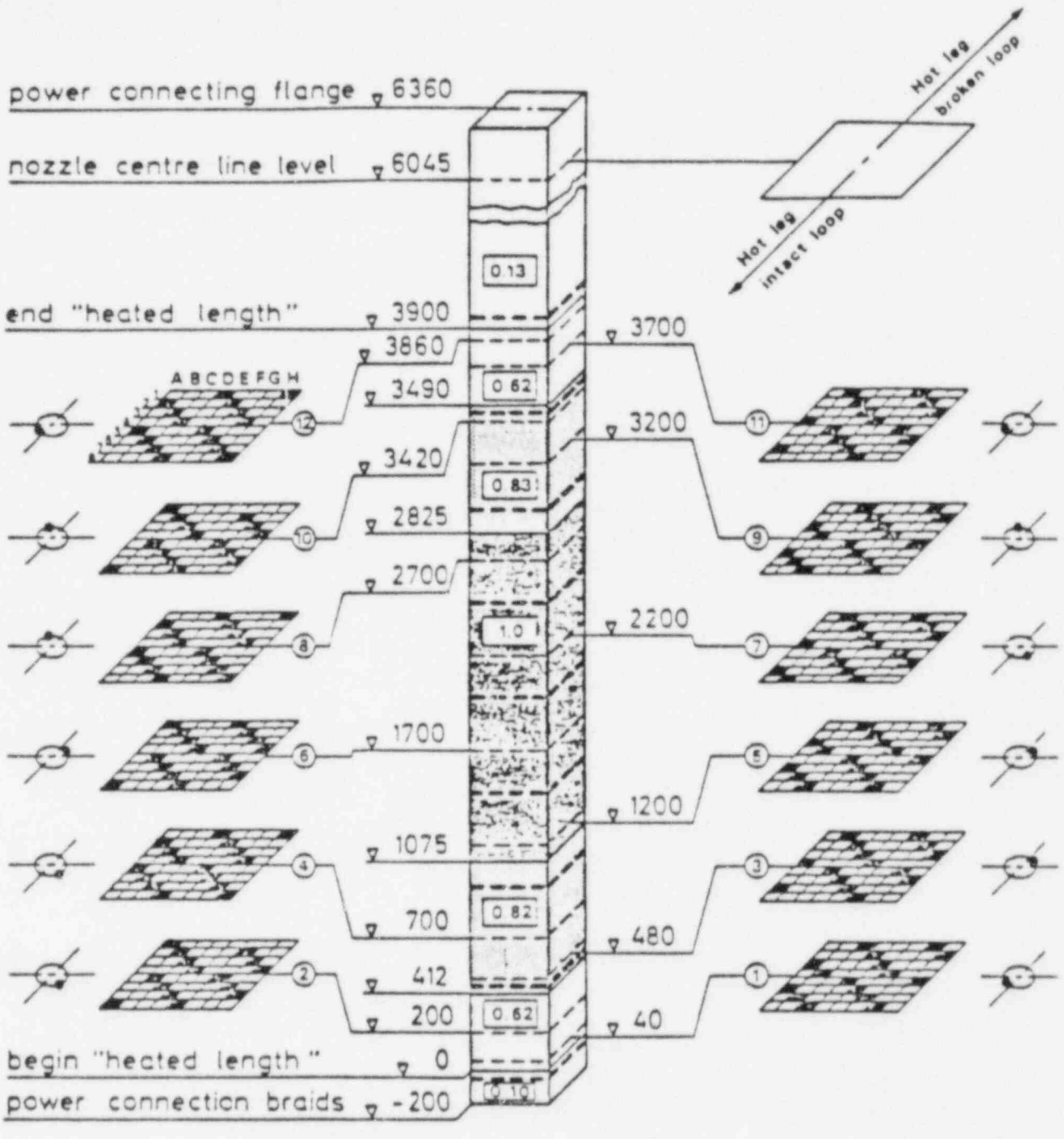

heater rod TC in use

TC - orientation in the rods at each level

① TC - Location level in the bundle (last number in TH-identifier)

0.82 relative heater power $\dot{q}/\dot{q}_{max}$

bundle spacer grids

Figure AI.5 Location of Heater Rod Thermocouples

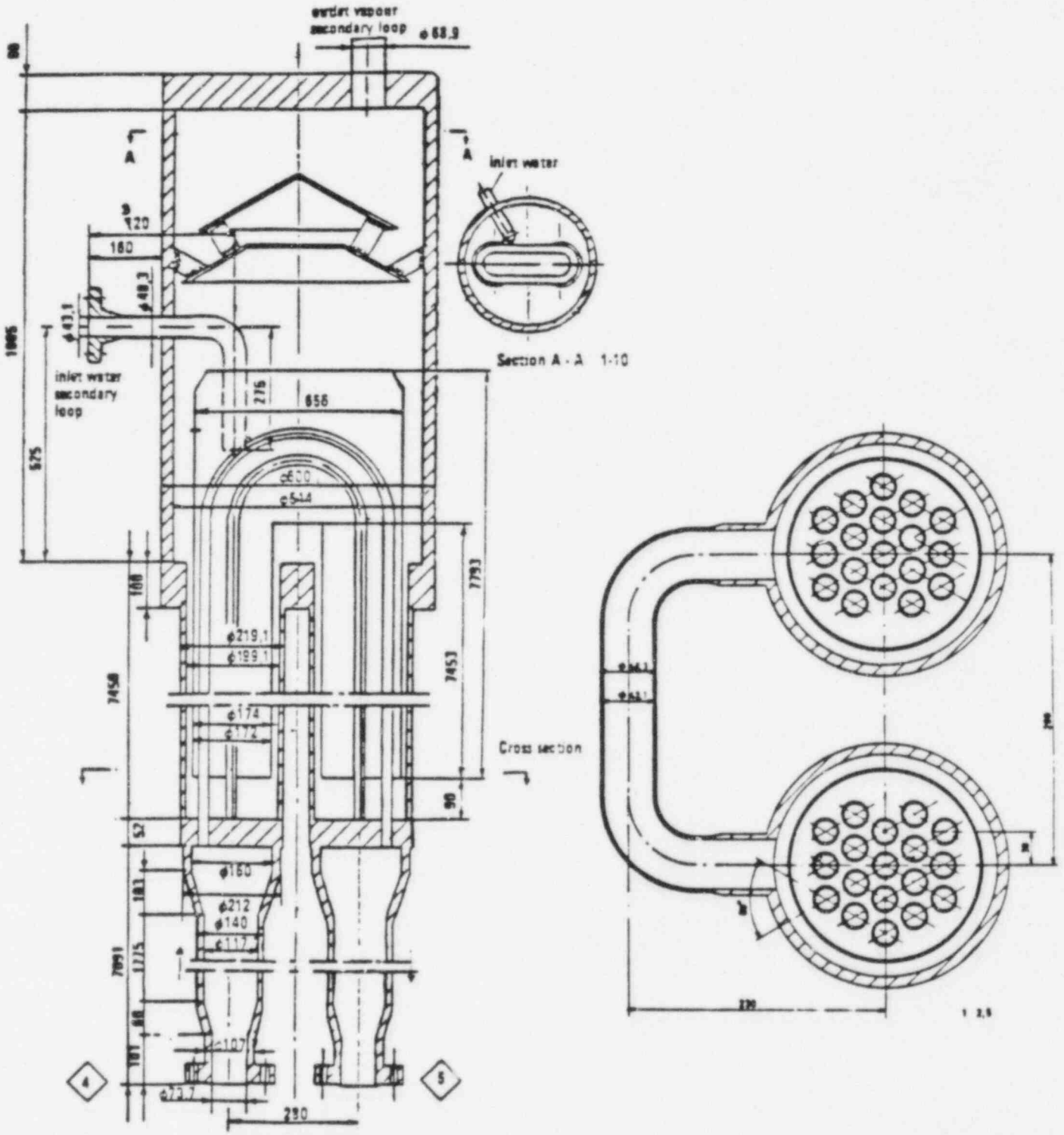

Figure AI.6 Intact Loop Steam Generator

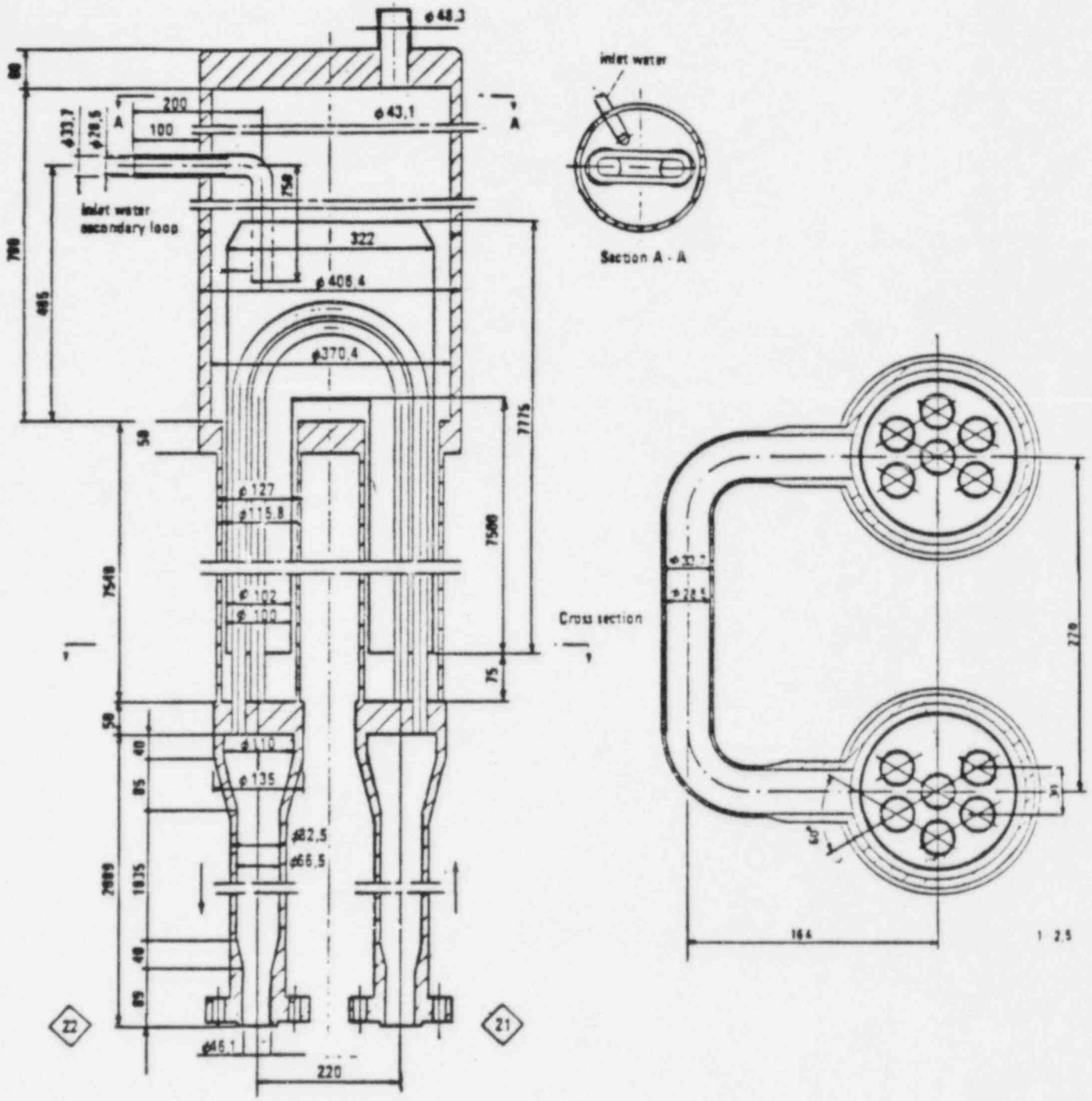

Figure AI.7 Broken Loop Steam Generator

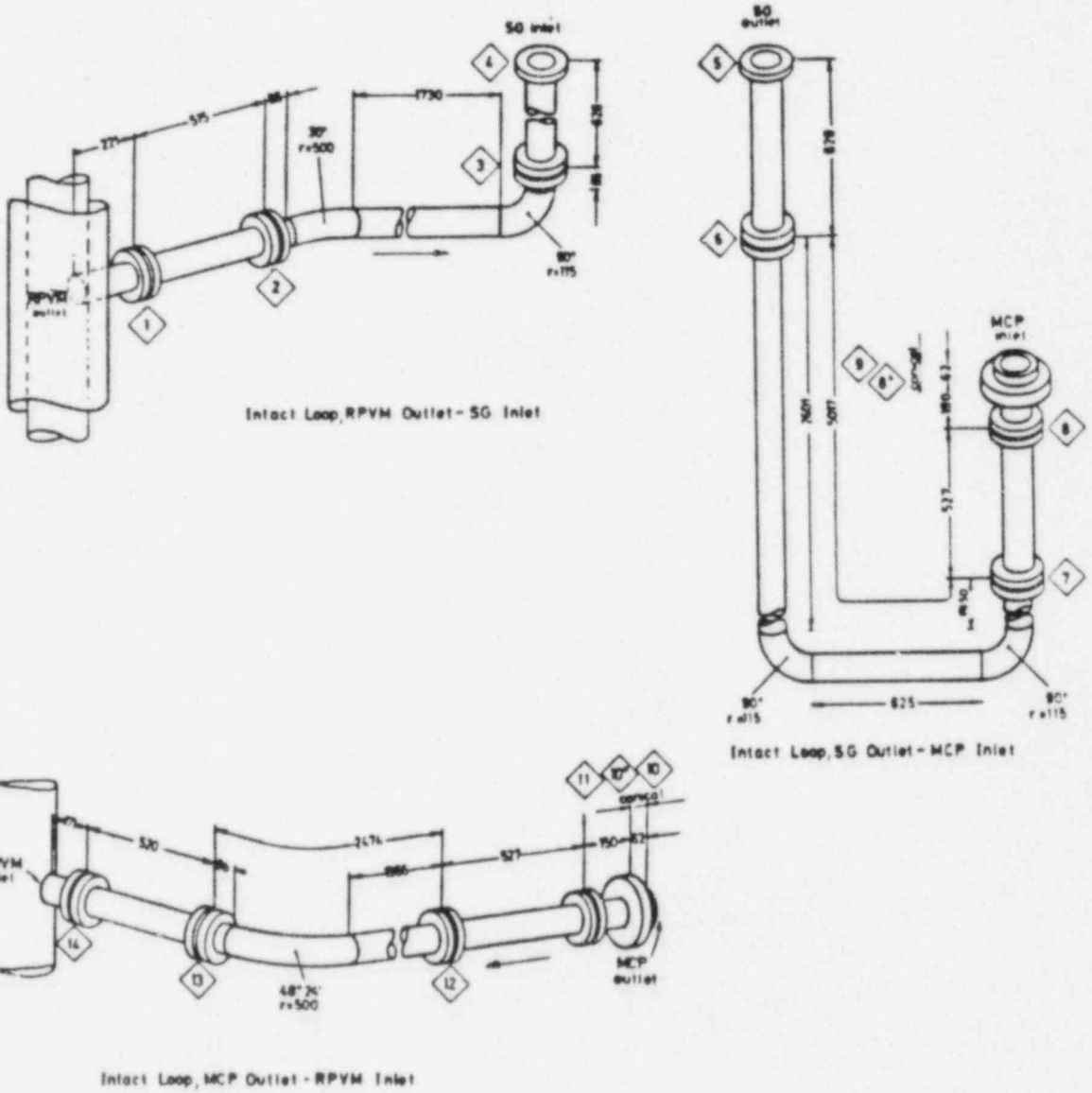

Figure AI.8 Intact Loop Piping -- (a) Hot Leg, (b) Pump Suction Leg, and (c) Cold Leg

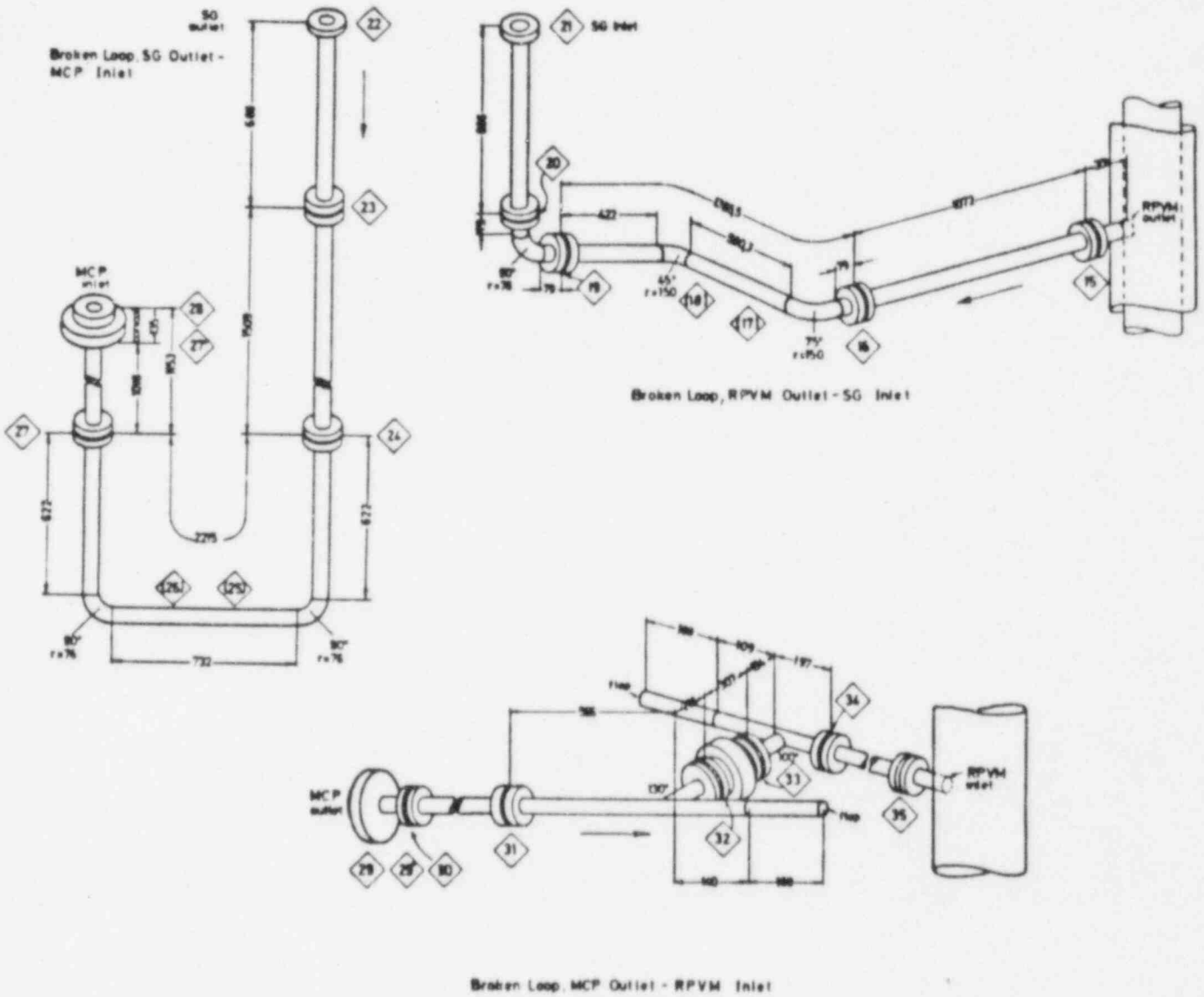

Figure AI.9 Broken Loop Piping -- (a) Hot Leg, (b) Pump Suction Leg, and (c) Cold Leg with Break Assembly (33 is ARGUS Valve)

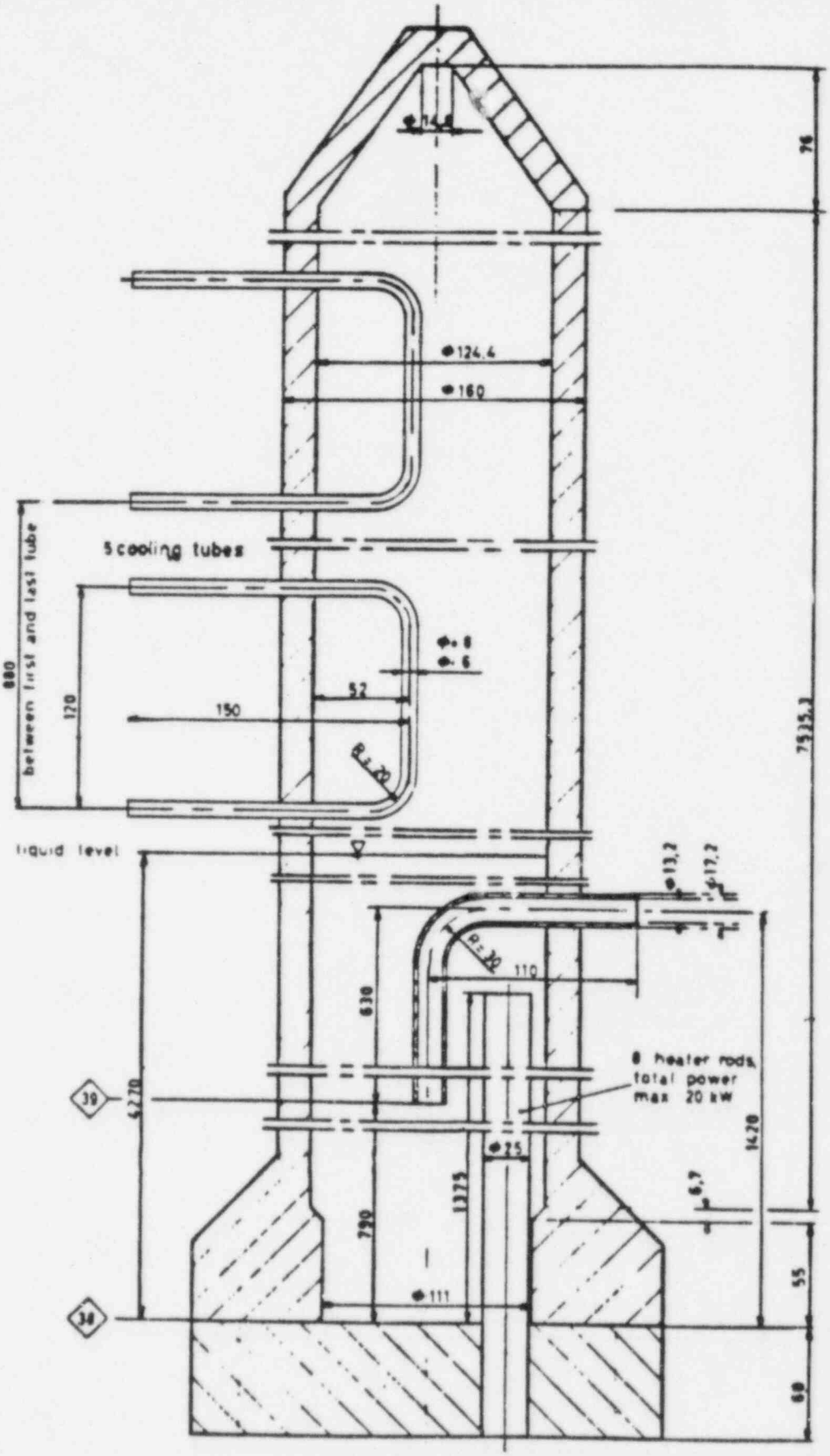

Figure AI.10 Pressurizer

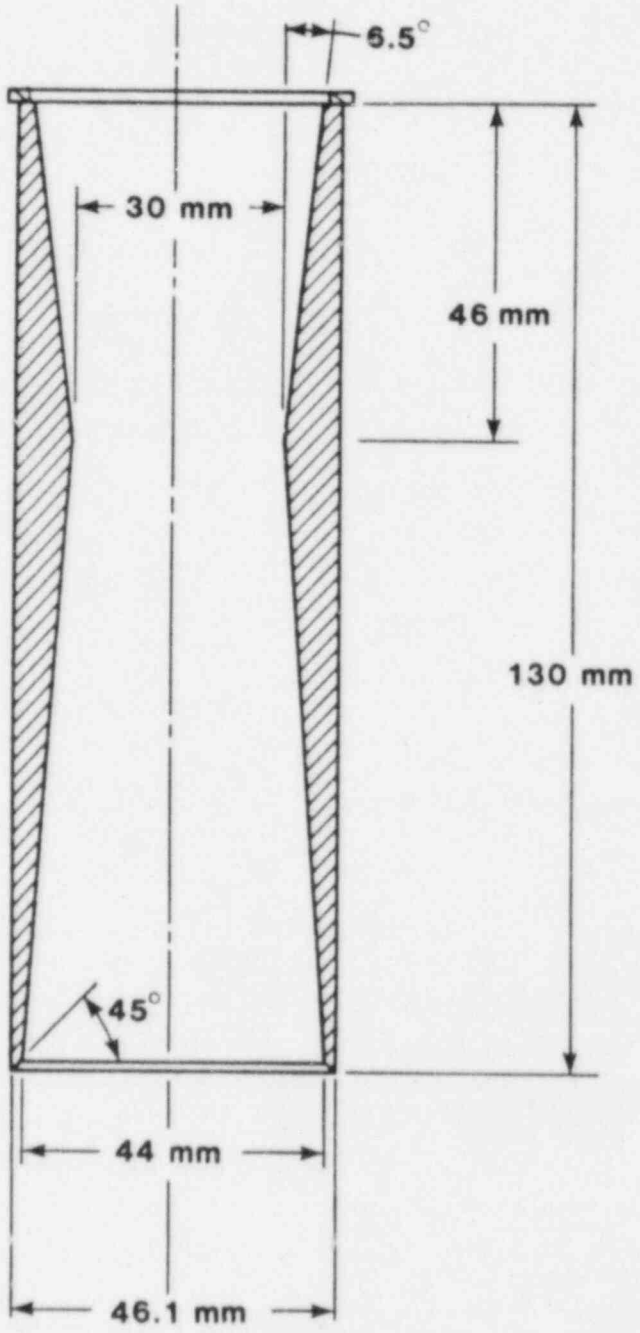

Figure AI.11 Break Nozzle Geometry

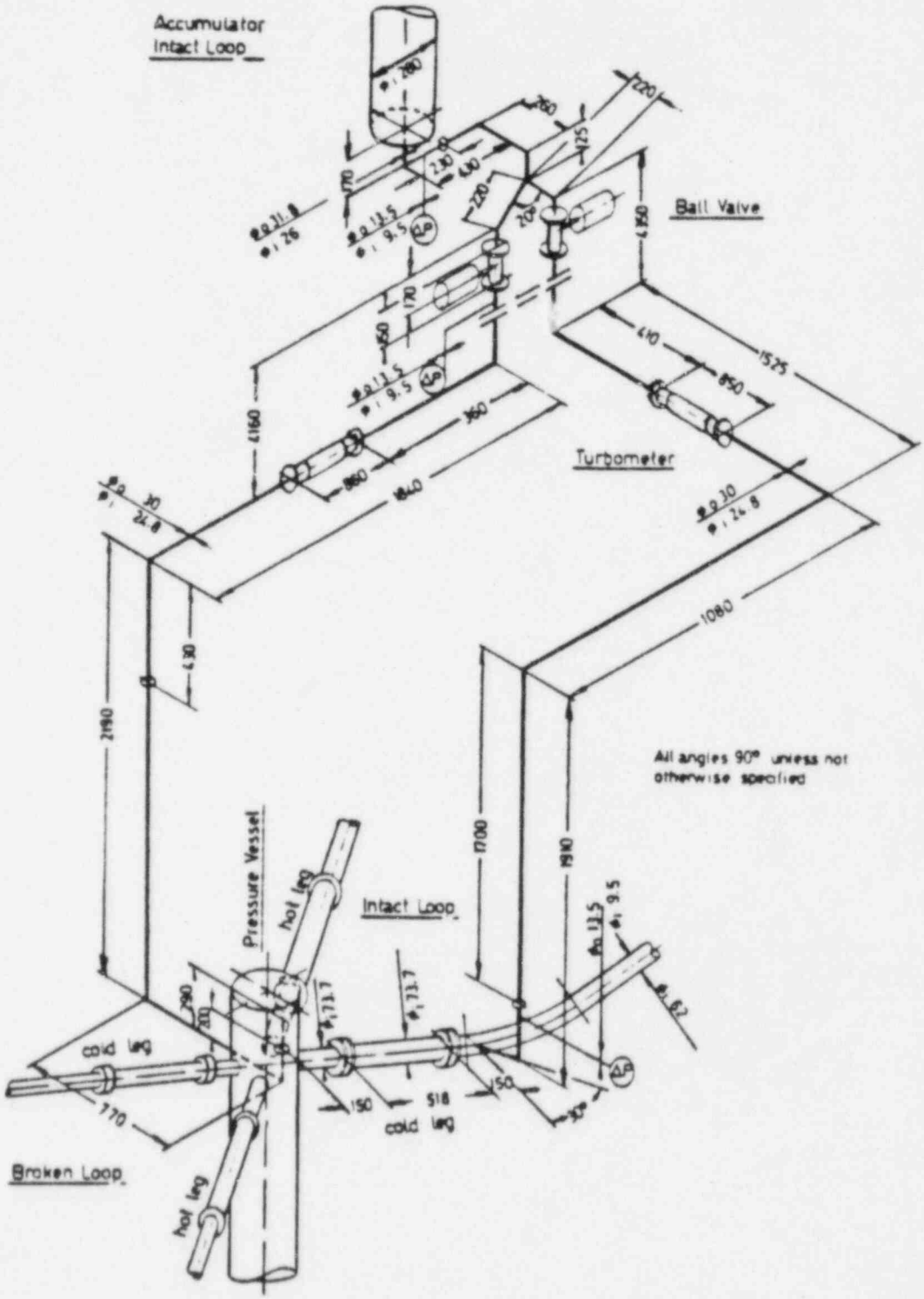

Figure AI.12 Intact Loop Accumulator Surge Line

APPENDIX II

INPUT LISTING

An input listing for the transient is given on attached microfiche.

DISTRIBUTION:

U. S. Government Printing Office
Receiving Branch (Attn: NRC Stock)
8610 Cherry Lane
Laurel, MD 20707
300 copies for R4

U. S. Nuclear Regulatory Commission (5)
Reactor Systems Research Branch
Division of Accident Evaluation
Office of Nuclear Regulatory Research
7915 Eastern Avenue
Silver Spring, MD 20910
Attn: F. Odar
L. M. Shotkin
D. Solberg
H. S. Tovmassian
N. Zuber

EG&G Idaho (5)
Idaho National Engineering Laboratory
P. O. Box 1625
Idaho Falls, ID 83415
Attn: T. R. Charlton
G. W. Johnsen
Edna Johnson
V. H. Ransom
R. J. Wagner

Brent Boyack
T. D. Knight
Rick Jenks
Los Alamos National Laboratory (3)
K553 Q-9
Los Alamos, NM 87545

U. S. Rohatgi, 130
Department of Nuclear Energy
Brookhaven National Laboratory
Associated Universities, Inc.
Upton, New York 11973

N. H. Shah
Babcock & Wilcox Co. (NPGD)
P. O. Box 1260
Lynchburg, VA 24505

Oddbjörn Sandervåg
Studsvik Energiteknik AB
S-611 82 Nyköping
SWEDEN

M. Banaschik (25)
Bundesministerium fuer Forschung
und Technologie
Postfach 200706
5300 Bonn 2
WEST GERMANY

LOBI Project (2)
Heat Transfer Division
EURATOM Joint Research Centre
Ispra Establishment
I-21020 Ispra/Varese
ITALY
Attn: W. L. Riebold
H. Städtke

Jesse Fell (5)
Deputy Director, Water Reactor Programs
Atomic Energy Establishment
Winfrith
Dorchester, Dorset DT28DH
ENGLAND

6400 A. W. Snyder
6410 J. W. Hickman
6417 D. C. Carlson
6420 J. V. Walker
6421 T. R. Schmidt
6422 D. A. Powers
6423 P. S. Pickard
6425 W. J. Camp
6427 M. Berman
6440 D. A. Dahlgren
6442 W. A. von Riesemann
6444 L. D. Buxton (20)
6444 R. K. Byers
6444 R. K. Cole, Jr.
6444 P. N. Demmie
6444 D. Dobranich
6444 M. G. Elrick
6444 L. N. Kmetyk
6444 J. M. McGlaun
6444 J. L. Orman
6444 W. H. Schmidt
6444 R. M. Summers
6444 S. W. Webb
6449 K. D. Bergeron
3141 S. A. Landenberger (5)
3151 W. L. Garner
8024 P. W. Dean

NRC FORM 335 (2.84) NRCM 1102, 3201, 3202

SEE INSTRUCTIONS ON THE REVERSE

U.S. NUCLEAR REGULATORY COMMISSION

BIBLIOGRAPHIC DATA SHEET

1. REPORT NUMBER (Assigned by TIDC and Vol. No., if any)
NUREG/CR-4171
SAND85-0442

2. TITLE AND SUBTITLE
TRAC-PF1/MOD1 Independent Assessment: LOBI Large Break Transient A1-04R

3. LEAVE BLANK

4. DATE REPORT COMPLETED
MONTH: October YEAR: 1985

5. AUTHOR(S)
L. N. Kmetyk

6. DATE REPORT ISSUED
MONTH: December YEAR: 1985

7. PERFORMING ORGANIZATION NAME AND MAILING ADDRESS (Include Zip Code)
Thermal/Hydraulic Analysis Division 6444
Sandia National Laboratories
P. O. Box 5800
Albuquerque, NM 87185

8. PROJECT/TASK/WORK UNIT NUMBER

9. FIN OR GRANT NUMBER
A-1374

10. SPONSORING ORGANIZATION NAME AND MAILING ADDRESS (Include Zip Code)
Reactor Systems Research Branch
Division of Accident Evaluation
Office of Nuclear Regulatory Research
U. S. Nuclear Regulatory Commission
Washington, DC 20555

11a. TYPE OF REPORT
Technical

b. PERIOD COVERED (Inclusive dates)

12. SUPPLEMENTARY NOTES

13. ABSTRACT (200 words or less)

The TRAC-PF1/MOD1 independent assessment project at Sandia National Laboratories is part of an overall effort funded by the NRC to determine the ability of various system codes to predict the detailed thermal/hydraulic response of light water reactors during accident and off-normal conditions. The TRAC code is being assessed at Sandia against test data from various integral and separate effects test facilities. As part of this assessment matrix, a large-break transient performed at the LOBI facility has been analyzed.

Our results show that TRAC-PF1/MOD1 correctly predicts the major phenomena occurring during a large break accident. Subcooled and saturated discharge coefficients both equal to 1.0 give good agreement with data for break flows and primary system depressurization. Accumulator flow is calculated to begin within 1 s of the observed time, and the predicted accumulator injection is generally within 5% of the measured value. Both the peak clad temperature (788 K) and the overall rod temperatures are in acceptable agreement with data (823 K PCT).

Sensitivity studies were done on the cold leg nodalization, the magnitude of the core bypass flow, the saturated break flow discharge coefficient and the accumulator surge line resistance. A coding error was discovered which resulted in the calculation of substantial and prolonged liquid superheat in the core; correcting this error did not, however, significantly change any of the global behavior calculated.

These TRAC-PF1/MOD1 results are generally comparable to our previous RELAP5/MOD1 results for this same LOBI test. Similar break flow and primary pressure behavior were calculated, but for different discharge coefficients; similar accumulator injection was calculated, but for different user-input surge line resistances. The PCT predicted by RELAP5 (820 K) was in much better agreement with data, but the late-time rod temperatures predicted by TRAC are in better agreement with data than those from RELAP5.

14. DOCUMENT ANALYSIS - a. KEYWORDS/DESCRIPTORS

b. IDENTIFIERS/OPEN-ENDED TERMS

15. AVAILABILITY STATEMENT
R4

16. SECURITY CLASSIFICATION
(This page) Uncl
(This report) Uncl

17. NUMBER OF PAGES
126

18. PRICE